Doctoral Dissertation
Doctoral Program in Mechanical Engineering (38.th cycle)

Refined structural modeling for progressive damage and fatigue analysis of composite structures

Elisa Tortorelli
* * * * *

Supervisors
Prof. Erasmo Carrera, Supervisor
Prof. Marco Petrolo, Co-supervisor
Prof. Matteo Filippi, Co-supervisor

Politecnico di Torino
2026

I hereby declare that, the contents and organisation of this dissertation constitute my own original work and does not compromise in any way the rights of third parties, including those relating to the security of personal data.

. . . . . .

Elisa Tortorelli
Turin, 2025

Summary

The increasing use of composite materials in aerospace and mechanical structures has led to a growing demand for reliable numerical tools capable of predicting damage initiation, damage evolution, and fatigue life under realistic service conditions. Unlike metallic materials, composite laminates exhibit complex failure mechanisms governed by material anisotropy, multi-axial stress states, and the interaction of multiple damage modes, such as fiber breakage, matrix cracking, and shear-driven failure. These challenges are further amplified when structures are subjected to variable-amplitude and stochastic loadings, where fatigue damage accumulates over a large number of cycles and is strongly influenced by the spectral content of the excitation.

From a modelling perspective, the accurate prediction of damage and fatigue in composite structures requires the reliable reconstruction of the three-dimensional stress state, including interlaminar and shear components that are often neglected or poorly approximated by classical low-order theories. At the same time, full three-dimensional solid-element models, while accurate, remain computationally prohibitive for large-scale structures and parametric analyses. The trade-off between accuracy and efficiency represents one of the central challenges addressed in the present research activity.

Within this context, the objective of this thesis is to develop and validate a numerical framework capable of accurately predicting progressive damage under quasi-static loading and fatigue response in metallic and composite structures, while maintaining a reduced computational cost. The research is conducted within the framework of the Carrera Unified Formulation (CUF), which provides a systematic and hierarchical approach for the development of refined beam and shell theories. CUF enables the construction of structural theories capable of reproducing three-dimensional stress states by adopting advanced kinematic descriptions.

The research activity is structured into two research lines. First, the focus is placed on the progressive damage analysis of composite laminates under quasi-static loading conditions. A continuum damage mechanics framework is adopted and extended through the implementation of three-dimensional failure criteria. The Hashin 3D formulation is employed to model tensile-dominated damage mechanisms, while a

combined Hashin-Puck criterion is introduced to improve the description of compressive and matrix-dominated failure. The damage models are embedded within CUF-based layer-wise finite element formulations, allowing damage initiation and evolution to be investigated at the ply level. Numerical simulations are performed on a variety of benchmark specimens, including notched and open-hole configurations, demonstrating that the proposed approach is able to accurately reproduce experimental responses and reference numerical solutions while maintaining computational efficiency.

The second line of the thesis addresses fatigue life estimation under stochastic loading using frequency-domain methodologies. The structural response to random excitations is characterized through stress power spectral densities obtained from CUF-based simulations. Fatigue damage is then evaluated without an explicit time-domain integration by adopting spectral fatigue methods, with particular emphasis on the Dirlik formulation for stress-range probability density estimation. For metallic structures, the frequency-domain framework is coupled with linear elastic fracture mechanics, enabling crack-growth prediction through equivalent stress intensity factor ranges derived from spectral stress information. For composite structures, the frequency-domain approach is extended by introducing an equivalent stress definition based on the Tsai-Hill failure criterion, allowing fatigue life estimation while accounting for material anisotropy and multi-axial stress states. The results show that fatigue damage cannot be predicted solely from global quantities such as the stress root mean square. A proper fatigue assessment requires the full stress-range probability density function, which in turn depends on an accurate three-dimensional stress reconstruction.

The proposed framework is validated through numerical applications involving both broadband excitations defined by constant power spectral densities and physically based stochastic loading conditions derived from the von Kármán turbulence model. The results highlight the strong interaction between the load spectral content, structural dynamics, and fatigue damage accumulation, as well as the significant influence of laminate stacking sequence on fatigue performance and sensitivity to stochastic loading parameters.

Overall, this thesis demonstrates that CUF-based higher-order structural models provide a quantitatively improved balance between accuracy and computational efficiency for the analysis of progressive damage and fatigue in metallic and composite structures. In progressive damage analyses, increasing the order of the structural theory leads to a clear improvement in agreement with experimental results. For instance, in the center-notched tensile test, higher-order CUF models predict equivalent stresses at damage initiation within the experimental scatter band, whereas low-order formulations exhibit larger deviations. The results further show that mesh refinement alone is insufficient to ensure accuracy, highlighting the dominant role of the adopted structural theory. At the same time, CUF models are shown to be less sensitive to specimen size in terms of computational cost, as accurate predictions can be obtained using coarser meshes combined with higher-order through-the-thickness

kinematics. For compact tension and compressive tests, CUF formulations coupled with advanced damage models provide force–displacement responses in good agreement with experiments. In particular, Hashin-based CUF models predict damage initiation with errors below 10 % for peak force if compared with experimental results. Discrepancies observed in low-order models are mainly attributed to the absence of delamination modeling, while higher-order CUF approaches are shown to better capture damage localization and initiation trends. In the context of fatigue life estimation under stochastic loading, quantitative comparisons highlight the importance of three-dimensional stress reconstruction. CUF-based two-dimensional models provide an effective framework for fatigue life prediction across different levels of kinematic refinement. Higher-order CUF formulations, while more computationally demanding than low-order models, enable accurate fatigue life predictions and a reliable reproduction of three-dimensional stress fields when compared with full 3D FEM analyses. Low-order CUF models, instead, are primarily employed in this work for extensive parametric analyses, where computational efficiency is essential and the focus is on capturing global trends and sensitivities.

Acknowledgements

First of all, I would like to express my gratitude to my supervisor, Prof. Erasmo Carrera, for his constant guidance and support throughout these years. His scientific vision and enthusiasm for research have been a reference for my professional and personal growth. I am also grateful to Prof. Marco Petrolo and Prof. Matteo Filippi for their support and continuous availability. Their dedication to research and attention to detail have been a constant source of motivation and inspiration. I would also like to thank Prof. Alfonso Pagani and Prof. Enrico Zappino for the valuable exchanges during my time in the research group. I would like to express my sincere gratitude to Dr. Giuseppe Palaia for being a constant point of reference, both professionally and personally, and for the invaluable support provided during this journey. I am also grateful to Dr. Salvatore Saputo for his support and guidance during the first stage of this research. I would also like to thank all the colleagues of the Mul2 research group for the stimulating environment. For the many shared moments and exchanges along the way, I am especially grateful to Shabnam, Daniele, Giulio, Chiara, Andrea, Karim, Myka and Dario. A special mention goes to Marianna, Martina, Francesca, and Piero, who have been there since the beginning, with smiles and constant support that helped carry me through even the most challenging moments.

This research was carried out within the CNMS — Sustainable Mobility National Research Center and received funding from financed by the European Union - NextGenerationEU (National Sustainable Mobility Center CN00000023, Italian Ministry of University and Research Decree n. 1033 - 17/06/2022, Spoke 11 - Innovative Materials & Lightweighting).

Lastly, I am deeply grateful to all my friends. A special thank goes to my Turin group, whose presence made these three years truly meaningful, with a particular mention to Debora and Catiana, who were not only trusted friends but also a true home during this time.

Above all, I would like to thank my family, my parents and my brothers, for their constant care, encouragement, and for always standing by my side, with a special

mention to my little brother Daniele, who holds a truly special place in my life.
Finally, I would like to thank my love and best friend Roberto for his patience, his closeness, and for believing in me even more than I believed in myself, and for his rare ability to bring lightness and warmth into everyday life.

Agli insicuri e agli ultimi.
Spesso, come al cinema, dall'ultima fila si ha una visuale migliore.

Contents

List of Tables

List of Figures

Chapter 1

Introduction

1.1 Context and motivations

The introduction of high-strength and high-stiffness reinforcements, such as carbon fibres, in conjunction with advances in polymer research that have led to the development of high-performance resins as matrix materials,has contributed to improving the efficiency and performance with which the aerospace industry addresses the challenges associated with increasingly complex aircraft designs. The recent utilization of advanced composites, encompassing civil transport aircraft of diverse dimensions, helicopters, satellites, and launch vehicles, serves as a paramount example of the prospective capabilities of these materials; polymers are assuming a central role as structural materials in aerospace vehicles and components [1].
The service life of aerospace structures is influenced by two fundamental aspects. On one hand, the mechanical behaviour of composites is governed by a complex interplay of damage mechanisms, such as fibre breakage, matrix cracking, and interlaminar delamination, that evolve progressively under load [2]. On the other hand, both metallic and composite aerospace structures are exposed to variable and uncertain operational environments, characterised by stochastic loads such as atmospheric turbulence, gusts, random vibrations, and acoustic excitations [3]. In traditional metallic structures, particularly those made of aluminium alloys widely employed in primary aircraft components, such variable loading conditions have long been recognised as a major source of fatigue damage accumulation and crack propagation. As a result, extensive research has been devoted to the development of fatigue life prediction and fracture mechanics-based models for metals, providing a mature and well-established framework for assessing structural integrity under stochastic loading conditions. Together, these aspects make the prediction of structural integrity and residual life of aerospace structures, especially when advanced composite materials are involved, an intricate and unresolved challenge.

When dealing with damage mechanisms, the failure modes in composites are inherently complex, and capturing them within a numerical material model while preserving the underlying physics of damage progression and its effects on structural integrity is far from straightforward. As a result, the numerical modelling of progressive damage in composites has become a highly active field of research, as demonstrated by the extensive body of scientific literature developed over the past decades [4]. Typically, computational models that simulate the progressive damage in fibre-reinforced composites are divided into discrete damage models (DDM) and continuum damage models (CDM). In the framework of CDM, material degradation laws are governed by failure criteria, which are employed to predict damage initiation, progressive failure evolution, and the ultimate strength of composite laminates. Considerable research efforts continue to be devoted to the development of increasingly accurate criteria capable of capturing the onset of failure and the formation of microcracks within the matrix. It is important to note that the underlying damage mechanisms differ significantly under tensile and compressive loading: under tension, failure is typically dominated by fibre breakage and matrix cracking, often leading to crack opening and delamination; whereas under compression, failure is usually associated with fibre microbuckling, kinking, or matrix shear instability [5, 6, 7]. This distinction leads to tailored failure criteria capable of distinguishing between tensile- and compressive-driven damage, thereby ensuring a more reliable prediction of the structural response of composite laminates.

Aerospace structures are routinely subjected to variable and uncertain operational environments, characterised by stochastic loading conditions such as atmospheric turbulence, gusts, random vibrations, and acoustic excitations. These phenomena play a key role in shaping the loading spectra experienced during flight and represent a primary source of fatigue damage accumulation.

In recent years, growing research has highlighted how climate change is further altering the operational environment of aerospace vehicles. In particular, increased atmospheric instability, largely driven by global warming, has led to more frequent and intense turbulence events [8]. These environmental changes exacerbate the variability and severity of in-flight loads, potentially resulting in greater fatigue damage accumulation than previously expected.

Consequently, developing computationally efficient, and physically accurate fatigue assessment tools is essential to support the design, maintenance, and certification of next-generation aerospace structures operating in increasingly uncertain environments. The effect of fatigue damage is primarily determined by two factors: the material's fatigue strength and the applied loading history. Since capturing the complete loading history for a fatigue scenario is often impractical, a finite time interval is usually obtained experimentally and treated as representative. Various methods can then be used to extrapolate and characterize the full loading spectrum from this experimentally measured time history [9]. Both time-domain and frequency-domain approaches

are applicable for fatigue analysis; however, the frequency-domain method is generally preferred because it is less computationally intensive than directly integrating the governing equations in the time domain, as noted by Calvente et al. [10].
This thesis investigates the behavior of composite materials by exploiting refined structural modeling approaches capable of reconstructing three-dimensional stress fields from one- and two-dimensional theories. These stress states are employed for the assessment of progressive damage under quasi-static loading and for fatigue damage prediction under random excitations using frequency-domain analysis, thereby linking the understanding of static failure mechanisms with those induced by variable loading.

1.2 State-of-the-art

1.2.1 Continuum damage mechanics

Computational strategies for simulating progressive damage in fibre-reinforced composites are generally classified into discrete damage models and continuum damage models [11]. DDM approaches provide a physically detailed representation of damage mechanisms and their interactions by explicitly modelling the geometry of cracks within the structure. However, this accuracy comes at the cost of a substantial increase in computational effort. Within DDM, discontinuities across cracks are typically incorporated into the finite element mesh. A widely used technique is the eXtended Finite Element Method (X-FEM) [12, 13], while another common approach relies on cohesive formulations through the Cohesive Zone Method (CZM). In particular, cohesive interface elements have been successfully employed to investigate progressive damage in laminates subjected to tensile loading and to study the interaction between matrix cracking and delamination [14, 15].
An alternative strategy to reduce computational demand is offered by the Continuum Damage Mechanics (CDM). In this framework, cracks within the composite matrix are not modelled explicitly but are assumed to be distributed throughout the finite element volume. Their influence is captured through damage variables that progressively degrade the stiffness of the material point in the structural model [16]. A well-known drawback of CDM is its strong sensitivity to mesh discretization. To overcome this limitation, the crack-band theory is commonly adopted, whereby the fracture energy is rescaled using a characteristic length associated with the dimensions of the finite element [17].
In the case of tensile loading, CDM has been extensively applied to predict damage initiation and growth in composite laminates. Studies have demonstrated its capability to capture matrix cracking, fibre breakage, and delamination phenomena under uniaxial and multiaxial tension. Several authors have proposed enhanced failure criteria as the maximum stress, Hashin, Puck, Hoffman, Yamada-Sun, Tsai-Hill, and Tsai-Wu criteria [18, 19, 20, 21, 22, 23]. Arruda et al. [24] proposed an innovative

two-dimensional orthotropic damage model based on the Tsai–Wu criterion, capable of capturing the main failure mechanisms. In [25], a nonlinear progressive damage model was developed by combining the Hashin and Matzenmiller–Lubliner–Taylor (MLT) failure criteria, specifically applied to 3D woven composites. Other studies have instead employed three-dimensional extensions of the Hashin failure criterion [26, 27]. Furthermore, tensile damage simulations have often served as a benchmark to validate CDM approaches, as the mechanisms are relatively easier to characterize experimentally, and the predicted size effects and notched behaviour in tension have shown good correlation with experimental data [28, 29].

In contrast, compressive damage modeling within the CDM framework has been less extensively investigated, due to the more complex mechanisms involved. Under compressive loading, damage evolution is dominated by fiber kinking, matrix shear failure, and inclined fracture planes, which are more challenging to capture within a continuum formulation. Classical criteria such as Hashin provide a first approximation, but more advanced formulations such as the Puck criterion have been shown to improve predictive capabilities for matrix compression, as they explicitly account for inclined fracture mechanisms in agreement with experimental observations [30, 31, 32].

In summary, while tensile CDM approaches are well established and widely validated, compressive CDM remains a more active research area, where the selection of appropriate failure criteria, particularly for matrix-dominated mechanisms is crucial for accuracy.

More recently, efforts have also focused on integrating CDM with advanced structural modeling frameworks, such as the Carrera Unified Formulation (CUF). In this context, the Composite Damage Model (CODAM) and its second-generation extension, CODAM2, have been widely employed. CODAM is a continuum damage model specifically developed for laminated composite materials, in which damage initiation and evolution are governed by failure criteria and associated degradation laws within a CDM framework. CODAM2 has been successfully used to model nonlinear material behaviour under both tensile [33] and compressive [34] loading conditions. These works demonstrated the potential of CUF in progressive damage modeling by coupling CODAM2 with a two-dimensional Hashin failure criterion. Similarly, Trombini et al. [35] combined a 3D Hashin orthotropic model with refined one-dimensional CUF-based finite elements to capture intralaminar damage mechanisms with high fidelity. Building on this framework, recent studies have further improved the modeling of compressive failure by employing Hashin 3D and Puck criteria for the matrix, the latter being particularly effective in describing inclined fracture mechanisms observed experimentally [36, 37].

1.2.2 Fatigue in metals

Fatigue in metallic materials has been extensively investigated over the past century and represents one of the most mature and well-established areas of structural mechanics. Unlike composite materials, metals generally exhibit a comparatively limited set of damage mechanisms, with fatigue behavior primarily governed by crack initiation and subsequent crack propagation under cyclic loading. This relative simplicity has enabled the development of robust theoretical, experimental, and numerical frameworks for fatigue life prediction, which today form the foundation of most engineering fatigue design standards [38].

Early fatigue studies focused on constant-amplitude cyclic loading, leading to the classical stress-life (S-N) approach introduced by Wöhler. These formulations established empirical relationships between stress amplitude and number of cycles to failure, providing a practical basis for high-cycle fatigue assessment [39]. For low-cycle fatigue, where plastic deformation becomes significant, strain-based approaches were introduced, most notably the Coffin-Manson relationship, which explicitly accounts for cyclic plastic strain contributions [40, 41]. Mean stress effects were later incorporated through correction models such as Goodman, Gerber, and Smith-Watson-Topper formulations [42, 43, 44].

As engineering applications increasingly involved complex loading histories, fatigue assessment methodologies evolved to address variable-amplitude loading. Linear cumulative damage models, most notably Miner's rule, were introduced to estimate fatigue life under spectrum loading by summing damage contributions from individual stress cycles [45]. Despite its simplicity and widespread use, Miner's rule is known to neglect load sequence effects and interaction phenomena, motivating the development of nonlinear cumulative damage models and crack growth-based approaches [46].

A major advancement in metallic fatigue analysis was the adoption of fracture mechanics concepts, which shifted the focus from total life prediction to crack propagation modeling. Paris and Erdogan established a power-law relationship between crack growth rate and stress intensity factor range, enabling fatigue life estimation based on measurable crack evolution [47]. Subsequent extensions incorporated threshold effects, crack closure, and load ratio dependencies, resulting in more accurate predictions across a wide range of loading conditions [48].

In parallel, multiaxial fatigue criteria were developed to address non-proportional and combined loading states. Stress-based and strain-based critical plane approaches gained prominence, allowing fatigue damage to be evaluated on planes experiencing maximum damage parameters [49, 50]. These methods demonstrated improved predictive capability compared to equivalent stress approaches, particularly in the presence of shear-dominated loading and phase differences between stress components.

For applications involving random and vibration-induced loading, fatigue assessment in metals has increasingly relied on frequency-domain techniques. In this framework,

the loading and structural response are characterized statistically through power spectral densities (PSD), enabling fatigue life estimation without reconstructing long time histories. Classical spectral methods, such as those proposed by Miles and Bendat, established the relationship between stress PSD and fatigue damage accumulation [51]. Subsequent developments introduced cycle counting approximations based on spectral moments, culminating in widely used formulations such as the Dirlik method, which provides accurate stress range probability density functions directly from PSD data [52].
Frequency-domain fatigue approaches have been successfully applied to metallic structures in aerospace, automotive, and offshore engineering, where random vibration and broadband excitation are dominant [53, 54]. These methods offer significant computational advantages over time-domain simulations, particularly when coupled with finite element models for structural dynamics analysis. However, their accuracy strongly depends on the quality of the stress response prediction and on the ability of the structural model to capture local stress concentrations.
Overall, fatigue modeling in metals has reached a high level of maturity, with well-established methodologies spanning constant-amplitude, variable-amplitude, multiaxial, and stochastic loading regimes. This solid theoretical and experimental foundation has made metallic fatigue a natural reference benchmark for validating advanced fatigue analysis frameworks and extending frequency-domain methodologies toward more complex material systems, such as composite structures.

1.2.3 Fatigue in composites

One of the key limitations in the adoption of composite materials in aerospace structures lies in their complex and still not fully understood fatigue behavior [55]. Fatigue in composites is fundamentally different from that in metals. Whereas metallic fatigue is often dominated by crack initiation and propagation under cyclic stresses, composites exhibit multiple interacting damage mechanisms, including matrix cracking, fiber breakage, fiber–matrix debonding, delamination, and progressive stiffness degradation. It is evident that such mechanisms are concurrent with a non-linear evolution. When the external loading is stochastic, multi-axial, and variable in amplitude, as in the case of vibration, induced fatigue, the prediction of service life becomes significantly more challenging [56, 57].
Despite the significant investment in research over several decades, existing methodologies have yet to yield universally reliable stress-based prediction models for composite structures in such environments. The primary challenges arise from the necessity to consider the multi-axial nature of stresses, the stochastic distribution of loads, and the progressive degradation of material properties over time [58, 59]. Consequently, the development of robust fatigue life prediction methods remains one of the most active and unresolved areas.

Initial studies on composite fatigue life were primarily based on classical strength theories adapted from metallic materials. Examples of first studies on fatigue behaviour were applied in CFRP jointed specimens [60] and the response under stochastic excitation analysed by Goswami [61]. A number of fatigue models were formulated around static strength criteria, most notably Tsai–Hill and Puck's criterion [62, 63, 64]. These approaches attempted to extend uniaxial fatigue principles to multiaxial domains by introducing equivalent stresses. For example, a fatigue damage parameter derived from the Tsai–Hill criterion incorporated a multiaxial Miner's coefficient, allowing for irregular stress spectra [62]. Recognizing the inadequacy of uniaxial-equivalent stress approaches, other researchers proposed multiaxial models explicitly rooted in Puck's failure theory [63]. Additional studies refined these methods by modifying Tsai–Hill with constant life diagrams, enabling the prediction of S-N curves for unidirectional carbon fiber-reinforced laminates while accounting for fiber orientation and stress ratio [65]. More advanced models acknowledged the role of strength degradation as a function of cycle number. Fiber fatigue models were developed to incorporate the reduction of material strength over time [64], while random vibration fatigue models utilized equivalent stresses based on Tsai–Hill in combination with stress time histories [66]. These contributions represented a first step toward moving beyond purely static-based predictions, but their accuracy remained limited, particularly in complex loading environments.

As applications demanded higher fidelity models, significant research attention shifted to the fatigue behavior of composites under multiaxial loadings. Experimental campaigns highlighted the detrimental effect of shear and transverse normal stresses on fatigue life [58], while theoretical frameworks attempted to formalize prediction methods based on multiaxial fatigue strength criteria [67]. Generalized property degradation models were later introduced to simulate the evolution of material stiffness and strength, using data derived from uniaxial tests but extended to multiaxial conditions [68, 69]. Formulations explicitly considered stress concentrations and load ratios, providing more realistic simulations of structural fatigue behavior. Other investigations explored the effects of biaxiality ratio, off-axis loading angle, phase differences between stress components, and structural discontinuities such as notches [70, 71].

Comparisons between isotropic and anisotropic fatigue behaviors further enriched this field. One significant outcome was the development of a fatigue damage criterion based on stresses acting on the failure plane, which was experimentally validated [72]. Critical-plane approaches soon gained prominence: a unified fatigue damage model applicable to both isotropic and anisotropic materials was proposed, incorporating mean stress effects [73]. Experimental studies confirmed these findings: tests on unidirectional GFRP rods under torsion and combined torsion/bending revealed that combined loading conditions could actually extend endurance limits compared to pure torsion [74]. A separate study proposed a predictive model for identifying the critical plane in laminates, distinguishing between fiber-dominated and matrix-dominated

failures [75].
While early models addressed constant or controlled loading conditions, real-world applications frequently involve variable-amplitude and random vibration loadings. As a result, fatigue life prediction models specifically designed for stochastic environments were developed. One strand of research focused on modal analysis: changes in natural frequencies and damping ratios were employed as indicators of fatigue damage and residual life [76]. In [77], the influence of load ratio was systematically examined for both constant-amplitude and block-loading regimes, resulting in more comprehensive fatigue life models. Random vibration experiments on C/SiC laminates revealed that reductions in natural frequency, driven by fiber fracture, could serve as reliable indicators of specimen failure [78]. Microscopic examinations further identified fiber pull-out and fiber splitting as dominant mechanisms in longitudinal and transverse directions, respectively.
Progressive damage models emerged as a powerful tool to simulate ply-level degradation. By applying stiffness degradation methods combined with Puck's failure criterion, these models accounted for sequence effects in block and spectrum loadings [79]. The sensitivity of composite fatigue life to vibration frequency was demonstrated for ceramic matrix composites, where acoustic loading frequency strongly influenced fatigue performance. Frequency-based modifications of S-N curves were therefore proposed [80].
Residual stiffness and residual strength models were also developed to handle stochastic stress states. The residual stiffness approach treated random loadings as multilevel variable-amplitude processes [81]. Residual strength models were initially proposed for constant and two-level amplitudes [82], later extended to random load spectra by assuming probabilistic distributions of strength and fatigue life [83]. A probabilistic framework based on stress peak distributions and power spectral density was validated experimentally on plain weave carbon/epoxy laminates [84].
In addition to theoretical and numerical developments, experimental studies have provided valuable insights into the sensitivity of fatigue life to both loading and structural parameters. It has been demonstrated that vibration-induced fatigue is highly dependent on excitation characteristics such as root-mean-square levels, frequency bandwidth, and PSD amplitude. Structural factors including notches, through-holes, and ply stacking sequence were also shown to play a decisive role in damage accumulation and failure [85].

1.2.4 Structural theories for metallic and laminated structures

An alternative philosophy to overcome the challenges associated with the high computational cost of full three-dimensional models is the use of refined 1D or 2D

structural theories. They were originally developed for homogeneous and isotropic metallic structures, with the primary objective of achieving accurate predictions of global structural behavior at a reduced computational cost. Classical beam, plate, and shell theories have therefore played a central role in the analysis and design of metallic aerospace components, where the stress state is typically smooth through the thickness and three-dimensional effects are often of secondary importance. Classical one-dimensional (1D) beam theories, such as the Euler–Bernoulli Beam Theory (EBBT) [86] and Timoshenko Beam Theory (TBT) [87], as well as two-dimensional (2D) plate and shell theories, such as Kirchhoff's theory [88] and Reissner–Mindlin plate theory [89], have been extensively applied in engineering practice. However, these classical formulations suffer from limitations due to their restrictive kinematic assumptions. As a consequence, these formulations may become inadequate in nonlinear analyses driven by damage initiation, fatigue accumulation, or other mechanisms that are highly sensitive to local three-dimensional stress states.

To improve the predictive capabilities of 1D theories, several techniques have been proposed in the literature. A basic solution involves incorporating shear correction factors into classical beam theories [90]. More advanced formulations include the Generalised Beam Theory (GBT), in which the kinematics are described through cross-sectional deformation modes [91, 92]. The method has been successfully extended to the physical and geometrical nonlinear analysis of thin-walled structures [93, 94]. Another powerful approach is the Variational Asymptotic Beam Section (VABS) technique, which decomposes the three-dimensional elasticity problem into a 1D beam analysis along the structural axis and a 2D cross-sectional analysis. Asymptotic expansion methods are employed, with the structural geometry (e.g., thickness) used as the characteristic parameter [95, 96].

Similarly, significant research has been devoted to enhancing 2D plate and shell theories, particularly for composite laminates where through-thickness effects are of critical importance. The First-Order Shear Deformation Theory (FSDT), developed from the works of Reissner [89] and Mindlin [97], is widely implemented in commercial finite element codes. While FSDT accounts for transverse shear deformation, it assumes constant shear stresses through the plate thickness and does not include thickness stretching effects, limiting its accuracy for multilayered composite laminates. To address this limitation, Higher-Order Theories (HOT) have been proposed, which incorporate higher-order terms in the displacement field to more accurately represent through-thickness kinematics. Reddy has made significant contributions to this field [98, 99, 100], while alternative high-order formulations can be found in the works of Palazotto [101]. Similar higher-order kinematic enrichments have also been developed for beam theories, where refined displacement expansions enable an improved description of cross-sectional deformation and transverse shear effects, extending the applicability of classical 1D formulations to problems requiring enhanced three-dimensional stress accuracy [102].

A major advancement in the development of refined structural theories is the Carrera Unified Formulation (CUF), introduced by Carrera as a generalized framework for the systematic derivation of refined structural theories [103, 104, 105]. CUF provides a unified platform to generate both 1D (beam) and 2D (plate/shell) models of variable order without requiring case-by-case modification of the underlying structural theory. The formulation employs one-dimensional thickness expansion functions and two-dimensional cross-section expansion functions to represent the cross-sectional and through-thickness kinematics, enabling a full three-dimensional description of field variables with computational costs significantly lower than those of conventional 3D finite element models [106].
In the past twenty years, CUF have been employed in a broad spectrum of structural and multi-field applications including the free vibration analysis of composite beams and plates [107, 108], aeroelastic and flutter assessments of composite aerostructures [109, 110], and to various problems in rotordynamics [111]. Beyond purely structural contexts, CUF has also been adapted to multi-physics environments, providing effective models for thermo-mechanical and hygrothermal behaviour of layered materials [112, 113], for biomechanical systems [114], for the dynamic interaction of piezoelectric components [115], and for functionally graded members with both compact and thin-walled geometries [116]. In more recent developments, the framework has been exploited to tackle nonlinear scenarios, including large-deformation responses, post-buckling phenomena [117, 118], and inelastic effects such as hyperelasticity [119, 120] and elastoplasticity [121, 122]. The state of the art further highlights the creation of advanced micromechanical descriptions based on 1D-CUF models [123, 124], together with multiscale methodologies capable of addressing the linear and nonlinear performance of composite laminates [125, 125]. The capacity of CUF to operate within the progressive damage model has been demonstrated in recent years by Nagaraj et al. [33, 34]. The first step to evaluate the response of the structures under randomic loads by using CUF approach was developed by Filippi et al. [126].

1.3 Thesis outline

The thesis is organized into two main parts. Chapter 2 introduces the higher-order structural modeling framework adopted throughout the work. Building on this framework, Part I focuses on the analysis of progressive damage in composite structures, while Part II addresses fatigue life estimation under stochastic loading conditions. The content of the chapters is outlined below.

Chapter 2 introduces the Carrera Unified Formulation (CUF) as the structural modelling framework adopted in this thesis. The chapter presents the general formulation for refined one-dimensional and two-dimensional structural theories, describing the kinematic assumptions, the role of expansion functions through the thickness or

cross-section, and the formulation of the governing equations within the finite element method. The capability of CUF-based models to recover a three-dimensional stress state using reduced-order formulations is highlighted, providing the modelling foundation for the subsequent analyses.

Part I: Progressive damage analysis of composite structures

Chapter 3 presents the progressive damage modelling framework adopted for composite laminates and implemented on top of the CUF structural formulation. A continuum damage mechanics approach is described, and three-dimensional failure criteria are introduced, including the Hashin 3D orthotropic criterion for tensile damage and the combined Hashin–Puck formulation for compressive and matrix-dominated failure mechanisms.

Chapter 4 reports the numerical results obtained using the CUF-based progressive damage models under quasi-static loading conditions. Several benchmark configurations are analysed, and the discussion focuses on damage initiation, damage evolution, stiffness degradation and the influence of modelling choices on the predicted structural response and computational efficiency.

Part II: Fatigue life estimation in the frequency domain

Chapter 5 introduces the theoretical background required for fatigue analysis in the frequency domain, building upon the CUF-based structural response. Random vibration analysis is presented through power spectral densities, and the Dirlik method is described for estimating stress-range probability density functions. Fatigue assessment strategies are discussed for both metallic and composite structures, including the definition of an equivalent stress suitable for composite structures.

Chapter 6 addresses the modelling of stochastic aerodynamic loading and load assessment procedures. Gust-induced excitation is described using the von Kármán turbulence spectrum, and the associated aerodynamic load modelling is introduced, including the use of Küssner's function to account for unsteady aerodynamic effects.

Chapter 7 presents the numerical results of the fatigue analyses performed in the frequency domain using stress PSD obtained from CUF-based simulations. Metallic and composite structures are analysed under constant power spectral density excitation and under gust loading modelled using the von Kármán turbulence spectrum. The discussion highlights fatigue hot-spot identification, the influence of laminate stacking sequence, and comparisons with reference finite element solutions.

Conclusions

Chapter 8 summarizes the conclusions of the thesis and discusses the most relevant future perspectives, with particular emphasis on the role of CUF-based structural

models in enabling accurate progressive damage and frequency-domain fatigue analyses through the reconstruction of three-dimensional stress states.

Chapter 2

Unified formulation

This chapter introduces the Carrera Unified Formulation (CUF) and illustrates how it can be applied to the development of refined structural theories within the finite element framework. CUF enables the straightforward and automated construction of both one-dimensional (beam) and two-dimensional (plate and shell) theories. The chapter begins by outlining the notation, geometry, and variables, and then introduces the kinematic assumptions, material relations, and governing equations. The role of different classes of expansion functions in enhancing structural modeling is highlighted. Finally, the chapter introduces the explicit approach employed in the progressive damage model.

2.1 Geometrical and constitutive relations

Consider beam and plate structural model adopting a Cartesian reference system as in Fig. 2.1. For a beam, the beam axis coincides with y-direction, whereas the in-plane directions for a place coincide with $x - y$ directions.

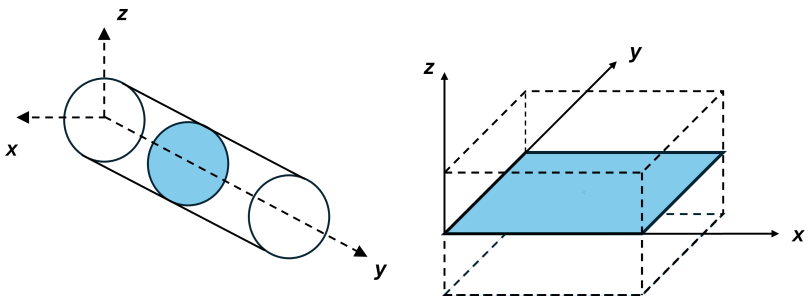

(a) **(b)**

Figure 2.1: Reference system and geometry of a) beam and b) plate.

The three-dimensional displacement components of a given point in the structural

domain is given by

$$\mathbf{u}(x, y, z) = \{\, u_x \; u_y \; u_z \,\}^T \tag{2.1}$$

Stresses, $\boldsymbol{\sigma}$, and strains, $\boldsymbol{\epsilon}$, are expressed in vectorial form. For beams and plates, they are written as:

$$\boldsymbol{\epsilon}^k = \{\epsilon^k_{xx},\, \epsilon^k_{yy},\, \epsilon^k_{zz},\, \epsilon^k_{xz},\, \epsilon^k_{yz},\, \epsilon^k_{xy}\}^{\mathrm{T}}, \tag{2.2}$$

$$\boldsymbol{\sigma}^k = \{\sigma^k_{xx},\, \sigma^k_{yy},\, \sigma^k_{zz},\, \sigma^k_{xz},\, \sigma^k_{yz},\, \sigma^k_{xy}\}^{\mathrm{T}}. \tag{2.3}$$

where the superscript k is the k-th layer if a laminate structure is considered and T is the trasponse operator. For beams and plates, stresses and strains are referred to a Cartesian coordinate system (x, y, z), where x and y lie in the structural plane, while z denotes the thickness direction. The corresponding stress and strain components are therefore expressed with respect to this global reference frame. Assuming small displacements and rotations, the strain-displacement relations are

$$\boldsymbol{\epsilon} = \mathbf{B}\mathbf{u} \tag{2.4}$$

where $\mathbf{B}$ is the linear differential operator matrix that follows:

$$\mathbf{B} = \begin{bmatrix} \partial_x & 0 & 0 \\ 0 & \partial_y & 0 \\ 0 & 0 & \partial_z \\ \partial_y & \partial_x & 0 \\ \partial_z & 0 & \partial_x \\ 0 & \partial_z & \partial_y \end{bmatrix} \tag{2.5}$$

The constitutive relation can be written as follows:

$$\sigma^k = \mathbf{C}^k \boldsymbol{\varepsilon}^k \tag{2.6}$$

$\mathbf{C}^k$ is the 6×6 material stiffness matrix. The stiffness matrix $\mathbf{C}^k$ for an orthotropic

material can be expressed as:

$$\mathbf{C}^k = \begin{bmatrix} C_{11}^k & C_{12}^k & C_{13}^k & 0 & 0 & 0 \\ & C_{22}^k & C_{23}^k & 0 & 0 & 0 \\ & & C_{33}^k & 0 & 0 & 0 \\ & & & C_{44}^k & C_{45}^k & 0 \\ & \text{sym} & & & C_{55}^k & 0 \\ & & & & & C_{66}^k \end{bmatrix} \tag{2.7}$$

The coefficients of the matrix $\mathbf{C}^k$ in Eq. (2.7) can be expressed in terms of nine independent constants, defined through the Young's moduli E_1, E_2, E_3, the shear moduli G_{12}, G_{13}, G_{23}, and the Poisson's ratios ν_{12}, ν_{13}, ν_{23}. Considering

$$\Delta = 1 - \nu_{12}\nu_{21} - \nu_{23}\nu_{32} - \nu_{13}\nu_{31} - 2\,\nu_{12}\nu_{23}\nu_{31}. \tag{2.8}$$

The components of the stiffness matrix $\mathbf{C}^k$ are given by:

$$\begin{aligned} C_{11}^k &= \frac{E_1\,(1-\nu_{23}\nu_{32})}{\Delta}, \\ C_{22}^k &= \frac{E_2\,(1-\nu_{13}\nu_{31})}{\Delta}, \\ C_{33}^k &= \frac{E_3\,(1-\nu_{12}\nu_{21})}{\Delta}, \\ C_{12}^k &= \frac{E_1\,(\nu_{21}+\nu_{31}\nu_{23})}{\Delta} = \frac{E_2\,(\nu_{12}+\nu_{13}\nu_{32})}{\Delta}, \\ C_{13}^k &= \frac{E_1\,(\nu_{31}+\nu_{21}\nu_{32})}{\Delta} = \frac{E_3\,(\nu_{13}+\nu_{12}\nu_{23})}{\Delta}, \\ C_{23}^k &= \frac{E_2\,(\nu_{32}+\nu_{12}\nu_{31})}{\Delta} = \frac{E_3\,(\nu_{23}+\nu_{21}\nu_{13})}{\Delta}. \end{aligned} \tag{2.9}$$

In the material reference system, the constitutive relation can be expressed as:

$$\boldsymbol{\sigma}^k = \mathbf{C}^k\,\boldsymbol{\varepsilon}^k \tag{2.10}$$

When transforming to a generic coordinate system, the stiffness matrix is obtained as:

$$\mathbf{C}^k = \mathbf{T}^{\mathrm{T}}\,\mathbf{C}^k\,\mathbf{T} \tag{2.11}$$

where $\mathbf{T}$ denotes the rotation matrix [127].

2.2 Carrera Unified Formulation

The Carrera Unified Formulation (CUF) provides a generalized hierarchical framework for the derivation of higher-order structural models in one and two dimensions, encompassing beams, plates, and shells. Its central idea lies in augmenting standard finite element interpolation functions with additional expansion functions, thereby enriching the kinematic representation of beam cross-sections and plate or shell thicknesses. Through this strategy, CUF enables the development of 1D and 2D models that achieve an accuracy comparable to full 3D finite element analyses, while demanding significantly lower computational resources [105].
In CUF, the 3D displacements field can be expressed as

$$\begin{aligned} \text{Beam:} \quad & \mathbf{u}^k(x,y,z) = F^k_\tau(x,z)\,\mathbf{u}^k_\tau(y), \quad \tau = 1,\ldots,M \\ \text{Plate:} \quad & \mathbf{u}^k(x,y,z) = F^k_\tau(z)\,\mathbf{u}^k_\tau(x,y), \quad \tau = 1,\ldots,M \end{aligned} \tag{2.12}$$

F_τ denotes a family of functions related to the cross-sectional coordinates (x, z) for beams and to the thickness expansion for plates. $\mathbf{u}_\tau$ is the generalized displacement vector, M is the expansion order, and the repeated index τ indicates summation. Thus, the parameters F_τ and M are defined as inputs and specify the structural theory applied in the formulation.
Over the last years, two major classes of expansion functions have been widely adopted: the Taylor Expansion (TE) and the Lagrange Expansion (LE). For laminated composite structures, two modeling strategies are generally employed: the Equivalent-Single-Layer approach (ESL) and the Layerwise approach (LW). The TE formulation employs a Taylor series either in $x - z$ (for beams) or in z (for plates, shells) as F_τ. The first-order Taylor expansion (TE1) for one-dimensional (1D) and two-dimensional (2D) models is shown below:

$$\begin{aligned} \text{1D:} \quad & u_x = u_{x1} + x u_{x2} + z u_{x3}, \\ & u_y = u_{y1} + x u_{y2} + z u_{y3}, \\ & u_z = u_{z1} + x u_{z2} + z u_{z3}, \\ \text{2D:} \quad & u_x = u_{x1} + z u_{x2}, \\ & u_y = u_{y1} + z u_{y2}, \\ & u_z = u_{z1} + z u_{z2}. \end{aligned} \tag{2.13}$$

More detailes about TE can be found in [118]. Lagrange Expansion (LE) models employ Lagrange polynomials to construct higher-order one- and two-dimensional theories, while the isoparametric formulation is adopted to handle arbitrary geometries. LE functions are used as F_τ functions over the cross-section in beam models and along the thickness direction in plate and shell models. In this study, three different polynomial sets were applied to both 1D and 2D formulations, as illustrated in Fig. 2.2.

Specifically, four-point (L4), nine-point (L9), and sixteen-point (L16) Lagrange poly-

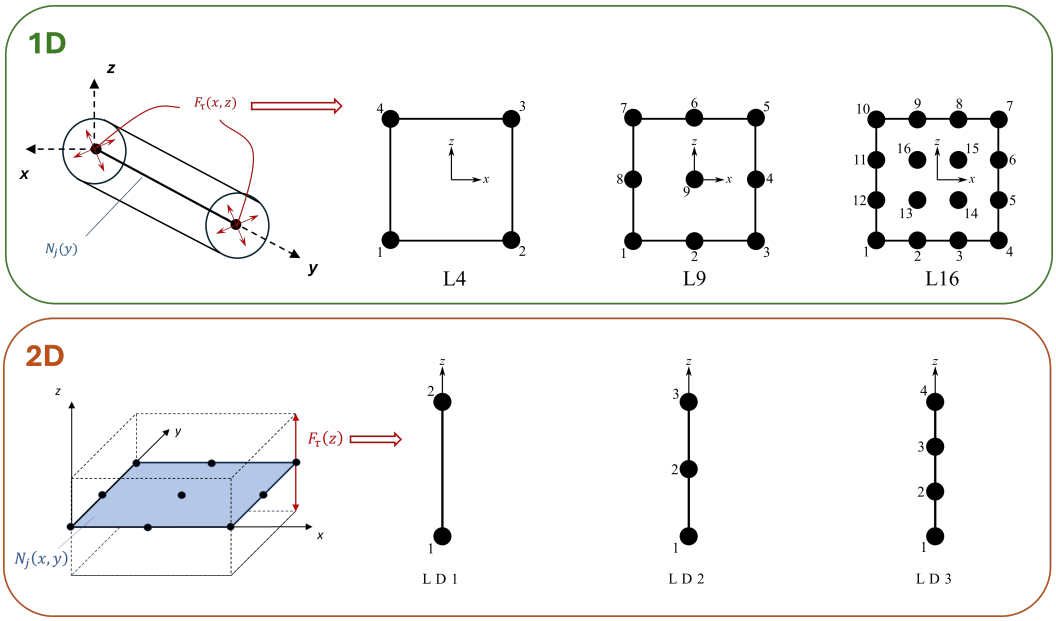

Figure 2.2: Lagrange expansion on the cross-section for 1D models (top) and thickness for 2D models (bottom).

nomials were employed to construct beam models ranging from linear to higher-order kinematics. For example, the bi-linear interpolation (L4) can be expressed as follows:

$$F_\tau = \frac{1}{4}\left(1 + rr_\tau\right)\left(1 + ss_\tau\right), \qquad \tau = 1,2,3,4 \tag{2.14}$$

In the bi-quadratic interpolation (L9), it is possible to write:

$$F_\tau = \frac{1}{4}\left(r^2 + rr_\tau\right)\left(s^2 + ss_\tau\right), \qquad \tau = 1,3,5,7 \tag{2.15}$$

$$F_\tau = \frac{1}{2}s_\tau^2\left(s^2 - ss_\tau\right)\left(1 - r^2\right) + \frac{1}{2}r_\tau^2\left(r^2 - rr_\tau\right)\left(1 - s^2\right), \qquad \tau = 2,4,6,8 \tag{2.16}$$

$$F_9 = \left(1 - r^2\right)\left(1 - s^2\right) \tag{2.17}$$

Finally, the equations for the bi-cubic interpolation (L16) is given below:

$$F_\tau = \frac{81}{256}\left(1 + rr_\tau\right)\left(1 + ss_\tau\right)\left(\frac{1}{9} - r^2\right)\left(\frac{1}{9} - s^2\right), \qquad \tau = 1,4,7,10 \tag{2.18}$$

$$F_\tau = \frac{243}{256}\left(1 - r^2\right)\left(s^2 - \frac{1}{9}\right)\left(\frac{1}{3} + 3rr_\tau\right)\left(1 + ss_\tau\right), \qquad \tau = 2,3,8,9 \tag{2.19}$$

$$F_\tau = \frac{243}{256}\left(1 - s^2\right)\left(r^2 - \frac{1}{9}\right)\left(\frac{1}{3} + 3ss_\tau\right)\left(1 + rr_\tau\right), \qquad \tau = 5,6,11,12 \tag{2.20}$$

$$F_\tau = \frac{729}{256}\left(1 - r^2\right)\left(1 - s^2\right)\left(\frac{1}{3} + 3rr_\tau\right)\left(\frac{1}{3} + 3ss_\tau\right), \qquad \tau = 13,14,15,16 \tag{2.21}$$

where r and s are the natural coordinates and vary from -1 to $+1$, whereas r_τ and s_τ are the coordinates of the Lagrange points.
For plates, the notation LDN (Lagrange Expansion, Displacement-based theory of order N) is introduced to identify different levels of refinement. For example, LD1, LD2, and LD3 correspond to linear (two-node), quadratic (three-node), and cubic (four-node) Lagrange expansion functions, respectively. These functions are applied along the thickness direction (z-axis) to generate CUF-based 2D models with progressively enriched kinematic descriptions. For the linear model LD1:

$$\begin{aligned} F_1 &= \frac{1}{2}(1-r), \\ F_2 &= \frac{1}{2}(1+r), \end{aligned} \qquad \begin{cases} r_1 = -1, \\ r_2 = 1, \end{cases} \tag{2.22}$$

For the parabolic model LD2:

$$\begin{aligned} F_1 &= \frac{1}{2}r(1-r), \\ F_2 &= -(1-r)(1+r), \\ F_3 &= \frac{1}{2}r(1+r), \end{aligned} \qquad \begin{cases} r_1 = -1, \\ r_2 = 0, \\ r_3 = 1, \end{cases} \tag{2.23}$$

For the cubic model LD3:

$$\begin{aligned} F_1 &= -\frac{9}{16}\left(r+\frac{1}{3}\right)\left(r-\frac{1}{3}\right)(r-1), \\ F_2 &= \frac{27}{16}(r-1)\left(r-\frac{1}{3}\right)(r+1), \\ F_3 &= -\frac{27}{16}(r+1)\left(r+\frac{1}{3}\right)(r-1), \\ F_4 &= \frac{9}{16}\left(r+\frac{1}{3}\right)\left(r-\frac{1}{3}\right)(r+1), \end{aligned} \qquad \begin{cases} r_1 = -1, \\ r_2 = -\frac{1}{3}, \\ r_3 = \frac{1}{3}, \\ r_4 = 1, \end{cases} \tag{2.24}$$

They are defined in the natural plane and r varies from -1 to +1.
Laminated structures are commonly analyzed using either the *Equivalent Single Layer* or the *Layer-Wise* approach. In the ESL formulation, the variables are formulated without dependence on the number of layers in the composite. The stiffness matrix is assembled by homogenizing the properties of the individual layers, i.e., by summing their contributions. Due to the heterogeneous nature of multilayered structures, ESL models inherently assume continuous transverse displacement fields through the thickness, which results in discontinuous transverse stress distributions at the interfaces between layers. Despite this limitation, ESL models are still widely adopted because of their conceptual simplicity and computational efficiency. In particular,

ESL theories are generally capable of providing accurate predictions of global structural responses. However, their accuracy significantly deteriorates when detailed three-dimensional stress fields are required. For clarity, Fig. 2.3 schematically illustrates the typical through-the-thickness behavior of the primary variables in a two-dimensional structure. Conversely, Layer-Wise (LW) theories discretize the displacement field sep-

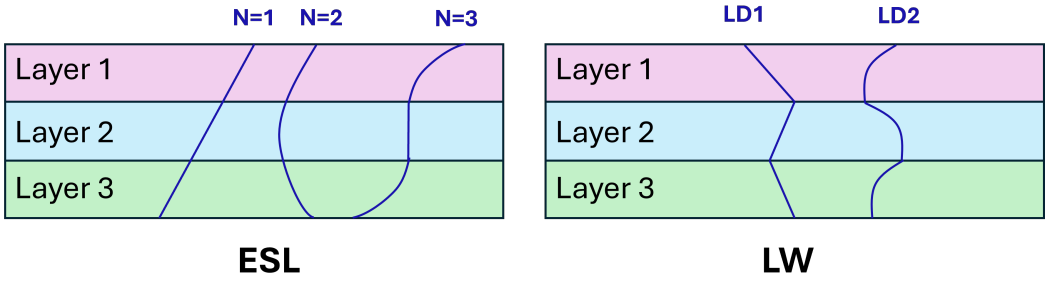

Figure 2.3: ESL (left) and LW (right) distributions of the primary variables through-the-thickness of a 2D model.

arately within each material layer. This approach naturally enforces displacement continuity at the layer interfaces, allowing for a more accurate description of both deformation and stress distributions through the thickness. In this framework, the homogenization process is effectively shifted to the interface level rather than being performed over the entire laminate. In this work, by adopting Lagrange Expansions (LE), the displacement components at the interpolation points of each layer are treated as independent unknowns, while interfacial compatibility conditions ensure continuity between adjacent layers. For completeness, the differences in the assembly procedures associated with ESL and LW formulations for a two-dimensional structure are illustrated in Fig. 2.4. The reader can found more detailed in [128].

2.3 Finite Element Method

The Finite Element Method (FEM) is adopted to solve the structural problem. Regardless of whether beam or plate kinematics are employed, the FEM is used to discretize the generalized displacement vector along the y-axis (for beams), or in the $x-y$ plane (for plates) as expressed below:

$$\begin{aligned} \text{Beams:} \quad & u_\tau^k(y) = N_i(y)\, q_{\tau i}^k, \qquad && i = 1, \ldots, N_n \\ \text{Plates:} \quad & u_\tau^k(x,y) = N_i(x,y)\, q_{\tau i}^k, \qquad && i = 1, \ldots, N_n \end{aligned} \tag{2.25}$$

where N_i are the shape functions, $q_{\tau i}$ represents the unknown nodal variables, N_n corresponds to the number of nodes per element, and i indicates summation. In this research, classical 2D finite elements (FEs) with four-node linear (Q4), nine-node quadratic (Q9) and sixteen-node cubic (Q16) are adopted for the shape functions in the

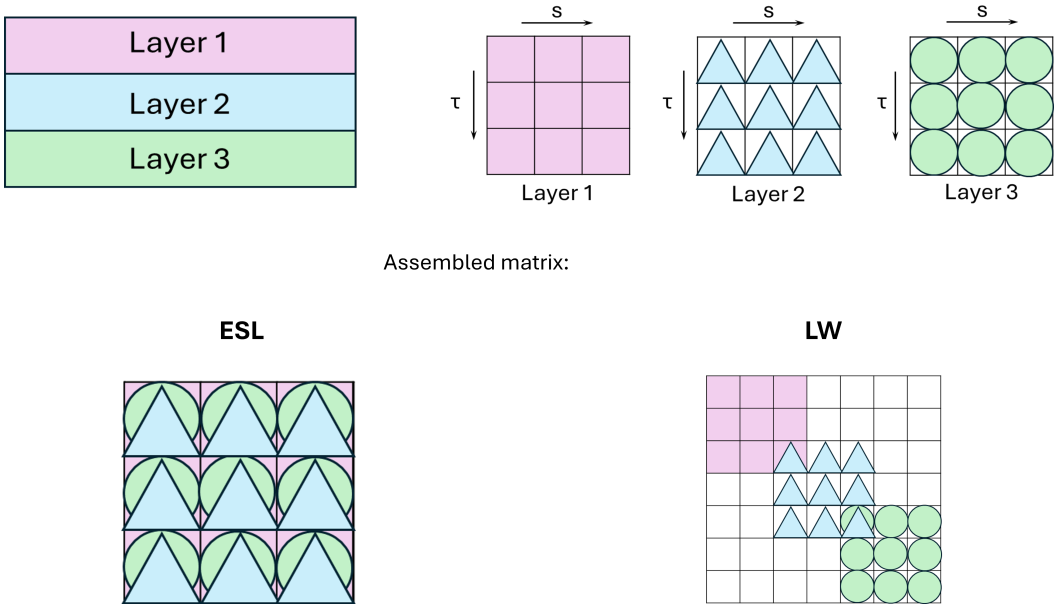

Figure 2.4: ESL and LW assembly schemes of the 2D model.

$x - y$. For the beam, this work employs two-node linear (B2) to four-node cubic (B4) finite elements. For the sake of completeness, the CUF and FEM model approximation of typical 1D and 2D structures is illustrated in Fig. 2.2. By the combination of the FE approximation, Eq. (2.25), with CUF, Eq. (2.12) , the 3D displacement field is defined by the following equation:

$$\begin{aligned} &\textit{Beam:} \quad \mathbf{u}^k(x,y,z) = F^k_\tau(x,z)N_i(y)q^k_{\tau i}, \qquad \tau = 1,\dots,M,\ i = 1,\dots,N_n \\ &\textit{Plate:} \quad \mathbf{u}^k(x,y,z) = F^k_\tau(z)N_i(x,y)q^k_{\tau i}, \qquad \tau = 1,\dots,M,\ i = 1,\dots,N_n \end{aligned} \tag{2.26}$$

2.4 Governing equations

For the sake of brevity, the governing equations are explicitly derived in the following section only for the beam formulation, while the corresponding expressions for plate structures can be found in [105]. According to the *Principle of Virtual Displacements (PVD)* [129], for a body in equilibrium the virtual work done by internal stresses and inertial loads equals the work done by external loads is expressed as:

$$\delta L_{\text{int}} = \delta L_{\text{ext}} - \delta L_{\text{ine}} \tag{2.27}$$

where δL_{int}, δL_{ext} and δL_{ine} represent the virtual variation of the strain energy, the virtual variation of the work of external loads, and the virtual variation of the inertial loads, respectively. The term related to the internal strain energy can be written as

follows:

$$\delta L_{\text{int}} = \int_V \delta \boldsymbol{\varepsilon}^{k\,T} \boldsymbol{\sigma}^k \, \mathrm{d}V = \int_V \delta \boldsymbol{\varepsilon}^{k\,T} \boldsymbol{C}^k \boldsymbol{\varepsilon}^k \, \mathrm{d}V \tag{2.28}$$

where V is the volume of the body. The strain-displacement relation (Eq. (2.4)) can be reformulated using Eq. (2.26):

$$\boldsymbol{\varepsilon} = \boldsymbol{B}_{\tau i} \, \boldsymbol{q}_{\tau i} \tag{2.29}$$

where the strain–displacement matrix in the case of beam, for example, is given by:

$$\mathbf{B}_{\tau i} = \begin{bmatrix} N_i F_{\tau,x} & 0 & 0 \\ 0 & N_{i,y} F_\tau & 0 \\ 0 & 0 & N_i F_{\tau,z} \\ 0 & N_i F_{\tau,z} & N_{i,y} F_\tau \\ N_i F_{\tau,z} & 0 & N_i F_{\tau,x} \\ N_{i,y} F_\tau & N_i F_{\tau,x} & 0 \end{bmatrix} \tag{2.30}$$

The virtual variation of the strain tensor can then be expressed as:

$$\delta \boldsymbol{\varepsilon} = \boldsymbol{B}_{sj} \, \delta \boldsymbol{q}_{sj} \tag{2.31}$$

Thus, the virtual variation of the internal strain energy reads:

$$\delta L_{\text{int}} = \delta \boldsymbol{q}_{sj}^T \int_V \boldsymbol{B}_{sj}^T \boldsymbol{C} \boldsymbol{B}_{\tau i} \, \mathrm{d}V \, \boldsymbol{q}_{\tau i} = \delta \boldsymbol{q}_{sj}^T \boldsymbol{k}_{ji\tau s} \boldsymbol{q}_{\tau i} \tag{2.32}$$

where $\boldsymbol{k}_{ji}^{\tau s}$ is a 3×3 matrix called the Fundamental Nucleus (FN) of the structural stiffness matrix. For the sake of clarity, the $k_{xx}^{ji\tau s}$ component is reported below:

$$k_{xx}^{ji\tau s} = \int_V \tilde{C}_{11} \frac{\partial}{\partial x}(N_j F_s) \frac{\partial}{\partial x}(N_i F_\tau) \, \mathrm{d}V + \int_V \tilde{C}_{16} \frac{\partial}{\partial x}(N_j F_s) \frac{\partial}{\partial y}(N_i F_\tau) \, \mathrm{d}V \tag{2.33}$$

$$+ \int_V \tilde{C}_{44} \frac{\partial}{\partial z}(N_j F_s) \frac{\partial}{\partial z}(N_i F_\tau) \, \mathrm{d}V + \int_V \tilde{C}_{16} \frac{\partial}{\partial y}(N_j F_s) \frac{\partial}{\partial x}(N_i F_\tau) \, \mathrm{d}V \tag{2.34}$$

$$+ \int_V \tilde{C}_{66} \frac{\partial}{\partial y}(N_j F_s) \frac{\partial}{\partial y}(N_i F_\tau) \, \mathrm{d}V \tag{2.35}$$

The remaining terms of the FN can be derived in an analogous manner in [105]. It is important to note that the formal expression of the FN remains the same regardless of the structural theory or FE scheme chosen. Therefore, any structural model can be created by simply looping on the indexes τ, i, j, and s. The virtual variation of the inertial loads is written as:

$$\delta L_{\text{ine}} = \delta \mathbf{q}_{sj}^T \int_V N_j F_s \, \rho \mathbf{I} \, N_i F_\tau \, dV \; \ddot{\mathbf{q}}_{\tau i} = \delta \mathbf{q}_{sj}^T \, \mathbf{m}_{ij}^{\tau s} \, \ddot{\mathbf{q}}_{\tau i}, \tag{2.36}$$

where $m^{\tau sij}$ is the Fundamental Nucleus of the mass matrix, evaluated in the same way as the structural stiffness. The virtual variation of the external work reads:

$$\delta L_{\text{ext}} = \int_V \delta \mathbf{u}^T \mathbf{g}\, dV + \int_S \delta \mathbf{u}^T \mathbf{q}\, dS + \int_l \delta \mathbf{u}^T \mathbf{r}\, dl + \delta \mathbf{u}^T \mathbf{P}_m, \tag{2.37}$$

where $\mathbf{g}$ is the body force per unit volume, $\mathbf{q}$ the surface force acting upon the surface S, $\mathbf{r}$ the line force, and $\mathbf{P}_m$ a concentrated point force exerted at point m. In discrete form, this becomes:

$$\delta L_{\text{ext}} = \delta \mathbf{u}_{sj} \left(\int_V N_j F^s \mathbf{g}\, dV + \int_S N_j F^s \mathbf{q}\, dS + \int_l N_j F^s \mathbf{r}\, dl + N_j F^s \mathbf{P}_m \right) = \delta \mathbf{u}_{sj}^T \mathbf{p}_j^s, \tag{2.38}$$

where $\mathbf{p}_j^s$ is the Fundamental Nucleus of the external force vector. Finally, the global stiffness and mass matrices, as well as the global force vector, are obtained by assembling the corresponding FNs over all finite elements and assuming undamped problems and a costant mass matrix, the governing equations for the elasticity problem are expressed as:

$$\mathbf{M}\, \ddot{\mathbf{q}} + \mathbf{K}\, \mathbf{q} = \mathbf{F} \tag{2.39}$$

Here, $\mathbf{K}, \mathbf{M}, \mathbf{F}$ represent the global stiffness matrix, mass matrix, and external force vector, respectively.

2.5 Explicit solution in CUF

Material and structural responses often require time-domain numerical strategies to efficiently solve the governing equations of motion. In this context, the dynamic problem can be addressed by adopting different time integration schemes, which are commonly classified into implicit and explicit approaches. In the present work, an explicit formulation is employed for the progressive damage analysis.
Explicit methods, due to their inherent formulation, typically avoid such difficulties. The semi-discrete balance of linear momentum can be expressed as:

$$\mathbf{M}\, \ddot{\mathbf{u}}^{\,t+\Delta t} = \mathbf{F}_{\text{ext}}^{t+\Delta t} - \mathbf{F}_{\text{int}}^{t+\Delta t} \tag{2.40}$$

where $\mathbf{M}$ is the mass matrix, $\mathbf{F}_{\text{ext}}$ is the external force vector, and $\mathbf{F}_{\text{int}}$ is the internal force vector. Eq. (2.40) is typically solved using the central-difference time integration scheme [130]. The velocity within a time step is approximated at its mid-interval as:

$$\dot{\mathbf{u}}^{\,t+\frac{1}{2}\Delta t} = \frac{\mathbf{u}^{t+\Delta t} - \mathbf{u}^t}{\Delta t} \tag{2.41}$$

where $\mathbf{u}$ and $\dot{\mathbf{u}}$ are the displacement and velocity vectors, respectively, and Δt is the time increment.

Eq. (2.41) can be reformulated to update the displacement field:

$$\mathbf{u}^{t+\Delta t} = \mathbf{u}^{t} + \Delta t\, \dot{\mathbf{u}}^{t+\frac{1}{2}\Delta t} \tag{2.42}$$

The updated displacements are then used to compute the strain field and, consequently, the updated stress field. From the updated stress tensor, the internal force vector can be evaluated as:

$$\mathbf{F}_{\text{int}}^{t+\Delta t} = \int_{V} \mathbf{B}^{T}\, \boldsymbol{\sigma}^{t+\Delta t}\, dV \tag{2.43}$$

where $\mathbf{B}^{T}$ is the transpose of the strain-displacement matrix introduced in Section 2.3. The acceleration is obtained by rearranging Eq.(2.40):

$$\ddot{\mathbf{u}}^{t+\Delta t} = \mathbf{M}^{-1} \left(\mathbf{F}_{\text{ext}}^{t+\Delta t} - \mathbf{F}_{\text{int}}^{t+\Delta t} \right) \tag{2.44}$$

The mid-interval velocity at the next time step is then updated as:

$$\dot{\mathbf{u}}^{t+\frac{3}{2}\Delta t} = \dot{\mathbf{u}}^{t+\frac{1}{2}\Delta t} + \Delta t\, \ddot{\mathbf{u}}^{t+\Delta t} \tag{2.45}$$

Finally, the solution of the first time step ($t = 0$) requires the initial mid-interval velocity $\dot{\mathbf{u}}^{\frac{1}{2}\Delta t}$, which can be estimated as:

$$\dot{\mathbf{u}}^{\frac{1}{2}\Delta t} = \dot{\mathbf{u}}^{0} + \frac{1}{2}\Delta t\, \ddot{\mathbf{u}}^{0} \tag{2.46}$$

where $\dot{\mathbf{u}}^{0}$ and $\ddot{\mathbf{u}}^{0}$ are the prescribed initial velocity and acceleration of the system, respectively, as determined from the initial conditions.

Part I

Progressive damage analysis of composite structure using 3D failure criteria

Chapter 3

Damage model

This chapter presents the modeling framework adopted for the analysis of composite materials, building on previous developments based on the CODAM2 formulation and its implementation within the CUF. The present study extends this framework by incorporating the Hashin 3D orthotropic failure criteria together with Puck's criteria for matrix compression, implemented within a 2D finite element formulation.

3.1 Damage framework

The constitutive damage models adopted in this work are selected from well-established literature contributions. The novelty of the present research lies in their implementation within the CUF and in the validation of refined structural models able to reconstruct local three-dimensional stress states and reproduce damage evolution with reduced computational cost. Therefore, the purpose of the thesis is not to provide a comprehensive treatment of all nonlinear phenomena that may affect the structural response, but rather to assess the suitability of CUF-based models for progressive damage analyses in aerospace structures. In this perspective, stiffness degradation is mainly related to constitutive damage evolution, while additional nonlinear effects associated with large geometric changes, boundary-condition modifications, or strong local kinematic discontinuities are outside the scope of the present implementation. Accordingly, although the damage variables act through a reduction of the elastic components, the adopted model is intended to capture the macroscopic and progressive loss of stiffness in a phenomenological sense, consistently with established literature formulations, rather than to explicitly resolve all the micromechanical features involved in gradual material degradation.

3.1.1 Tensile damage model

The tensile damage behavior of fiber-reinforced composites is modeled within the framework of CDM. The onset of fiber tensile failure is governed by the Hashin 3D

criterion [36], which states that damage initiates when the failure index $F_{ft} \geq 1$, with

$$F_{ft} = \left(\frac{\sigma_{11}}{X_T}\right)^2 + \alpha_f \left[\left(\frac{\sigma_{12}}{S_{12}}\right)^2 + \left(\frac{\sigma_{13}}{S_{13}}\right)^2\right], \tag{3.1}$$

where X_T is the fiber tensile strength, S_{12} and S_{13} are the in-plane and out-of-plane shear strengths, respectively, and α_f is an interaction coefficient, set to zero unless otherwise specified. Similarly, matrix tensile damage initiates when $F_{mt} \geq 1$, where the corresponding Hashin criterion is

$$F_{mt} = \left(\frac{\sigma_{22} + \sigma_{33}}{Y_T}\right)^2 + \frac{1}{S_{23}^2}\left(\sigma_{23}^2 - \sigma_{22}\sigma_{33}\right) + \left(\frac{\sigma_{12}}{S_{12}}\right)^2 + \left(\frac{\sigma_{13}}{S_{13}}\right)^2, \tag{3.2}$$

with Y_T being the transverse tensile strength and S_{23} the transverse shear strength. Once the failure indices reach unity, the damage progression is described in terms of equivalent displacements for fibers and matrix. For fiber tension, the equivalent displacement is

$$\delta_{eq}^{ft} = l_c \sqrt{\langle \epsilon_{11} \rangle^2 + \epsilon_{12}^2 + \epsilon_{13}^2}, \tag{3.3}$$

while for matrix tension it is

$$\delta_{eq}^{mt} = l_c \sqrt{\langle \epsilon_{22} \rangle^2 + \langle \epsilon_{33} \rangle^2 + \epsilon_{12}^2 + \epsilon_{23}^2 + \epsilon_{13}^2}, \tag{3.4}$$

where l_c is the characteristic length set equal to the cubic root of the Gauss point volume , $\mathrm{l}_C = (\mathrm{V}_{GP})^{1/3}$, and $\langle \cdot \rangle$ denotes the Macaulay bracket, ensuring that only tensile strains contribute. The equivalent stresses are

$$\sigma_{eq}^{ft} = \frac{l_c \left(\langle \sigma_{11} \rangle \langle \epsilon_{11} \rangle + \sigma_{12}\epsilon_{12} + \sigma_{13}\epsilon_{13}\right)}{\delta_{eq}^{ft}}, \tag{3.5}$$

$$\sigma_{eq}^{mt} = \frac{l_c \left(\langle \sigma_{22} \rangle \langle \epsilon_{22} \rangle + \langle \sigma_{33} \rangle \langle \epsilon_{33} \rangle + \sigma_{12}\epsilon_{12} + \sigma_{23}\epsilon_{23} + \sigma_{13}\epsilon_{13}\right)}{\delta_{eq}^{mt}}. \tag{3.6}$$

The constitutive relation between equivalent stress and displacement is depicted in Fig. 3.1. The ultimate equivalent displacements at damage saturation are related to the fracture energies G_f and G_m as

$$\delta_{eq}^{u,f} = \frac{2G_f}{X_T}, \qquad \delta_{eq}^{u,m} = \frac{2G_m}{T}, \tag{3.7}$$

where T denotes the peak equivalent transverse stress at the onset of matrix damage, i.e. $T = \sigma_{eq}^{mt}\big|_{F_{mt}=1}$. The damage variable d governs the stiffness degradation and is expressed as

$$d = \frac{\delta_{eq}^u \left(\delta_{eq} - \delta_{eq}^0\right)}{\delta_{eq}(\delta_{eq}^u - \delta_{eq}^0)}, \tag{3.8}$$

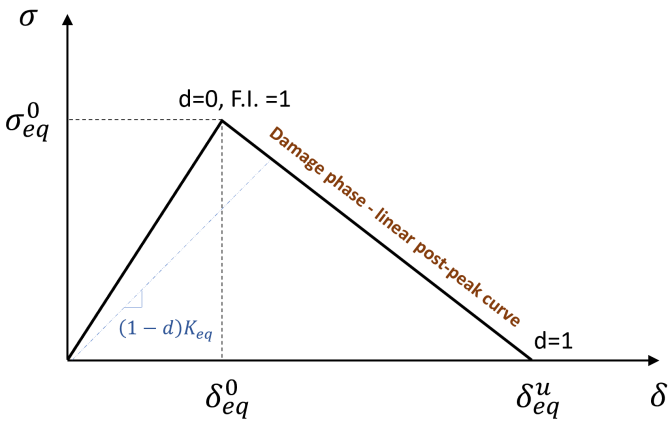

Figure 3.1: Constitutive equivalent stress-displacement relation for tensile damage.

where $\delta^0_{eq} = \delta_{eq}|_{F=1}$ is the displacement at damage initiation. Accordingly, the stiffness matrix in the damaged state, $\mathbf{C}^{dam}$, is

$$\mathbf{C}^{dam} = \frac{1}{\Delta}\begin{bmatrix} C_{11} & C_{12} & C_{13} & 0 & 0 & 0 \\ C_{21} & C_{22} & C_{23} & 0 & 0 & 0 \\ C_{31} & C_{32} & C_{33} & 0 & 0 & 0 \\ 0 & 0 & 0 & C_{44} & 0 & 0 \\ 0 & 0 & 0 & 0 & C_{55} & 0 \\ 0 & 0 & 0 & 0 & 0 & C_{66} \end{bmatrix}, \tag{3.9}$$

where

$$\Delta = 1-(1-d_f)(1-d_m)\nu_{12}\nu_{21}-(1-d_m)\nu_{23}\nu_{32}-(1-d_f)\nu_{13}\nu_{31}-2(1-d_f)(1-d_m)\nu_{21}\nu_{32}\nu_{13}.$$

The effective damage parameters for fiber and matrix are defined as

$$d_f = 1-(1-d_{ft})(1-d_{fc}), \qquad d_m = 1-(1-d_{mt})(1-d_{mc}), \tag{3.10}$$

where d_{ft} and d_{mt} refer to fiber and matrix tension, while d_{fc} and d_{mc} account for fiber and matrix compression. Finally, the matrix components of $\mathbf{C}^{dam}$ are

$$\begin{aligned} C_{11} &= [1-(1-d_m)\nu_{23}\nu_{32}](1-d_f)E_1, & C_{12} &= (1-d_f)(1-d_m)(\nu_{21}+\nu_{23}\nu_{31})E_1, \\ C_{22} &= [1-(1-d_f)\nu_{31}\nu_{13}](1-d_m)E_2, & C_{13} &= (1-d_f)(\nu_{31}+(1-d_m)\nu_{21}\nu_{32})E_1, \\ C_{33} &= [1-(1-d_f)(1-d_m)\nu_{21}\nu_{12}]E_3, & C_{23} &= (1-d_m)(\nu_{32}+(1-d_f)\nu_{12}\nu_{31})E_2, \\ C_{44} &= \Delta(1-d_f)(1-d_m)G_{12}, & C_{55} &= \Delta G_{23}, \\ C_{66} &= \Delta G_{13}. \end{aligned} \tag{3.11}$$

Thus, the constitutive relation in the damaged state becomes

$$\boldsymbol{\sigma} = \mathbf{C}^{dam}\boldsymbol{\epsilon}. \tag{3.12}$$

3.1.2 Compressive damage model

The present work employs the Hashin 3D criteria to describe fiber and matrix damage under tensile and fiber under compressive states, while for matrix compression the Puck criterion is adopted, following the approaches of Davila et al. [32] and Lapczyk et al. [131]. The initiation of fiber damage in compression occurs when the failure index $F_{fc} \geq 1$, with

$$F_{fc} = \left(\frac{\sigma_{11}}{X_C}\right)^2, \tag{3.13}$$

where X_C denotes the fiber compressive strength. The Puck criterion, according to which initiation occurs when $F_{mc} \geq 1$, where

$$F_{mc} = \left(\frac{\sigma_{nt}}{S_{23}^A - \eta_{nt}\sigma_{nn}}\right)^2 + \left(\frac{\sigma_{nl}}{S_{12} - \eta_{nl}\sigma_{nn}}\right)^2. \tag{3.14}$$

The coefficients η_{nl} and η_{nt} represent the internal material friction according to the Mohr-Coulomb theory [19]. Here, σ_{nn}, σ_{nl} and σ_{nt} are the stresses acting on the fracture plane in the normal, longitudinal shear and transverse shear directions, respectively; S_{12} is the in-plane shear strength, and S_{23}^A the transverse shear strength in the fracture plane, are computed as

$$\begin{aligned}
\sigma_{nn} &= \sigma_{22}\cos^2\theta + \sigma_{33}\sin^2\theta + 2\sigma_{23}\cos\theta\sin\theta, \\
\sigma_{nl} &= \sigma_{12}\cos\theta + \sigma_{13}\sin\theta, \\
\sigma_{nt} &= -\sigma_{22}\cos\theta\sin\theta + \sigma_{33}\cos\theta\sin\theta + 2\sigma_{23}(2\cos^2\theta - 1), \\
\mu_{nt} &= \tan(2\theta - 90^\circ), \quad \frac{\mu_{nt}}{S_{23}^A} = \frac{\mu_{nl}}{S_{12}}, \quad S_{23}^A = \frac{Y_C}{2}\left(\frac{1-\sin\phi}{\cos\phi}\right), \quad \phi = 2\theta - 90^\circ.
\end{aligned} \tag{3.15}$$

The angle θ denotes the fracture inclination, typically around 53° for unidirectional composites under transverse compression [132]. In this work, θ is obtained through the Simple Parabolic Interpolation Search (SPIS) algorithm [133], which divides the 180° interval into 18 sub-intervals, each with 19 reference points (see Fig.3.2). For each reference orientation θ, an equivalent failure index $f_e(\theta)$ is evaluated from the local stress state according to the adopted failure criterion. The quantity f_e provides a scalar measure of the proximity to material failure, with $f_e = 1$ identifying the onset of damage. Since different fracture mechanisms may become dominant depending on the inclination angle, the failure response exhibits a pronounced directional dependence. The progressive damage variable is therefore expressed as a two-parameter function $f = f(f_e, \theta)$, which combines the magnitude of the equivalent failure index with the

orientation of the fracture plane. Within the SPIS framework, discrete evaluations of f_e are obtained at the prescribed reference angles, and a continuous representation of the function $f(f_e, \theta)$ is reconstructed through parabolic interpolation over the angular domain. This procedure allows the fracture inclination θ corresponding to the maximum damage driving force to be identified in a robust and computationally efficient manner, while avoiding the need for an exhaustive angular search. Damage progres-

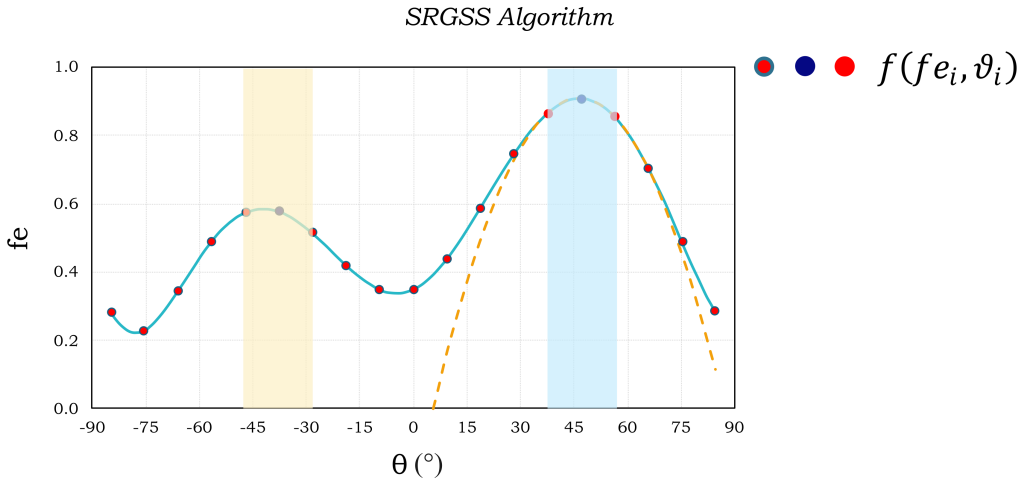

Figure 3.2: Example of the SPIS method based on [133].

sion is described in terms of the equivalent compressive displacements δ_{eq}^{fc} and δ_{eq}^{mc} for fibers and matrix, respectively:

$$\delta_{eq}^{fc} = l_c \langle -\epsilon_{11} \rangle, \tag{3.16}$$

$$\delta_{eq}^{mc} = l_c \sqrt{\langle -\epsilon_{22} \rangle^2 + \langle -\epsilon_{33} \rangle^2 + \epsilon_{12}^2 + \epsilon_{23}^2 + \epsilon_{13}^2}, \tag{3.17}$$

where $\langle \cdot \rangle$ is the Macaulay bracket and $l_c = (V_{GP})^{1/3}$ is the characteristic length associated with the Gauss point volume V_{GP}. The corresponding equivalent stresses are defined as

$$\sigma_{eq}^{fc} = \frac{l_c \langle -\sigma_{11} \rangle \langle -\epsilon_{11} \rangle}{\delta_{eq}^{fc}}, \tag{3.18}$$

$$\sigma_{eq}^{mc} = \frac{l_c \left(\langle -\sigma_{22} \rangle \langle -\epsilon_{22} \rangle + \langle -\sigma_{33} \rangle \langle -\epsilon_{33} \rangle + \sigma_{12}\epsilon_{12} + \sigma_{23}\epsilon_{23} + \sigma_{13}\epsilon_{13} \right)}{\delta_{eq}^{mc}}. \tag{3.19}$$

The ultimate equivalent displacements at damage saturation are given by

$$\delta_{eq}^{u,f} = \frac{2G_f}{T}, \qquad \delta_{eq}^{u,m} = \frac{2G_m}{T}, \tag{3.20}$$

where G_f and G_m are the fracture energies in the longitudinal and transverse directions, respectively, and T is the peak equivalent stress at damage onset. The scalar damage variable d governs stiffness degradation during evolution:

$$d = \frac{\delta_{eq}^{u}\,(\delta_{eq} - \delta_{eq}^{0})}{\delta_{eq}(\delta_{eq}^{u} - \delta_{eq}^{0})}, \tag{3.21}$$

with $\delta_{eq}^{0} = \delta_{eq}\big|_{F=1}$ being the displacement at damage initiation. The damage parameter d and the stiffness matrix in the damage state $\mathbf{C}^{dam}$ are computed as for the tensile case.

The bi-linear constitutive models with linear softening often fail to capture the complex post-peak compressive response, dominated by micro-buckling and kink-band formation, which cause a sharp strength drop followed by a stress plateau [134]. Enhanced damage evolution laws including linear-brittle softening curves have been proposed [135], enabling a more realistic representation of compressive failure. The curves introduce a residual plateau stress, defined as a fraction of the peak value, thus allowing to generate families of responses while preserving fracture energy. An example of such curves is illustrated in Fig. 3.3.

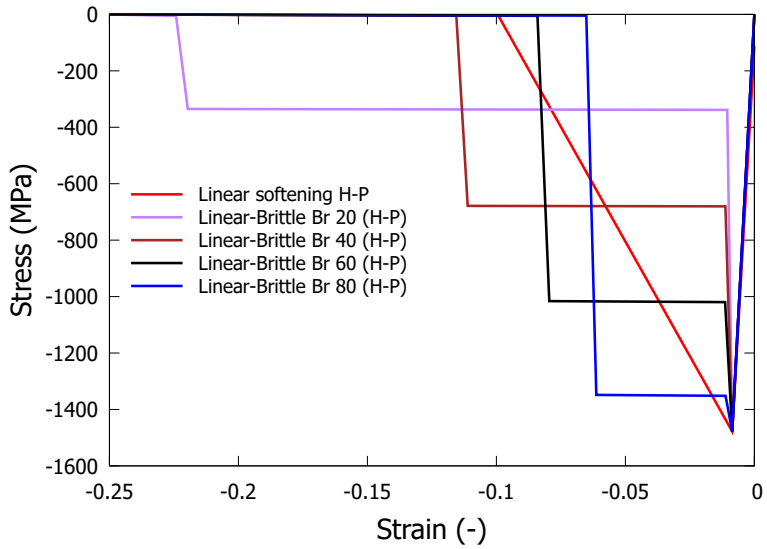

Figure 3.3: Family of softening curves for compressive damage using Hashin-Puck (H-P) criteria.

Chapter 4

Numerical results of progressive damage

This chapter presents numerical case studies under tensile and compressive loading, taken from the literature. For tension, the accuracy and efficiency of the 3D Hashin damage model combined with 2D CUF theories are evaluated against the CODAM2 model, 2D Hashin criteria, experimental results, and Abaqus analyses. For compression, simulations developed with the combined Hashin 3D–Puck (H-P) criteria are compared with alternative modeling approaches and experiments. The overall aim is to verify, validate, and assess the proposed methods in terms of accuracy and numerical efficiency. The results related to tensile loading case are present in [136], whereas the compressive loading case are discussed in [137].

4.1 Tensile loading cases

4.1.1 Single element

The first benchmark case examines a single square element of 1 mm × 1 mm to verify the predictive capability of the damage model. The material system is the IM7/8552 carbon fiber reinforced polymer (CFRP) with a ply thickness of 0.125 mm, whose properties are listed in Table 4.1.

Table 4.1: Material properties of IM7/8552.

E_1 (GPa)	E_2 (GPa)	E_3 (GPa)	G_{12} (GPa)	G_{13} (GPa)	G_{23} (GPa)	ν_{12}	ν_{13}	ν_{23}
150.0	11.0	11.0	5.8	5.8	2.9	0.34	0.34	0.48
X_T (MPa)	X_C (MPa)	Y_T (MPa)	Y_C (MPa)	S_{12} (MPa)	G_1^T (kJ/m^2)	G_2^T (kJ/m^2)	G_1^C (kJ/m^2)	G_2^C (kJ/m^2)
2560	1960	73	250	90	120	2.6	80.0	4.2

The structural model employs a Q4 element with ply-thickness kinematics described by LE1 [33]. Three conditions are investigated: (i) uniaxial tension in the

longitudinal direction with fibers aligned to y, (ii) transverse loading with fibers perpendicular to y, and (iii) a quasi-isotropic $[90/45/0/-45]_{2s}$ laminate. Stress–strain curves are reported in Fig. 4.1, including results from four approaches: Hashin 3D with CUF, CODAM2 with CUF [33], CODAM2 with LS-Dyna [29], and Hashin 3D with Abaqus continuum shell elements. Equivalent strains and stresses at damage initiation (ϵ^0_{eq}, σ^0_{eq}) and the ultimate strain (ϵ^u_{eq}) are summarized in Table 4.2. The verification on the single element highlights two main findings:

1. The peak stresses predicted by the present model match the fiber and matrix strengths; after the peak, the response degrades linearly until the saturation strain.

2. Across the three loading cases, all four modeling strategies yield very similar stress–strain curves.

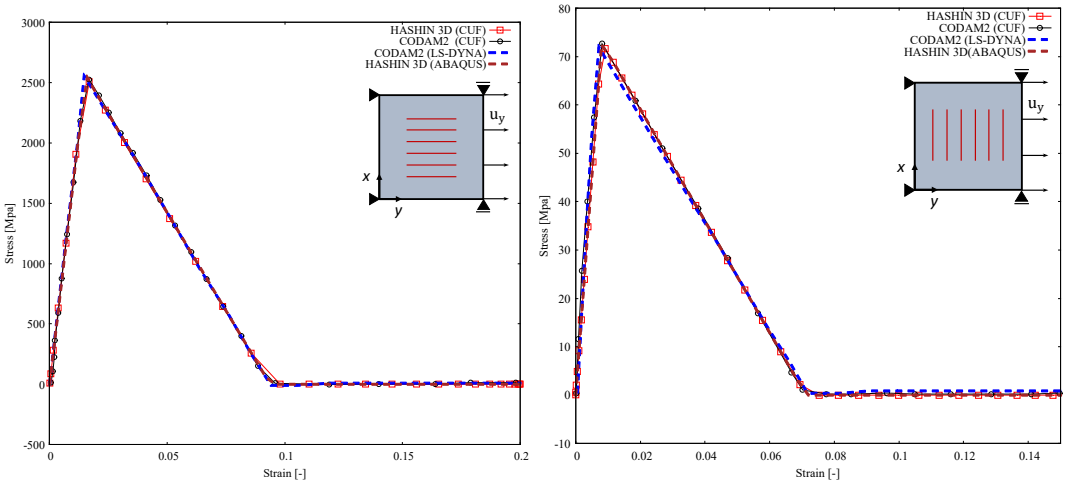

(a) Longitudinal loading

(b) Transverse loading

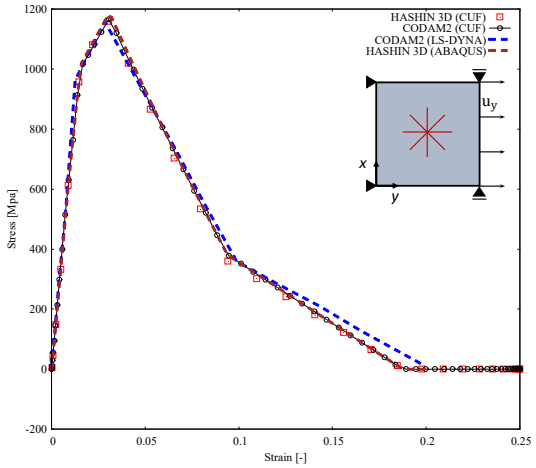

(c) Quasi-isotropic laminate

Figure 4.1: Stress–strain response of the single element under uniaxial traction.

Table 4.2: Comparison of equivalent strains and stresses at damage initiation and ultimate strain for the single element $[90/45/0/-45]_{2s}$.

	Hashin 3D/CUF	CODAM2/CUF	CODAM2/LS-Dyna	Hashin 3D/Abaqus
ϵ^0_{eq}	0.028	0.028	0.027	0.027
ϵ^u_{eq}	0.185	0.186	0.199	0.185
σ^0_{eq} (MPa)	1166.3	1166.2	1165.9	1165.8

4.1.2 Center-notched specimen

The second numerical case examines a center-notched specimen subjected to tensile loading, following the setup described in [29], which investigates size effects. The notch length is $C = 25.4$ mm, the gauge width $W = 127$ mm, and the gauge length $L = 508$ mm. The boundary conditions and geometry are shown in Fig. 4.2, where the specimen is clamped at one edge and a displacement along the y-direction is applied at the free edge. The material system is IM7/8552 CFRP, with ply properties given in Table 4.1. The stacking sequence is $[45/90/-45/0]_{4s}$ with a ply thickness of 0.125 mm. Numerical results are compared with models from [29], including LS-Dyna using CODAM2 and an Abaqus-based Ladeveze damage model (ABQ-DLR), which describes fiber damage evolution through an exponential softening law. Experimental data from [138] are also used for validation. Figure 4.3 shows the stress–strain curves obtained using the

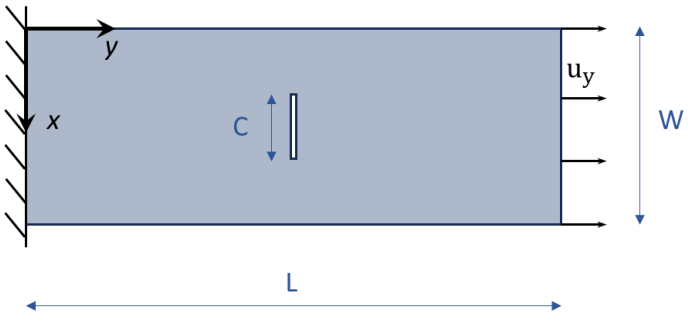

Figure 4.2: Boundary conditions and geometry of the center-notched specimen under tension

3D Hashin criteria, highlighting the effect of mesh refinement with 9-node elements ranging from 74 to 184 elements. The expansion order through the thickness also increases from linear (LE1) to cubic (LE3). These results are compared against the minimum and maximum experimental strength values [138]. Table 4.3 summarizes the degrees of freedom (DOF) of each model and the equivalent strains and stresses at damage initiation. Figure 4.4 shows a comparison with CODAM2 results from CUF [33] and LS-Dyna [29]. Figure 4.5 shows the stress–strain response for the specimen with 132 Q9 LE1 elements for $\alpha_f = 0$ and $\alpha_f = 1$. The former removes the shear stress contribution, whereas the latter includes it. The two curves overlap almost perfectly, indicating a negligible effect of fiber shear stresses. The final set of results explores the effect of specimen scale on computational cost. The specimen dimensions for different

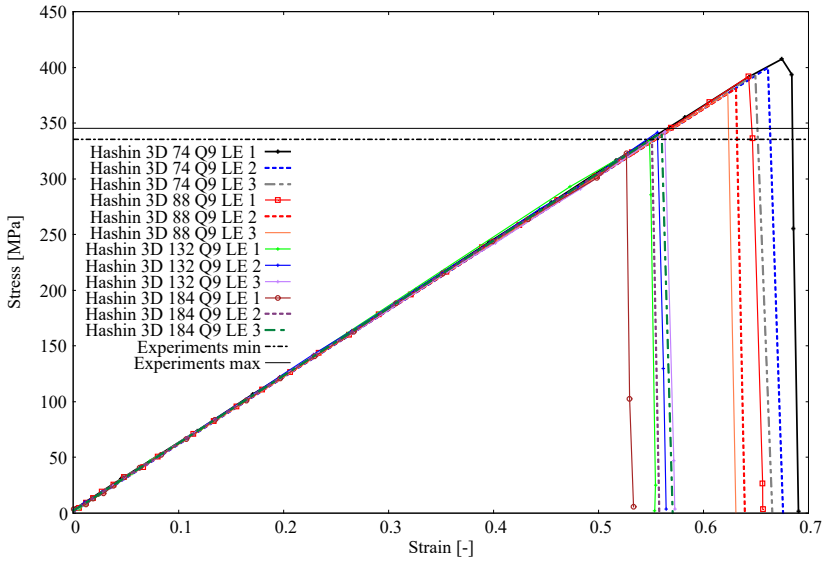

Figure 4.3: Mesh and structural theory convergence for the stress–strain response of the center-notched specimen

Table 4.3: DOF and equivalent strains and stresses at damage initiation for the center-notched specimen

	74Q9-LE1	88Q9-LE1	132Q9-LE1	132Q9-LE2	132Q9-LE3	184Q9-LE1	Exp. min	Exp. max
DOF	33660	39600	61380	120900	180420	79200		
ϵ^0_{eq}	0.675	0.643	0.548	0.555	0.563	0.526		
σ^0_{eq} (MPa)	407.6	392.1	334.4	341.8	342.5	323.2	335.4	345.2

scales are listed in Table 4.4, where C is the notch length, W the width, and L the gauge length. Figure 4.6 shows the maximum peak stress for each scale, compared with CODAM2 models [33, 29] and experimental data [138], with the percentage errors reported in Table 4.5. Figure 4.7 reports the DOF and computational time for each scale and model, normalized relative to scale 1. Differences in DOF with [33] arise because plies with the same orientation were combined into a single LE1 element in their approach. The results indicate that:

1. The Hashin 3D model provides results similar to CODAM2, while being closer to experimental values.

2. Increasing the order of the structural theory improves agreement with experiments. Mesh refinement alone does not guarantee accuracy, emphasizing the importance of structural theory as shown in Fig. 4.3.

3. The stress–strain curves with and without fiber shear contributions are nearly identical, demonstrating that fiber shear effects are negligible (Fig. 4.5).

4. Table 4.5 shows that CODAM2-CUF exhibits more pronounced size effects due to its damage evolution mechanism, whereas Hashin 3D-CUF shows a smoother

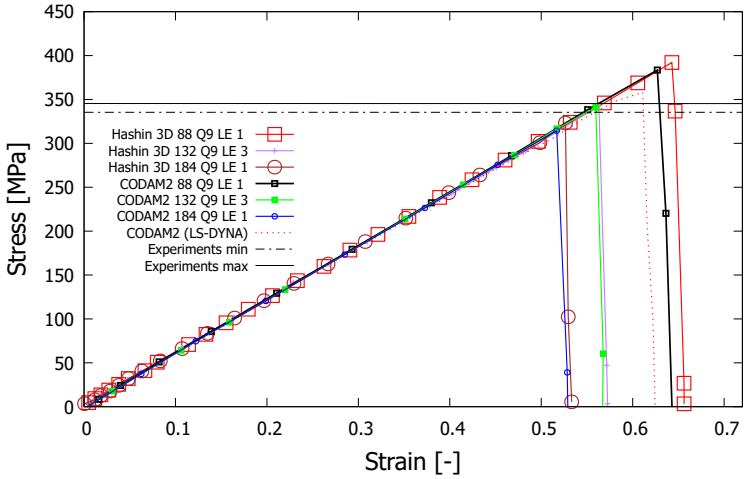

Figure 4.4: Stress–strain curves of the center-notched specimen using Hashin 3D and CODAM2

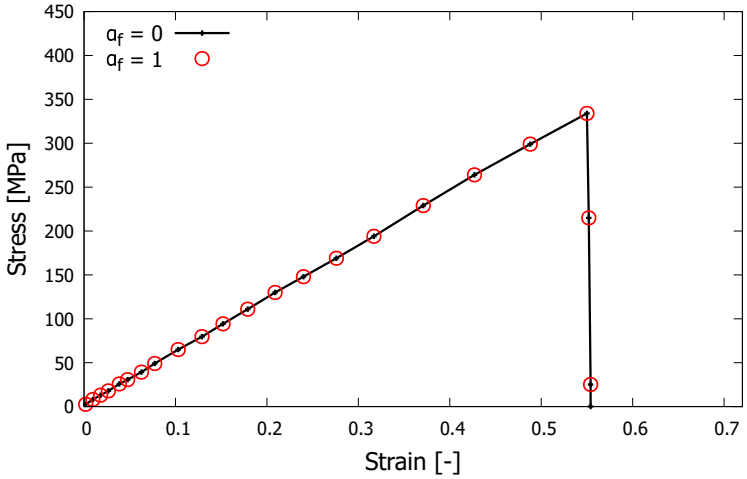

Figure 4.5: Stress–strain response of the center-notched specimen, 132 Q9 LE1, $\alpha_f = 0$ and $\alpha_f = 1$

trend.

5. CUF models are less sensitive to specimen size in terms of computational cost compared to standard finite element approaches, as coarser meshes with higher-order through-thickness kinematics can be employed [33].

4.1.3 Over-height compact tension Test

The final numerical case focuses on an over-height compact tension (OCT) specimen with a ply sequence of $[90/45/0/-45]_{4s}$. The geometry and boundary conditions are illustrated in Fig. 4.8, based on [33]. The pins are opened gradually up to a displacement of 1 mm. Numerical results are compared with experimental data from

Table 4.4: Specimen dimensions (mm) for different scales

Scale	C	W	L
1	3.2	15.9	63.5
2	6.4	31.8	127.0
4	12.7	63.5	254.0
8	25.4	127.0	508.0
16	50.8	254.0	508.0

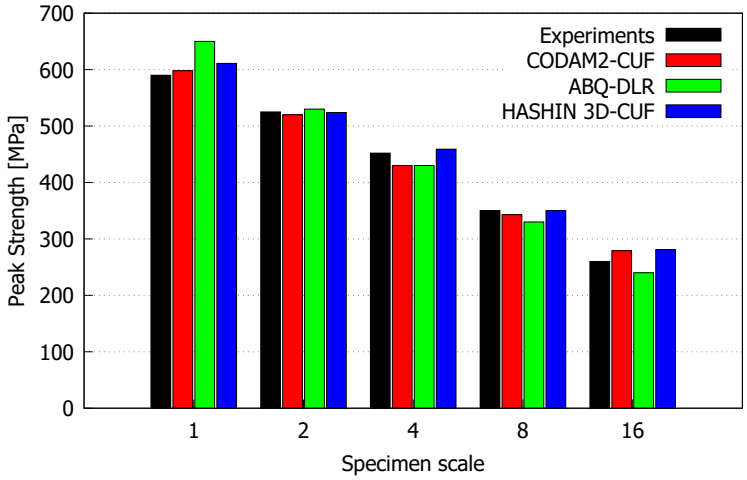

Figure 4.6: Maximum peak stress for various specimen scales using different models

[134] obtained via Digital Image Correlation (DIC). The finite element mesh consists of 392 Q9 elements as in [33], with expansion order along the thickness varying from linear (LE1) to cubic (LE3). Figure 4.9 presents the force–displacement response obtained using Hashin 3D, compared with CODAM2 and experimental results. Table 4.6 reports the Pin Opening Displacement (POD) at damage initiation and the first peak force, along with the percentage errors relative to experiments. As in the previous case, the influence of fiber shear ($\alpha_f = 0$ versus $\alpha_f = 1$) is shown in Fig. 4.10, indicating negligible differences. Figure 4.11 illustrates the distribution of matrix and fiber damage at peak stress. CUF was employed for both Hashin 3D and CODAM2 with 392 Q9 elements. Additional comparisons include CODAM2 with LS-DYNA and the ABQ-DLR Ladeveze damage model. The main observations are as follows:

1. The force–displacement curves in Fig. 4.9 show a discrepancy between the predicted damage initiation in the LE models and experimental results, likely due to the absence of delamination modeling.

2. Hashin 3D-CUF and CODAM2-CUF both predict damage initiation at POD = 1.142 mm (Table 4.6), producing similar curves. LE models predict higher peak forces than experiments, again attributable to the neglect of delamination. In [139], CUF models incorporating delamination achieved better agreement with experimental data. LE1 displacement fields remain similar to other numerical models in the literature, improving the match.

Table 4.5: Peak strength and percentage error relative to experimental values for different scales

Scale	Model	Peak strength (MPa)	Error (%)
1	Experiments	590	-
	CODAM2-CUF	598	1.4
	ABQ-DLR	650	10.2
	Hashin 3D-CUF	611	3.6
2	Experiments	525	-
	CODAM2-CUF	520	-0.9
	ABQ-DLR	530	0.9
	Hashin 3D-CUF	524	-0.2
4	Experiments	452	-
	CODAM2-CUF	430	-4.9
	ABQ-DLR	430	-4.9
	Hashin 3D-CUF	459	1.5
8	Experiments	350	-
	CODAM2-CUF	343	-2.0
	ABQ-DLR	330	-5.7
	Hashin 3D-CUF	350	0.0
16	Experiments	260	-
	CODAM2-CUF	279	7.3
	ABQ-DLR	240	-7.7
	Hashin 3D-CUF	281	8.1

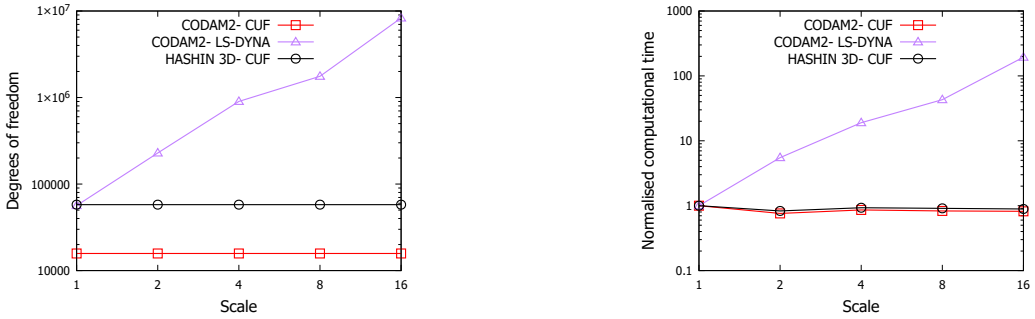

(a) Degrees of Freedom (DOF) **(b)** Normalized computational time

Figure 4.7: Comparison of DOF and computational time for different specimen scales and numerical approaches

3. Post-peak oscillations in CUF models arise from the use of fully integrated Q9 elements without numerical damping. Experimental curves are less smooth, reflecting heterogeneous fiber failure, manufacturing defects, and interactions of failure mechanisms including splitting and delamination, as noted in [140].

4. Damage distributions in Fig. 4.11 indicate that, at POD = 1.5 mm, the area near the crack initiates damage earlier for Hashin 3D than for CODAM2.

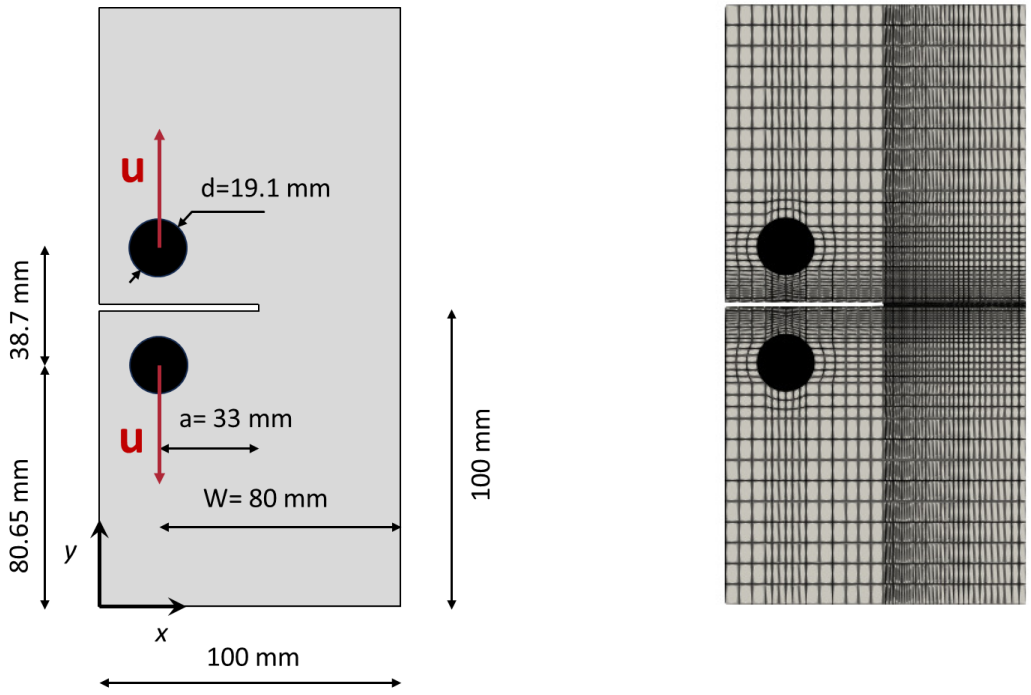

(a) Geometry **(b)** Mesh

Figure 4.8: Geometry, boundary conditions, and mesh of the OCT specimen

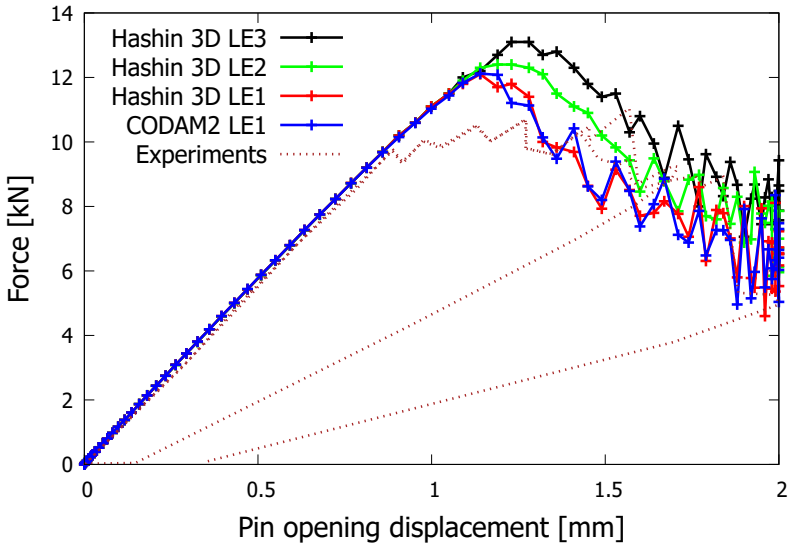

Figure 4.9: Force–displacement curves of the OCT specimen comparing Hashin 3D, CODAM2, and experimental results

Table 4.6: Comparison of POD at damage initiation and first peak force for the OCT specimen, with percentage error relative to experimental $F_{\max}$

	Hashin 3D-LE1	Hashin 3D-LE2	Hashin 3D-LE3	CODAM2-LE1	Experiments
POD (mm)	1.142	1.192	1.233	1.142	0.888
$F_{\max}$ (kN)	12.08	12.39	13.09	12.11	9.72
Error $F_{\max}$ (%)	24.3	27.5	34.7	24.6	-

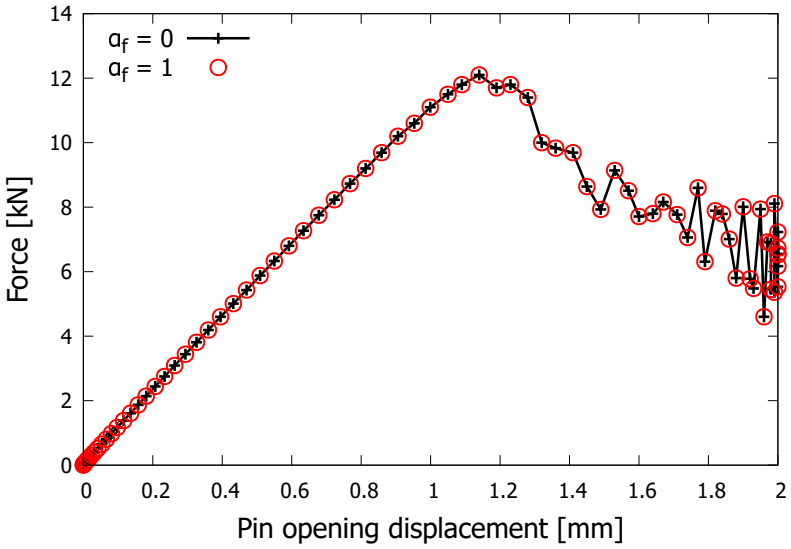

Figure 4.10: Force–displacement curves for the OCT specimen with $\alpha_f = 0$ and $\alpha_f = 1$

4.2 Compressive loading cases

4.2.1 Single element

The first compressive benchmark considers a single element of dimensions 1 mm × 1 mm. The material is IM7/8552 carbon fiber reinforced polymer (CFRP), with a ply thickness of 0.125 mm. The adopted CUF structural model employs a four-node Q4 element for in-plane discretization and a linear Lagrange expansion (LE1) along the thickness, consistent with the CODAM2-based approach in [34].
Three loading scenarios are examined: (i) uniaxial compression in the longitudinal direction with fibers oriented along the y-axis (0°); (ii) uniaxial compression in the transverse direction (90°); and (iii) uniaxial compression of a quasi-isotropic laminate with stacking sequence $[90/45/0/-45]_{2s}$. The corresponding boundary conditions and stress–strain responses are reported in Fig. 4.12. In Figures 4.12a-4.12b, the stress–strain responses obtained with Hashin 3D-CUF are compared against CODAM2-CUF based on 2D Hashin criteria [34]. For the quasi-isotropic case in Fig.4.12c, results are additionally compared with CODAM2-CUF, two LS-DYNA models, and the ABQ-DLR-UD user-defined model in Abaqus/Explicit [141]. In particular, LS-DYNA employs CODAM2 (MAT219) and the Laminate-Based Composite Model

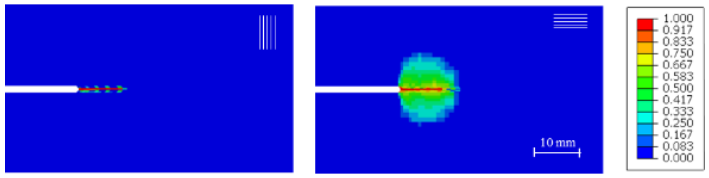

(a) Hashin 3D (CUF)

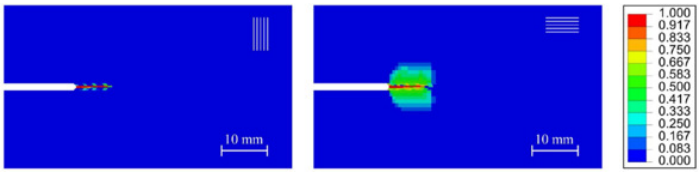

(b) CODAM2 (CUF)

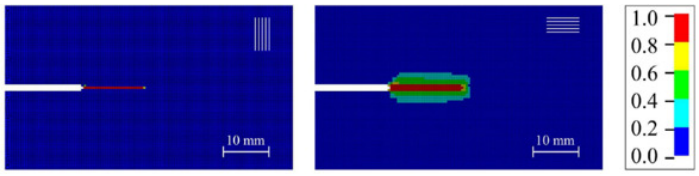

(c) CODAM2 (LS-DYNA)

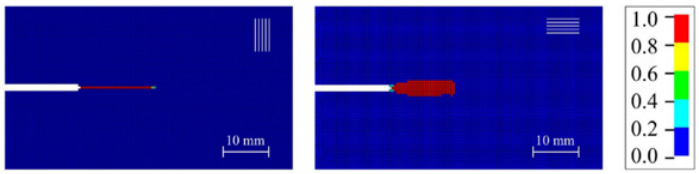

(d) ABQ-DLR

Figure 4.11: Damage distribution at POD = 1.5 mm: matrix damage in 90° ply (right) and fiber damage in 0° ply (left)

(MAT81), while ABQ-DLR-UD implements Ladeveze's coupled transverse–shear damage formulation [142].
The results can be summarized as follows:

1. The peak stresses predicted by the proposed model closely match the material strengths: 1690 MPa for fiber and 250 MPa for matrix. These values are also consistent with CODAM2-CUF predictions. The fracture energy, computed as the area under the stress–strain curve, is 80 $\mathrm{kJ/m^2}$ in the longitudinal direction and 4.2 $\mathrm{kJ/m^2}$ in the transverse direction, in good agreement with CODAM2.

2. For the quasi-isotropic configuration, the peak stress aligns well with CODAM2 and ABQ-DLR-UD predictions. In contrast, MAT81 underestimates the peak by about 30%. This discrepancy is likely due to its homogenized laminate representation, which neglects separate fiber and matrix failure mechanisms. In CUF, each ply is modeled explicitly with one Q4 element and one LE1 expansion, whereas MAT81 employs a stacked 3D shell approach with simplified laminate behavior.

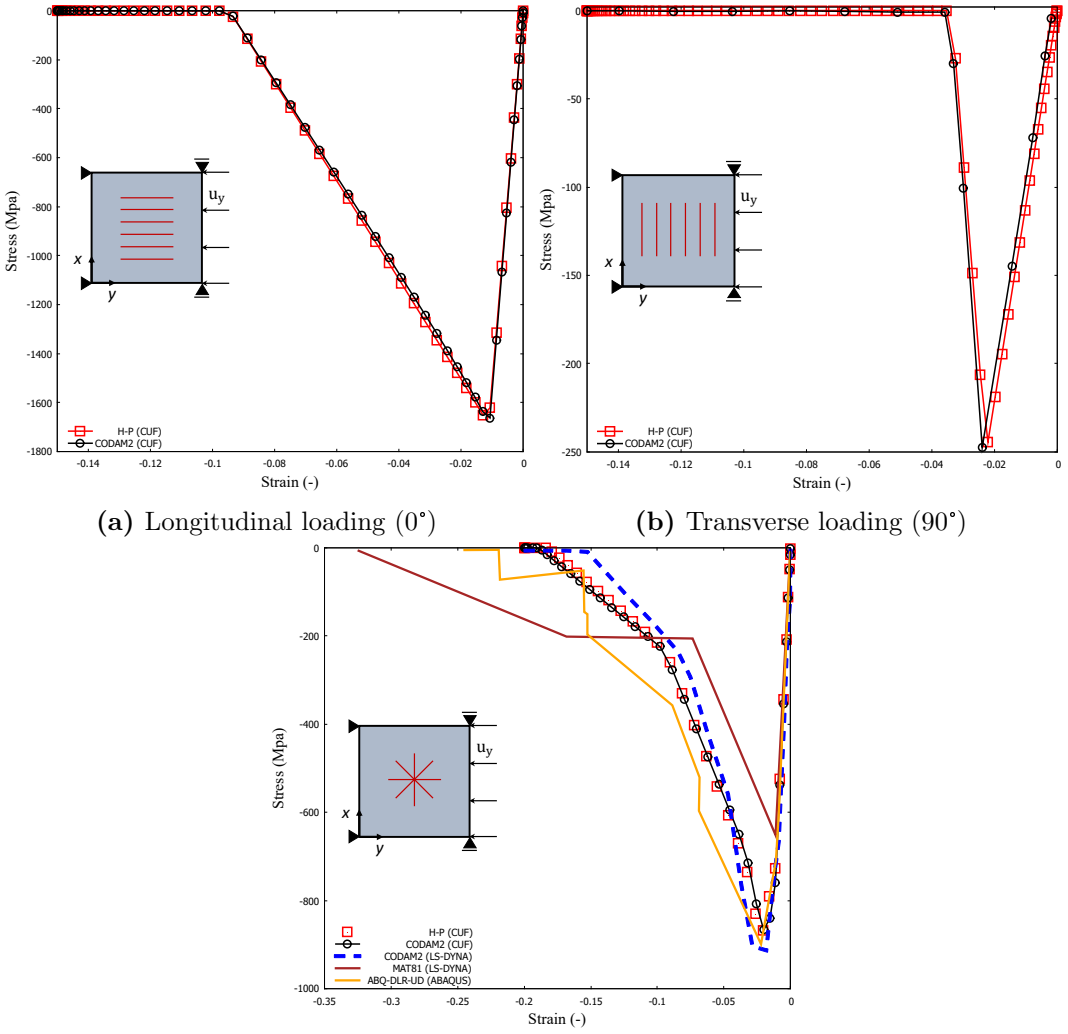

(a) Longitudinal loading (0°)

(b) Transverse loading (90°)

(c) Quasi-isotropic laminate

Figure 4.12: Stress–strain response of the single element under uniaxial compression

4.2.2 Compact compression test

The second benchmark concerns a compact compression (CC) test performed on a quasi-isotropic $[90/45/0/-45]_{4s}$ laminate. The geometry, loading configuration, and finite element mesh are shown in Fig. 4.13. This numerical case was originally introduced in [140], where quasi-static fracture experiments were conducted. Later, in [141], the same configuration was analyzed using CODAM2 and MAT81 damage models in LS-DYNA. The present CUF simulations adopt the same geometry and in-plane discretization, consisting of 191 quadratic nine-node (Q9) elements [34]. Three kinematic expansions are used through the thickness, from linear (LE1) to cubic (LE3). The number of elements and corresponding degrees of freedom (DOF) for all models is reported in Table 4.7. Figure 4.14 presents the force–POD curves. CUF models exhibit a linear softening post-peak response, with different expansions (LE1–LE3)

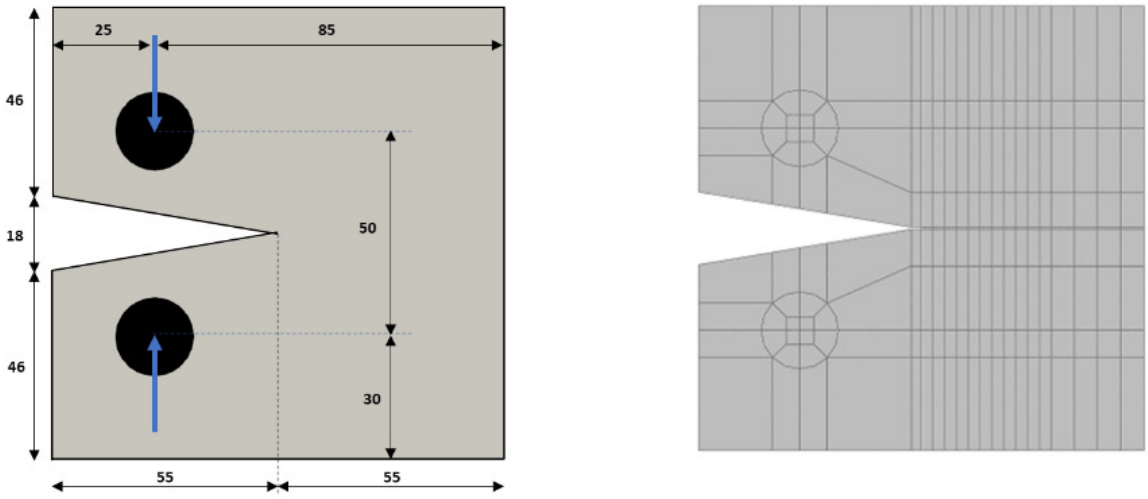

Figure 4.13: Geometry and in-plane discretization of the CC specimen; dimensions in mm. The CUF finite element mesh contains 191 Q9 elements.

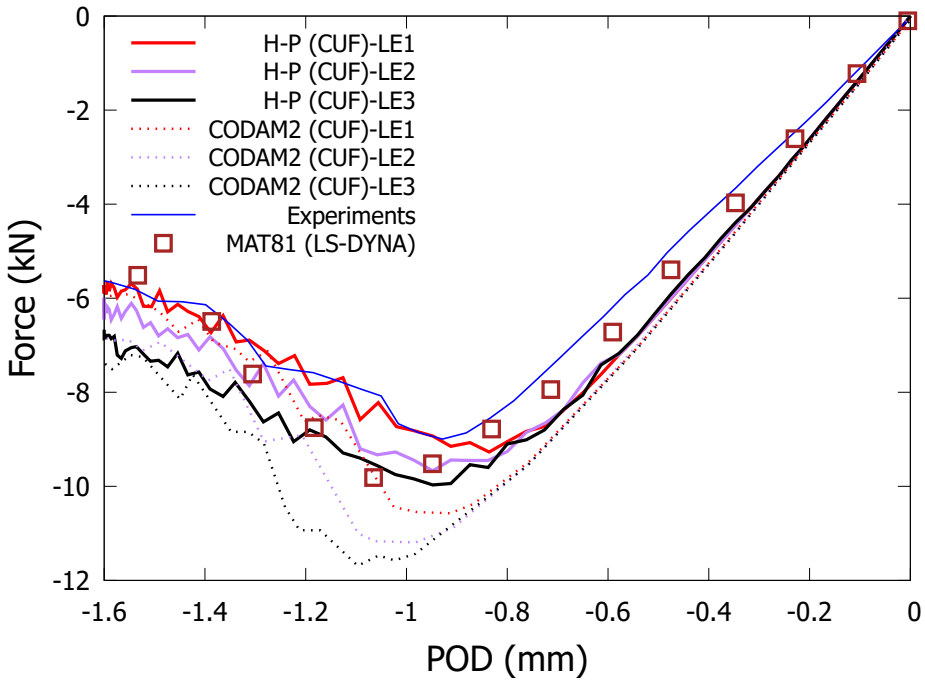

Figure 4.14: Force–POD curves for the CC test

through the thickness. For reference, the experimental curve and the MAT81 model from LS-DYNA are also included. Table 4.8 summarizes the peak force and corresponding POD values, along with the percentage errors relative to experiments.
The damage progression for the H-P LE1 model is shown in Fig. 4.15. The vertical markers in Fig. 4.15a indicate the three POD values analyzed: -0.687, -0.836, and -0.985 mm. Corresponding fiber and matrix damage distributions are illustrated in Fig. 4.15b. The main findings can be summarized as follows:

Model	Elements	DOF
CUF 191Q9-LE1	191 Q9 elements in-plane, 1 LE1 per ply	82467
CUF 191Q9-LE2	191 Q9 elements in-plane, 1 LE2 per ply	162435
CUF 191Q9-LE3	191 Q9 elements in-plane, 1 LE3 per ply	242403
MAT81 (LS-DYNA)	4848 shell elements	N/A

Table 4.7: Number of elements and DOF in the FE models for the CC test

Approach	Peak Force (kN)	Error (%)	POD at Peak Force (mm)	Error (%)
Experiments	-9.092	–	0.932	–
MAT81 (LS-DYNA)	-9.912	9.0	1.005	7.8
H-P (CUF)-LE1	-9.267	1.49	0.836	-10.3
H-P (CUF)-LE2	-9.668	6.3	0.948	1.87
H-P (CUF)-LE3	-9.965	9.6	0.948	1.87
CODAM2 (CUF)-LE1	-10.671	17.4	0.887	-4.8
CODAM2 (CUF)-LE2	-11.283	24.1	0.962	3.2
CODAM2 (CUF)-LE3	-11.808	29.9	1.074	15.2

Table 4.8: Comparison of peak forces and POD values at peak force for different models of the CC test

1. The H-P model reproduces the experimental force–POD curves with good accuracy.

2. In the case of linear softening, H-P provides a better match with experiments than CODAM2, with percentage errors for both peak force and POD below 10%. Higher-order expansions (LE2 and LE3) improve the POD prediction but introduce oscillations in peak force convergence. Since this is an in-plane problem, LE1 is sufficient to obtain accurate results. Higher-order kinematics are expected to become more relevant in problems dominated by interlaminar effects such as delamination.

3. Small differences in the slope of the linear branch are likely related to difficulties in replicating the exact experimental boundary conditions.

4. Oscillations in the CUF post-peak response may be attributed to the absence of numerical damping.

5. Compared to MAT81 in LS-DYNA, the H-P CUF approach shows lower percentage errors. This is due to the layer-wise description of each ply in CUF, while MAT81 relies on a homogenized laminate representation.

4.2.3 Open-hole compression test

The third case study investigates an open-hole specimen with a quasi-isotropic layup of $[45/90/\text{-}45/0]_{4s}$ subjected to compressive loading. This benchmark is based on the numerical work presented in [34] and compared with the experimental results

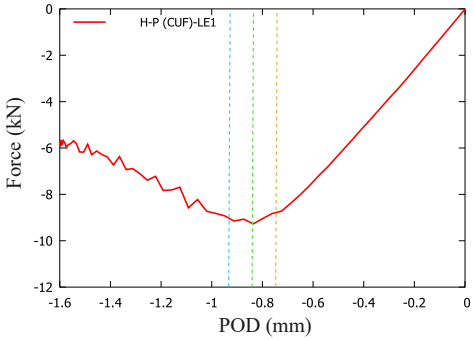

(a) Force–POD curve

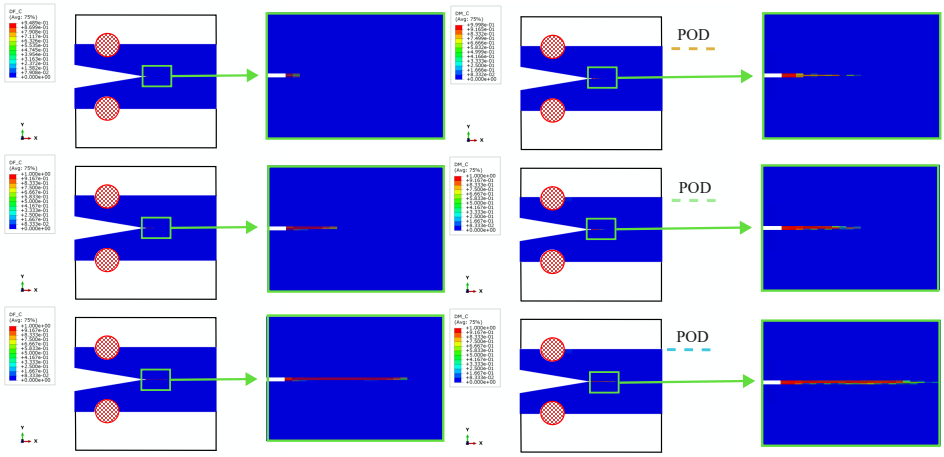

(b) Damage distributions

Figure 4.15: Damage progression in the H-P LE1 model at POD values of −0.687, −0.836, and −0.985 mm; fiber damage on the left, matrix damage on the right.

reported by Lee and Soutis [143]. The geometry and boundary conditions of the specimen are illustrated in Fig. 4.16, where the specimen dimensions W and L vary according to the adopted scale, as listed in Table 4.9. The discretization details, including the number of elements and degrees of freedom (DOF) for each model, are summarized in Table 4.10.

	L (mm)	W (mm)	d (mm)
Scale 1	32	32	6.35
Scale 2	64	64	12.70
Scale 3	128	128	25.40

Table 4.9: Dimensions of the open-hole specimen at different scales.

The first set of results concerns Scale 1. Various CUF models are analyzed, using 48, 72, and 96 Q9 elements, combined with LE1, LE2, and LE3 expansion functions. The post-peak behavior exhibits linear softening, as illustrated in Fig. 4.17. Peak loads are compared with experimental data [143], with numerical simulations based on the MAT18 damage model in LS-DYNA [34], and with Abaqus simulations using Hashin

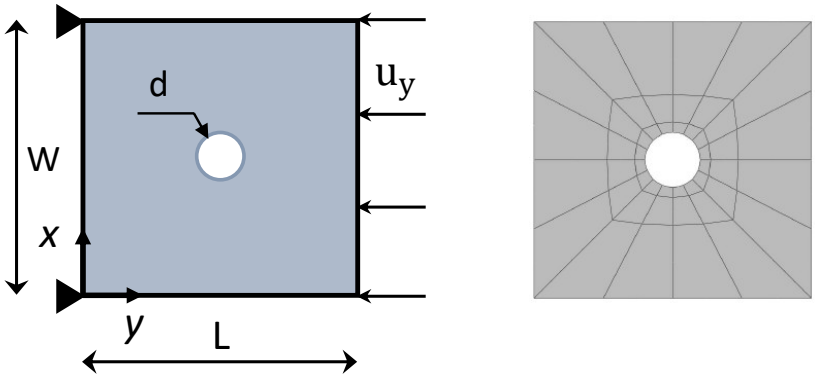

Figure 4.16: Geometry and boundary conditions of the open-hole specimen under compressive loading. The FE mesh consists of 48 Q9 elements.

Model	Elements	DOF
	Scale 1	
CUF 48Q9-LE1	48 Q9 elements in-plane and 1 LE1 per ply	22176
CUF 48Q9-LE2	48 Q9 elements in-plane and 1 LE2 per ply	43680
CUF 48Q9-LE3	48 Q9 elements in-plane and 1 LE3 per ply	65184
CUF 72Q9-LE1	72 Q9 elements in-plane and 1 LE1 per ply	33264
CUF 96Q9-LE1	96 Q9 elements in-plane and 1 LE1 per ply	44352
MAT18 (LS-DYNA)	1202 shell elements	N/A
	Scale 2	
CUF 128Q9-LE1	128 Q9 elements in-plane and 1 LE1 per ply	57024
	Scale 3	
CUF 256Q9-LE1	256 Q9 elements in-plane and 1 LE1 per ply	114048

Table 4.10: Number of elements and DOF for the different open-hole compression test models.

2D criteria with shell elements. Figure 4.18 extends the comparison to CUF models with linear-brittle post-peak softening and the H-P damage model, benchmarking them against experiments, MAT18 in LS-DYNA, and CODAM2-CUF predictions. Damage evolution obtained with the H-P CUF model (96 Q9 mesh, LE1) is reported in Fig. 4.19, at displacements of -0.24 mm, -0.29 mm, and -0.31 mm. The final analysis considers the peak failure strength across all three scales. For this set, CUF simulations employ LE1 with a linear-brittle (Br-50) post-peak softening. As shown in Fig. 4.20, the H-P CUF predictions are compared with CODAM2 CUF models (Br-30), experimental data, and MAT18 damage models in LS-DYNA [34]. The key findings are:

1. Linear softening tends to overestimate peak stresses by approximately 20% compared to experimental values. The H-P approach improves accuracy compared to CODAM2 and Hashin 2D (Abaqus), reducing the peak load discrepancy by about 25%.

2. A mesh with 48 Q9 elements is sufficient to achieve converged results.

3. Linear-brittle softening models provide more accurate peak strength predictions.

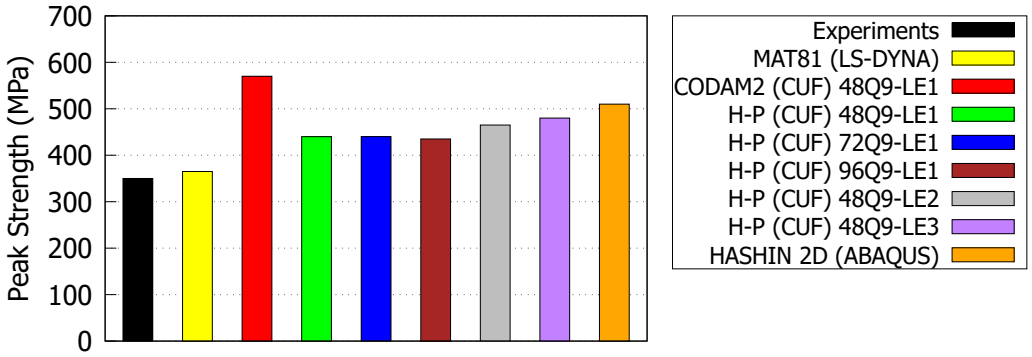

Figure 4.17: Comparison of peak strength values of the $[45/90/\text{-}45/0]_{4s}$ open-hole compression specimen (Scale 1) using different damage models, experiments, and CUF models with linear softening.

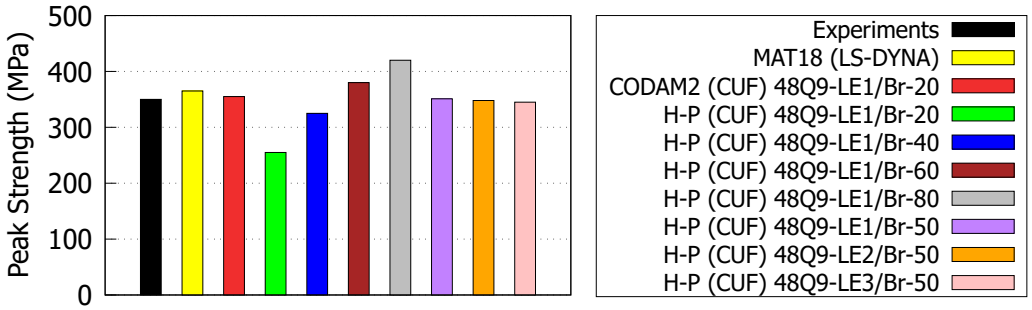

Figure 4.18: Comparison of peak strength values of the $[45/90/\text{-}45/0]_{4s}$ open-hole compression specimen (Scale 1) with different post-peak softening laws.

Variations in expansion functions (LE1–LE3) have a negligible effect on the compressive peak load.

4. The H-P CUF approach with Br-50 post-peak softening offers better agreement

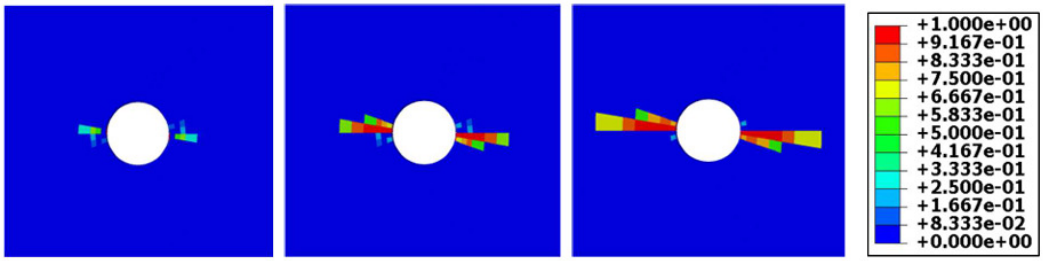

(a) Fiber damage evolution.

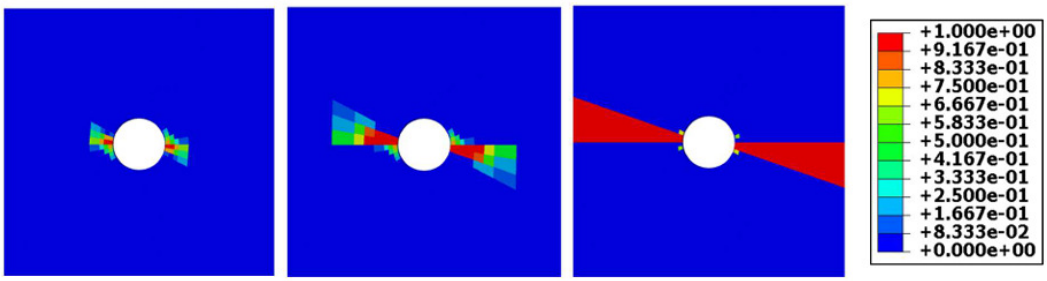

(b) Matrix damage evolution.

Figure 4.19: Damage progression of the $[45/90/\text{-}45/0]_{4s}$ open-hole compression specimen (Scale 1) at displacements of -0.24 mm, -0.29 mm, and -0.31 mm for: a) fiber and b) matrix.

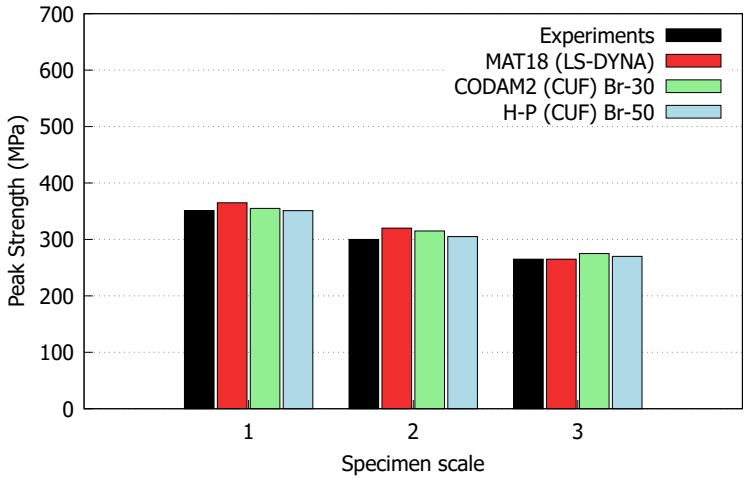

Figure 4.20: Comparison of peak strength values of the $[45/90/\text{-}45/0]_{4s}$ open-hole compression test across three scales.

with experiments than MAT18 in LS-DYNA, while requiring fewer computational resources. The CUF model uses 48 Q9 elements in-plane, compared to 1202 elements in the MAT18 model.

4.3 Discussion

This chapter has investigated the progressive damage behavior of composite laminates under both tensile and compressive loading conditions, by combining higher-order two-dimensional structural theories with advanced failure criteria within the framework of CUF. The adoption of a layer-wise modeling strategy has allowed for an explicit description of ply-level kinematics, thereby ensuring that the essential mechanisms governing damage initiation and propagation could be represented with accuracy. In this context, Hashin's three-dimensional failure criteria were employed for tensile simulations, while the combined Hashin–Puck formulation was used for compressive scenarios. The aim was not only to capture the distinct failure mechanisms associated with fiber- and matrix-dominated responses but also to provide a modeling approach capable of balancing accuracy and computational efficiency when compared with full 3D analyses.

For tensile cases, the numerical studies have confirmed the ability of higher-order CUF-based theories to reproduce experimental responses with a reduced computational burden. For the over-height compact tension test, higher-order CUF models reproduce the experimental response with a strongly reduced computational cost. Compared to 3D FEM analyses, CUF formulations require over one order of magnitude fewer degrees of freedom and up to two orders of magnitude lower computational time. By avoiding the need for excessive mesh refinement, these models provide accurate predictions of stress–strain curves and ultimate strengths even when the specimen size increases. This result is particularly significant because it highlights the intrinsic capability of higher-order CUF formulations to capture the dominant kinematic and stress gradients through the thickness without relying on local mesh refinement. In conventional three-dimensional finite element models, an increase in specimen size typically requires a proportional refinement of the mesh in order to accurately resolve stress concentrations and damage localization, leading to a rapid growth in the number of degrees of freedom. The comparison with CODAM2 has revealed that Hashin's 3D formulation tends to predict more extended damage areas, a feature consistent with the physical expectations of matrix cracking and fiber-matrix interactions. These results underline the capacity of the proposed approach to provide reliable simulations while preserving efficiency, especially when compared with traditional 3D solid models.

In the compressive regime, the integration of Hashin and Puck criteria has demonstrated clear improvements over CODAM2, particularly in capturing the strength and damage progression of open-hole specimens. The sensitivity analyses on softening laws have shown that the choice of linear-brittle behavior is crucial to accurately predict peak strengths, while compact compression could be effectively described even with linear softening when coupled with the H-P approach. Furthermore, the comparison between LW CUF models and ESL formulations has highlighted the necessity of retaining ply-level kinematics. ESL approximations resulted in less accurate predictions,

whereas the layer-wise framework provided robust and consistent results across different configurations.
Taken together, these findings confirm that the proposed CUF-based modeling strategy, enriched with refined structural theories and advanced failure criteria, constitutes a powerful and efficient tool for the progressive damage analysis of composite laminates. It offers predictive capabilities that are comparable with those of more computationally demanding 3D approaches, while maintaining the flexibility to incorporate different failure mechanisms and constitutive laws.
It should be noted that the present framework is primarily aimed at the prediction of intralaminar damage mechanisms, namely fiber- and matrix-dominated failure within the plies. Although the layer-wise CUF formulation enables an accurate reconstruction of three-dimensional stress fields, including interlaminar stress components, delamination is not explicitly modeled in the present implementation. Therefore, the reconstructed 3D stress state can be regarded as an indicator of potential interlaminar critical regions, but not as a direct prediction of delamination onset and propagation. This aspect may partly explain some discrepancies with experimental results in benchmark cases where failure is governed by the interaction of intralaminar damage, splitting, and interlaminar separation. In this regard, it is worth noting that CUF-based models have already been coupled in the literature with cohesive interface elements for the explicit simulation of delamination, for instance in low-velocity impact analyses of composite laminates [139, 144].
It is important to note that the progressive damage analyses presented here were performed under quasi-static loading conditions, allowing for a detailed investigation of the initiation and growth of damage mechanisms in composites. However, real engineering structures are rarely exposed to purely static conditions; instead, they typically operate under variable-amplitude and random cyclic loads that gradually degrade material properties and lead to fatigue failure. For this reason, the models and findings obtained in the quasi-static regime constitute a fundamental basis for the subsequent transition to fatigue analyses in the frequency domain, where the cumulative effects of random loading on structural integrity are investigated.

Part II

Fatigue life estimation in frequency domain

Chapter 5

Fatigue analysis in frequency domain

This chapter presents the theoretical and methodological foundations required to evaluate the fatigue life of structures subjected to stochastic loading within the frequency-domain framework. The first part introduces the fundamentals of random response analysis, including the description of excitation and structural response through Power Spectral Densities (PSD) and associated statistical quantities such as root mean square (RMS) values. Building on these concepts, the Dirlik method, one of the most widely adopted spectral fatigue approaches, is presented for estimating stress-range probability distributions directly from PSD data. The chapter then discusses fatigue estimation and crack propagation models traditionally employed for metallic components, providing a reference framework for spectral fatigue assessment. Finally, these concepts are extended to composite materials, where an equivalent stress PSD based on the Tsai–Hill failure criterion is adopted to predict fatigue life within the CUF high-order structural modeling environment.

5.1 Random response

When a linear structural system with n degrees of freedom is subjected to random excitations, its behaviour in the time domain can be described by the classical equation of motion:

$$\mathbf{M}\ddot{\mathbf{q}} + \mathbf{C}\dot{\mathbf{q}} + \mathbf{K}\mathbf{q} = \mathbf{f}(t), \tag{5.1}$$

where $\ddot{\mathbf{q}}$, $\dot{\mathbf{q}}$, and $\mathbf{q}$ denote the vectors of generalized accelerations, velocities, and displacements, respectively. The term $\mathbf{f}(t)$ represents a vector of time-dependent random forces acting on selected DOF, while $\mathbf{M}$, $\mathbf{C}$, and $\mathbf{K}$ are the mass, damping, and stiffness matrices of the structure.
To analyse the system in the frequency domain, the Fourier transform is applied to

Eq. (5.1), leading to the algebraic equilibrium equation [145]:

$$\mathbf{q}_k(\omega) = \left[-\omega^2\mathbf{M} + i\omega\mathbf{C} + \mathbf{K}\right]^{-1} \mathbf{F}_k^*, \quad i = \sqrt{-1}, \tag{5.2}$$

where $\mathbf{q}_k(\omega)$ represents the displacement vector in the frequency domain associated with the k-th non-zero term of the generalized force vector, and $\mathbf{F}_k^*$ is a unit vector isolating the corresponding DOF. Owing to the linearity of the system, independent frequency-response analyses can be performed for each active force component and superimposed afterward to reconstruct the total structural response.

5.1.1 Modal reduction for random response analysis

A more efficient approach for computing the random response of large finite element models is based on modal reduction. As originally described by Dey [146], the method avoids repeated matrix inversion in the frequency domain by projecting the equations of motion onto the undamped eigenmodes of the structure.
The starting point is the free vibration eigen-problem:

$$(\mathbf{K} - \omega_j^2\mathbf{M})\mathbf{x}_j = \mathbf{0}, \tag{5.3}$$

where ω_j and $\mathbf{x}_j$ denote the j-th natural frequency and its corresponding mode shape. Collecting n_m eigenvectors into the modal matrix $\mathbf{X} = [\mathbf{x}_1\ \mathbf{x}_2\ \ldots\ \mathbf{x}_{n_m}]$, the physical displacements are expressed in terms of the modal coordinates $\boldsymbol{\eta}(t)$ as

$$\mathbf{q}(t) = \mathbf{X}\,\boldsymbol{\eta}(t). \tag{5.4}$$

Exploiting the orthogonality of the eigenvectors with respect to mass and stiffness [146], one obtains:

$$\mathbf{X}^T\mathbf{M}\mathbf{X} = \boldsymbol{\Lambda}, \qquad \mathbf{X}^T\mathbf{K}\mathbf{X} = \mathbf{I}, \tag{5.5}$$

where $\boldsymbol{\Lambda} = \mathrm{diag}(\Lambda_1, \ldots, \Lambda_{n_m})$ contains the modal masses. Assuming proportional structural damping, the modal damping matrix becomes diagonal:

$$\mathbf{X}^T\mathbf{C}\mathbf{X} = \mathbf{D}. \tag{5.6}$$

Premultiplying the transformed equation of motion by $\mathbf{X}^T$ leads to a set of uncoupled single–degree-of-freedom equations:

$$\Lambda_j\ddot{\eta}_j(t) + D_j\dot{\eta}_j(t) + \eta_j(t) = \mathbf{x}_j^T\mathbf{f}(t). \tag{5.7}$$

Applying the Fourier transform to Eq. (5.7), the j-th modal transfer function is obtained as:

$$H_j(\omega) = \frac{1}{1 - (\omega/\omega_j)^2 + i\,g_j}, \tag{5.8}$$

where g_j is the structural damping factor of the mode. This expression corresponds to the modal admittance derived in [146], but is presented here explicitly in terms of the transfer function $H_j(\omega)$. Using the modal transfer functions, the full transfer function matrix of the structure can be reconstructed without any matrix inversion:

$$\mathbf{H}(\omega) = \mathbf{X}\,\mathrm{diag}(H_1(\omega), \ldots, H_{n_m}(\omega))\,\mathbf{X}^T. \tag{5.9}$$

Power Spectral Density of Random Processes

Random excitation and structural response in the frequency domain are described using the Power Spectral Density, a key statistical descriptor of stationary stochastic processes. The PSD quantifies how the power of a random signal is distributed over frequency, enabling the characterization of both broadband and narrowband excitations without requiring explicit time-domain simulations. For a real-valued, zero-mean random process $x(t)$, the one-sided PSD is defined as [147]:

$$\mathbf{G}_{xx}(f) = \lim_{T\to\infty}\left(\frac{1}{T} \mid \mathbf{X}_T(f)|^2\right), \tag{5.10}$$

where $X_T(f)$ is the Fourier transform of the truncated signal $x_T(t)$ observed over the finite interval $[-T/2, T/2]$. This formulation is fully consistent with the classical definitions employed in random vibration theory, where ergodicity and stationarity allow the PSD to be computed as the ensemble-average spectral energy density.
The PSD plays a central role in frequency-domain analysis because it bypasses the need to directly simulate time histories of random excitation. Instead, once the PSD of the load is known or estimated from measurements, the corresponding PSD of the structural response may be determined analytically through the transfer function of the system. For a linear time-invariant system subjected to a stochastic input with PSD $G_{in}(f)$, the output PSD is given by

$$\mathbf{G}_{out}(f) = \bar{\mathbf{H}}(f)\,\mathbf{G}_{in}(f)\,\mathbf{H}^T(f), \tag{5.11}$$

where $H(f)$ is the frequency-response transfer function that maps input to output in the frequency domain, while $\bar{H}(f)$ and $H^T(f)$ denote the complex conjugate and transpose, respectively. This expression follows directly from the linearity of the system and the definition of cross-power spectral densities, and it represents how each frequency component of the input is filtered by the dynamic properties of the structure.
In the context of finite element analysis, the PSD of displacement G_{u_i} and stress components G_{σ_j} at a given point of the structure can be expressed as

$$\mathbf{G}_{u_i}(f) = \bar{\mathbf{H}}_{u_i}(f)\,\mathbf{G}_F(f)\,\mathbf{H}^T_{u_i}(f), \qquad i = 1,2,3, \tag{5.12}$$

$$\mathbf{G}_{\sigma_j}(f) = \bar{\mathbf{H}}_{\sigma_j}(f)\,\mathbf{G}_F(f)\,\mathbf{H}^T_{\sigma_j}(f), \qquad j = 1,\ldots,6, \tag{5.13}$$

where $G_F(f)$ is the PSD of the applied generalized forces. These relations allow one to estimate RMS values of displacements, stresses, and strains directly from the PSDs by integrating over frequency, a step that is fundamental for fatigue analysis in the frequency domain.
In practical FE implementations, the transfer function matrix $\mathbf{H}(f)$ is constructed by performing as many frequency response analyses as the number of non-zero entries n_{nz} in the generalized load vector $\mathbf{F}$. For the k-th non-zero force component, the frequency response is assembled into the matrix

$$\mathbf{H}_{(q_k)}(f) = \left[q_{(k_1)}\ q_{(k_2)}\ \ldots\ q_{(k_L)}\right], \qquad k = 1,\ldots,n_{nz}, \qquad L = 1,\ldots,f_s, \tag{5.14}$$

where each column vector $q_{(k_l)}$ represents the structural response at the L-th frequency step, obtained by solving the frequency-domain equation of motion (Eq.(5.2)). Once the full transfer matrix is known, the propagation of input PSD through the structure follows directly from Eq. (5.11).
A comprehensive and rigorous introduction to the theory of random vibration, spectral representations, and statistical properties of structural response can be found in [54], which provides detailed discussions on ergodicity, spectral moments, filtering of random processes, and numerical considerations for PSD-based analysis.

5.1.2 Force spectral density within the CUF framework

Within the Carrera Unified Formulation (CUF), stochastic external loads are introduced through the spectral representation of the generalized force vector. Starting from the Principle of Virtual Displacements, the virtual variation of the internal strain energy δL_{int} is equated to the virtual work of the external loads δL_{ext},

$$\delta L_{\text{int}} = \delta L_{\text{ext}}. \tag{5.15}$$

The external work includes contributions from volume, surface, and point forces. In the presence of stochastic surface pressures, which are typical of aeroelastic and acoustic loading conditions, the generalized nodal force vector associated with a pressure field F_A acting on a surface A can be expressed as in [126]

$$\mathbf{F}(t) = \int_A \mathbf{F}_s(x,\xi)\,\mathbf{N}_j(y)\,F_A(x,y,t)\,\mathrm{d}A, \tag{5.16}$$

$\mathbf{F}(t)$ denotes the vector of generalized nodal forces associated with the stochastic pressure field. The quantities $\mathbf{F}_\tau(x,\xi)$ and $\mathbf{N}_j(y)$ represent the CUF through-the-thickness expansion functions and the finite element shape functions along the beam axis, respectively, and are written in boldface since they collect vector-valued contributions

associated with the displacement degrees of freedom. ξ denotes the local coordinates of the finite element. Conversely, $F_A(x, y, t)$ denotes the stochastic pressure field acting on the surface A and is treated as a scalar quantity. As a result, the surface integral yields a vector of generalized forces consistent with the finite element discretization adopted in the present work.
The statistical characterization of the generalized forces is obtained by defining the correlation matrix between two time instants t_1 and t_2 as [126]

$$\mathbf{R}_F(t_1, t_2) = \int_A \mathbf{F}_s(x_1, \xi)\mathbf{N}_j(y_1) \int_A \mathbf{F}_s(x_2, \xi)\mathbf{N}_j(y_2)\, \mathbb{E}[F_A(x_1, y_1, t_1)\, F_A(x_2, y_2, t_2)]\, \mathrm{d}A_1\, \mathrm{d}A_2. \tag{5.17}$$

Assuming the pressure field to be a stationary stochastic process, the correlation function depends only on the time lag $\tau = t_2 - t_1$. By taking the Fourier transform of the correlation matrix, the cross-spectral density matrix of the generalized forces is obtained as [126]

$$\mathbf{S}_F(\omega) = \int_A \mathbf{F}_s(x, \xi)\mathbf{N}_j(y) \int_A \mathbf{F}_s(x, \xi)\mathbf{N}_j(y)\, \mathbf{S}_P(\omega)\, \mathrm{d}A_1\, \mathrm{d}A_2, \tag{5.18}$$

where $\mathbf{S}_P(\omega)$ denotes the cross-spectral density matrix of the applied pressure field. Under the assumption of spatially separable pressure spectra, the above expression can be simplified as [126]

$$\mathbf{S}_F(\omega) = \left[\int_A \mathbf{F}_s(x, \xi)\mathbf{N}_j(y)\, \mathrm{d}A\right] \mathbf{S}_P(\omega) \left[\int_A \mathbf{F}_s(x, \xi)\mathbf{N}_j(y)\, \mathrm{d}A\right]^T. \tag{5.19}$$

This formulation shows that, within the CUF framework, the stochastic excitation enters the finite element model through the force cross-spectral density matrix $\mathbf{S}_F(\omega)$, which depends on both the spectral properties of the load and the adopted kinematic expansion. Once $\mathbf{S}_F(\omega)$ is known, the displacement and stress power spectral densities are obtained by propagating the force PSD through the structural transfer function, as discussed in Section 5.1.1.

5.2 Dirlik's method

A common approach to fatigue analysis under random loading is to work in the time domain, reconstruct the stress time history, perform rainflow counting, and finally evaluate damage via Palmgren-Miner's rule. This procedure, although accurate and conceptually straightforward, becomes computationally expensive when long-duration signals and broadband random processes are involved, especially if the structural response needs to be computed repeatedly, for instance within a parametric or probabilistic framework. Frequency–domain methods leverage the statistical properties

of stationary random processes, summarised by PSD, and enable fatigue assessment without explicitly reconstructing the complete time history of the stress.
Within this class of approaches, Dirlik's method is among the most widely adopted, as it provides a closed-form expression for the probability density function (PDF) of the stress directly in terms of the spectral moments of the PSD. It was originally proposed by Turan Dirlik in his doctoral thesis [52], where a systematic Monte Carlo study was carried out to establish a link between rainflow counting and the PSD of stationary and ergodic Gaussian processes. In the present work, Dirlik's method is adopted in combination with the PSD of the stress $G_\sigma(f)$ computed via frequency-response analysis of the structural model.

Spectral characterization of the stress

Let $G_\sigma(f)$ denote the one–sided PSD of the stress history at the point of interest. Once the random response analysis has been performed in the frequency domain, the stress PSD is known and the corresponding spectral moments m_i can be evaluated as

$$m_i = \int_0^\infty f^i \, G_\sigma(f) \, \mathrm{d}f, \tag{5.20}$$

where $i = 0,1,2,\ldots$ and m_0 coincides with the variance of the stress process. The root–mean–square (RMS) stress is therefore given by $\sqrt{m_0}$.
From the spectral moments, two key dimensionless parameters are introduced. The first is the mean frequency x_m, defined as:

$$x_m = \left(\frac{m_1}{m_0}\right)\left(\frac{m_2}{m_4}\right)^{1/2}, \tag{5.21}$$

which provides a measure of the average slope of the response spectrum. The second family of parameters is the set of bandwidth coefficients α_i, defined as

$$\alpha_i = \frac{m_i}{\sqrt{m_0 \, m_{2i}}}, \tag{5.22}$$

with particular emphasis on α_2, often referred to as the irregularity factor. In the present context, α_2 is interpreted as a measure of the spectral bandwidth: for a narrow–band process $\alpha_2 \to 1$, whereas for a wide–band process α_2 approaches zero. m_{2i} denotes the spectral moment of order $2i$ of the response power spectral density, defined according to the general expression of spectral moments. Finally, the characteristic frequency of stress occurrences, which will be used to estimate the number of cycles per unit time, is written as

$$\mathrm{freq} = \sqrt{\frac{m_4}{m_2}}. \tag{5.23}$$

This expression represents the expected rate of local peaks of the process and plays an analogous role to the mean up-crossing frequency in classical random vibration theory.

5.2.1 Dirlik Probability Density Function

As documented in [53], Dirlik analysed a total of 70 PSDs of various shapes as rectangular, smooth, narrow-band, wide-band, and bimodal. These spectra were normalised to have the same RMS value and peak rate, while the irregularity factor α_2 was varied systematically. For each PSD, synthetic stress time histories were generated through inverse FFT. From these time histories, rainflow ranges and simple peak-valley ranges were extracted, producing the empirical distributions shown in [53].
A key observation emerged from this simulation campaign: the rainflow range distribution cannot be represented by a single classical probability distribution. Instead, it was consistently found to be well approximated by a weighted mixture of:

- an exponential distribution (dominating small amplitudes),
- a Rayleigh-like distribution with variable scale parameter (intermediate amplitudes),
- a standard Rayleigh distribution (large amplitudes).

To calibrate the analytical form of the rainflow range distribution, Dirlik generated synthetic stress time histories from prescribed PSDs using the inverse FFT. Each realization consisted of 1024 points, and the procedure was repeated 20 times to obtain a sufficiently long simulated record (20480 points), a limitation imposed by the computing resources available at the time [53]. The concatenated signal was then processed in the time domain to extract peaks and troughs, from which fatigue cycles were identified using both rainflow counting and simple peak–valley range counting. Based on these counted cycles, empirical probability distributions of simple ranges and rainflow ranges were constructed as shown in Fig. 5.1. The empirical evidence provided the foundation for Dirlik's three-term mixed probability density function. Rainflow ranges r are normalised according to:

$$Z = \frac{r}{2\sqrt{m_0}}.$$

The Dirlik probability density function can be expressed as:

$$p_{DK}(Z) = \frac{1}{2\sqrt{m_0}} \left[D_1 \frac{1}{Q} e^{-Z/Q} + D_2 \frac{Z}{R^2} e^{-\frac{Z^2}{2R^2}} + D_3 Z e^{-\frac{Z^2}{2}} \right]. \tag{5.24}$$

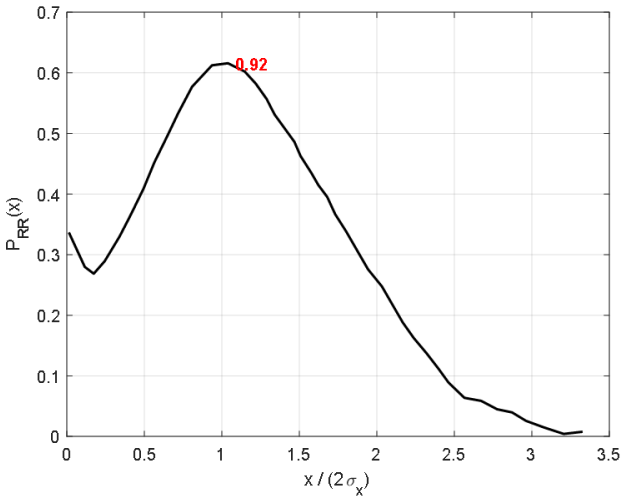

Figure 5.1: Example of empirical probability distribution with $\alpha_2 = 0.92$ as described in [53].

The coefficients depend on α_2 and x_m through:

$$D_1 = \frac{2\,(x_m - \alpha_2^2)}{1 + \alpha_2^2}, \tag{5.25}$$

$$D_2 = \frac{1 - \alpha_2 - D_1 + D_1^2}{1 - \alpha_2}, \tag{5.26}$$

$$D_3 = 1 - D_1 - D_2, \tag{5.27}$$

and the scale parameters:

$$R = \sqrt{\frac{\alpha_2 - x_m - D_2^2}{1 - \alpha_2 - D_1 + D_2^2}}, \tag{5.28}$$

$$Q = 1.25\,\frac{\alpha_2 - D_3 - D_2 R}{D_1}. \tag{5.29}$$

These relationships were obtained by least-squares fitting of the analytical PDF to the empirical rainflow distributions. Their dependence on four spectral moments explains the method's superior accuracy in broadband cases.

5.2.2 Fatigue Damage using Dirlik distribution

The main challenge in linking PSD information to fatigue is that fatigue damage depends on the distribution of stress ranges extracted by a counting algorithm, typically the rainflow method. For a narrow–band process, the peaks of a Gaussian signal follow a Rayleigh distribution and each peak is associated with a negative minimum of comparable magnitude. The stress ranges are therefore related in a simple way to

the peak distribution. In this case, classical narrow–band approximations are available and the fatigue damage can be expressed in closed-form in terms of the spectral moments.
However, for wide–band processes this assumption is no longer valid: the stress history contains many interrupted cycles, nested loops and non-symmetric peaks and valleys. The rainflow range distribution differs significantly from the distribution of ordinary ranges, particularly in the tails of the distribution where high–amplitude cycles reside. As shown in Dirlik's thesis, the rainflow method tends to count more very small ranges, fewer medium–amplitude ranges, and more large ranges than ordinary range counting for the same PSD. This behaviour is critical for fatigue, since large ranges dominate the damage accumulation.
Because of the complexity of the rainflow algorithm, deriving an exact analytical expression for the rainflow range distribution directly from the PSD is extremely challenging. Dirlik therefore adopted a Monte Carlo approach: given a prescribed PSD, synthetic random stress histories were generated using inverse Fourier transformation, rainflow counting was applied, and the empirical histogram of ranges was determined. This extensive simulation campaign was repeated for many spectra, with varying irregularity factor and mean frequency, to cover a representative set of loading conditions. In the notation used in this thesis, following Ref. [54], r corresponds to the stress σ in the fatigue evaluation and normalised by the RMS value according to

$$Z = \frac{\sigma}{\sqrt{m_0}}. \tag{5.30}$$

For an S–N curve expressed as $N = Kr^{-b}$, the rainflow damage per unit time can be computed using the continuous Miner rule:

$$D = \nu_{rfc} \int_0^\infty \frac{p_{DK}(r)}{Kr^{-b}}\, dr, \tag{5.31}$$

where $\nu_{rfc} = \frac{1}{2\pi}\sqrt{\frac{m_2}{m_0}}$ is the rainflow cycle rate.

Substituting the Dirlik PDF yields the closed-form expression :

$$D_{DK} = \frac{\nu_{rfc} T}{K} (\sqrt{m_0})^b \left[D_1 Q^b \, \Gamma(1+b) + (\sqrt{2})^b \, \Gamma\left(1 + \frac{b}{2}\right) \left(D_2 |R|^b + D_3\right) \right]. \tag{5.32}$$

where T is the duration of the considered loading history, K and b are the material fatigue parameters of the S-N curve $N(r) = K\, r^{-b}$, and $\Gamma(\cdot)$ is the Euler Gamma function. This expression is one of the major practical advantages of the Dirlik method: it enables fatigue assessment directly from the PSD without generating a time history or performing cycle counting.

5.3 Fatigue for metallic structures

Fatigue in metallic structures subjected to random vibration is often governed by the propagation of cracks under cyclic loading. While the frequency–domain approach provides an efficient means of estimating an equivalent stress range from the stress PSD, crack growth prediction requires the corresponding Stress Intensity Factor (SIF) range, which represents the driving force for fatigue crack extension. In this section, the theoretical framework linking the Dirlik stress distribution, the equivalent stress range, the geometry factor, and Paris' crack growth law is presented.

5.3.1 Crack growth modelling and Stress Intensity Factor

Once the PDF $p(\sigma)$ is known, the expected number of stress cycles with amplitude in the interval $[\sigma_k, \sigma_k + \Delta\sigma]$ over a time interval Δt can be expressed as

$$n_k = p(\sigma_k)\,\Delta\sigma\,\mathrm{freq}\,\Delta t, \tag{5.33}$$

where freq is given by Eq. (5.23). The quantity n_k plays the same role as the cycle counts obtained from rainflow analysis.
For fatigue crack growth or S–N based life prediction, it is often convenient to define an equivalent stress range $\Delta\sigma_{\mathrm{eq}}$ that, when applied for an equivalent number of cycles, produces the same damage as the full random spectrum. Assuming a power–law damage relationship, as in Paris' law for crack growth, and denoting by m the exponent of the law, the equivalent stress range can be written as:

$$\Delta\sigma_{\mathrm{eq}} = \left(\frac{\sum_k \sigma_k^m n_k}{\sum_k n_k} \right)^{1/m} . \tag{5.34}$$

This expression is discussed in Ref. [148] and provides the link between the Dirlik distribution and the crack growth model adopted in the present work. Once $\Delta\sigma_{\mathrm{eq}}$ is known for a given crack size, it can be used to compute an equivalent stress intensity factor range and, hence, the crack increment according to Paris' law for the metallic structures.
For metallic materials, the crack propagation in the Paris region is commonly expressed as

$$\frac{da}{dN} = C_0\,(\Delta K)^m\,, \tag{5.35}$$

where C_0 and m are material constants. Thus, conversion from $\Delta\sigma_{\mathrm{eq}}$ to an equivalent SIF range $\Delta K_{\mathrm{SIF,eq}}$ is required for crack-growth analysis.

5.3.2 Geometry factors for metallic structures

The Stress Intensity Factor (SIF) for a cracked body subjected to a nominal stress range $\Delta\sigma$ can be written in the general form

$$\Delta K = F(a)\,\Delta\sigma\sqrt{\pi a}, \tag{5.36}$$

where a is the crack size and $F(a)$ is a dimensionless geometry factor that accounts for finite geometry, crack shape and loading mode. Equation (5.36) originates from linear elastic fracture mechanics (LEFM) [149, 150] and applies to many standard configurations, including

- edge cracks under tension: $F \approx 1.12$;
- through cracks in finite plates: $F(a) = \sec\left(\frac{\pi a}{W}\right)$, where W is half-width;
- central cracks in infinite plates: $F = 1$.

For more complex geometries, such as surface cracks, embedded flaws, stiffened panels or interacting cracks, geometry factors can be obtained from handbooks (e.g., [151, 152]) or through numerical techniques such as finite element analysis and weight functions [153]. Replacing the stress range with its equivalent value $\Delta\sigma_{\text{eq}}$, the equivalent SIF range becomes

$$\Delta K_{\text{SIF,eq}} = F(a)\,\Delta\sigma_{\text{eq}}\,\sqrt{\pi a}. \tag{5.37}$$

This expression forms the link between frequency–domain stress analysis and crack-growth mechanics.

5.3.3 Equivalent SIF range and crack-growth prediction

A random stress history containing N_T cycles can be interpreted as a sequence of blocks, each with its associated SIF range ΔK_j. The cumulative crack extension is

$$\Delta a_T = \sum_{j=1}^{N_T} C_0\,(\Delta K_j)^m\,. \tag{5.38}$$

An equivalent SIF range $\Delta K_{\text{SIF,eq}}$ is defined such that it produces the same Δa_T when applied uniformly for N_T cycles:

$$\Delta K_{\text{SIF,eq}} = \left(\frac{1}{N_T}\sum_{j=1}^{N_T}(\Delta K_j)^m\right)^{1/m}. \tag{5.39}$$

Substituting the geometry factor relation, one obtains a compact expression for

the average crack growth rate:

$$\left(\frac{da}{dN}\right)_{\text{eq}} = C_0 \left(\Delta K_{\text{SIF,eq}}\right)^m . \tag{5.40}$$

This sequence completes the theoretical framework adopted in the present work, linking the frequency–domain stress response to fatigue crack growth. Starting from the stress power spectral density, the associated spectral moments are first computed and used to define the stress–range probability density function through the Dirlik formulation. The resulting distribution provides the equivalent cycle counts n_k, which are employed to evaluate an equivalent stress range $\Delta\sigma_{\text{eq}}$. This quantity is then converted into an equivalent stress intensity factor range $\Delta K_{\text{SIF,eq}}$ by means of the geometry correction factor $F(a)$. Finally, fatigue crack propagation is predicted by integrating the Paris law expressed in terms of da/dN.

5.3.4 Damage indices

In metallic components subjected to fatigue, crack initiation and propagation are accompanied by progressive changes in the structural dynamic response. As the crack grows, local stiffness is reduced and the global dynamic characteristics, as natural frequencies, modal damping and frequency response functions (FRFs), are modified accordingly. Vibration-based methods (VBMs) exploit this phenomenon by monitoring variations in the FRFs of the structure over time [154, 155]. In the context of fatigue analysis in the frequency domain, and in particular when crack propagation is evaluated through an equivalent-stress framework or Paris/Walker-type laws, DI-based monitoring offers a complementary perspective: while the frequency-domain fatigue model predicts the crack growth rate theoretically, the DI captures the actual structural degradation experimentally. This duality enables combined prediction–verification strategies suitable for real-time structural health monitoring.

FRF-based damage indices

A first family of DI was introduced by Monaco et al. [156] following extensive experimental campaigns on metallic beams and frame-like structures. Their formulation is based solely on the comparison between the magnitudes of the FRFs measured in the healthy condition, FI_i, and those measured after the onset or progression of damage, FD_i. Two scalar indices were proposed:

$$\text{DI}_1 = \frac{\displaystyle\sum_{i=1}^{n} |FI_i - FD_i|}{\displaystyle\sum_{i=1}^{n} |FI_i|}, \tag{5.41}$$

$$\mathrm{DI}_2 = \frac{1}{n}\sum_{i=1}^{n}\frac{|FI_i - FD_i|}{|FI_i|}, \tag{5.42}$$

where n is the number of spectral lines within the selected frequency band.
Both indices are zero when the two FRFs coincide and increase monotonically with the severity of the structural alteration. Monaco et al. [156] additionally introduced the concept of a *repetitiveness index*, allowing the establishment of an experimental threshold that distinguishes true structural modifications from noise-induced variations. Their results demonstrated sensitivity to very small stiffness changes, including early-stage cracks.

Damage index based on percentage FRF deviation

A second widely used DI was proposed by Mickens et al. [157] during the development of vibration-based SHM procedures for aircraft metallic joints. For each frequency f, the discrepancy between healthy and damaged FRFs is described by the percentage deviation:

$$y(f) = \left|\frac{H^h(f) - H^d(f)}{H^h(f)}\right|, \tag{5.43}$$

and the global damage index is the average deviation over the frequency range $[f_L, f_U]$:

$$D = \frac{\Delta f}{f_U - f_L}\sum_{i=1}^{N} y(f_i), \tag{5.44}$$

with Δf being the frequency resolution. This indicator has proven effective in detecting small reductions in local stiffness, such as rivet loosening or crack initiation, especially at higher frequencies where the FRF is more sensitive to local damage.

Damage indices and fatigue crack growth

More recently, Marques et al. [148] integrated DI-based monitoring into a fatigue-life estimation framework for metallic structures under random loading. In their study on aluminium beams with edge cracks, the two Monaco indices and Mickens' indicator were evaluated after repeated excitation under random base acceleration. The measured DIs showed the following behaviours:

- a clear *monotonic increase* as the crack propagates;
- an approximately *linear evolution* of DI_1 with respect to time;
- a nearly *log-linear trend* in the case of DI_2;

- excellent correlation with the crack lengths predicted via frequency-domain fatigue methods.

These properties demonstrate that DI-based monitoring can track stiffness degradation throughout the fatigue process, even when cracks remain small and difficult to detect visually. In this way, the DI becomes a diagnostic parameter that complements the theoretical crack-growth computation obtained from the equivalent stress intensity factor range $\Delta K_{\mathrm{SIF,eq}}$.

Role of damage indices in metallic fatigue assessment

Within the present thesis, damage indices serve two major purposes:

1. **Detection**: they provide early identification of deviations from the healthy structural condition, enabling the detection of crack initiation or stiffness loss before critical growth occurs.
2. **Monitoring**: they offer a quantitative measure of the progression of fatigue damage, which may be correlated with the outputs of the frequency-domain fatigue model.

Because DIs are inexpensive to compute, require only measured structural responses, without explicit knowledge of the excitation, and do not rely on explicit FE updating or modal identification, they constitute a practical tool for real-time SHM of metallic components subjected to random vibration. When combined with the previously introduced crack-growth formulation, they support a consistent methodology for fatigue assessment in the frequency domain, providing both predictive and observational insight into the structural degradation process.

5.3.5 Applicability, assumptions and limitations

The combined use of PSD-based fatigue analysis, Dirlik's distribution, and Paris' law relies on several assumptions:

- **Gaussian, stationary loading**: Dirlik's method assumes a stationary Gaussian process; strong non-Gaussian effects or non-stationarity may compromise accuracy.
- **Linear structural response**: PSD-based stress computation requires a linear, time-invariant structural model.
- **LEFM validity**: SIF formulations assume small-scale yielding and Mode I dominated behaviour.

- **Paris regime applicability**: The crack-growth law is valid only in the Paris region between threshold and unstable fracture.

Despite these limitations, the method provides an efficient and physically consistent framework for estimating fatigue life in metallic components subjected to random vibration, avoiding time-domain simulations while retaining compatibility with established fracture-mechanics models.

5.4 Fatigue for composite structures

Composite laminates subjected to random vibration loads exhibit fatigue mechanisms that are substantially different from those of metallic structures. Instead of a single dominant crack, damage in composites typically involves the interaction of several mechanisms, such as fiber breakage, matrix cracking, fiber–matrix debonding, and delamination [11]. In addition, the stress state in a laminate is generally multiaxial and the material response is strongly anisotropic. These features make it necessary to adopt fatigue damage parameters that are able to merge the contribution of all in–plane stress components into a single scalar quantity, suitable for use in frequency–domain methods.
In this context, Gao et al. [158] proposed an equivalent spectral method for the fatigue life prediction of composite laminates under random vibration loadings. The method is based on the Tsai-Hill strength criterion, extended to the frequency domain, and on the construction of a power spectral density (PSD) of an equivalent Tsai–Hill stress that acts as fatigue damage parameter. Once this equivalent stress PSD is known, the fatigue life can be estimated in analogy with the metallic case, by combining Dirlik's rainflow amplitude distribution with the material S-N curve.

5.4.1 Tsai–Hill criterion and equivalent stress in the time domain

For a unidirectional lamina under plane stress, the Tsai–Hill strength criterion can be written in the principal material directions (1,2) as

$$\frac{\sigma_1^2(t)}{X^2} - \frac{\sigma_1(t)\,\sigma_2(t)}{X^2} + \frac{\sigma_2^2(t)}{Y^2} + \frac{\tau_{12}^2(t)}{S^2} = 1, \tag{5.45}$$

where $\sigma_1(t)$ and $\sigma_2(t)$ are the normal stresses in the fiber and transverse directions, $\tau_{12}(t)$ is the in–plane shear stress, and X, Y and S are the corresponding tensile and shear strengths of the lamina [158]. It is convenient to collect the stresses in the

material axes into the vector

$$\boldsymbol{\sigma}(t) = \begin{bmatrix} \sigma_1(t) \\ \sigma_2(t) \\ \tau_{12}(t) \end{bmatrix}. \tag{5.46}$$

Then Eq. (5.45) can be rewritten as a quadratic form

$$\boldsymbol{\sigma}^{\mathrm{T}}(t)\,\mathbf{Q}\,\boldsymbol{\sigma}(t) = 1, \tag{5.47}$$

where the symmetric matrix $\mathbf{Q}$ contains the interaction coefficients of the Tsai–Hill criterion. Matching Eq. (5.45) with Eq. (5.47) gives

$$\mathbf{Q} = \begin{bmatrix} \dfrac{1}{X^2} & -\dfrac{1}{2X^2} & 0 \\ -\dfrac{1}{2X^2} & \dfrac{1}{Y^2} & 0 \\ 0 & 0 & \dfrac{1}{S^2} \end{bmatrix}. \tag{5.48}$$

Gao et al. [158] interpret the left–hand side of Eq. (5.47) as the square of a dimensionless equivalent stress, denoted here by $\bar{\sigma}_{\mathrm{eq}}(t)$:

$$\bar{\sigma}^2_{\mathrm{eq}}(t) = \boldsymbol{\sigma}^{\mathrm{T}}(t)\,\mathbf{Q}\,\boldsymbol{\sigma}(t). \tag{5.49}$$

This quantity measures the distance of the current stress state from the Tsai–Hill failure surface.
To obtain a stress-like fatigue damage parameter with the same units as the physical stresses, an equivalent strength K is introduced and the equivalent Tsai–Hill stress $\sigma_{\mathrm{eq}}(t)$ is defined by the relation

$$\sigma_{\mathrm{eq}}(t) = K\,\bar{\sigma}_{\mathrm{eq}}(t), \qquad \sigma^2_{\mathrm{eq}}(t) = K^2\,\boldsymbol{\sigma}^{\mathrm{T}}(t)\,\mathbf{Q}\,\boldsymbol{\sigma}(t). \tag{5.50}$$

The equivalent strength K is chosen such that the contributions of longitudinal, transverse and shear stress components to fatigue damage are properly balanced. In particular, Gao defines K as in [158]:

$$\frac{1}{K^2} = \frac{1}{X^2} + \frac{1}{Y^2} + \frac{1}{S^2}, \tag{5.51}$$

which reflects the assumption that, under random vibration, all failure modes (fiber, matrix, shear) are statistically possible and must be considered in the damage parameter.

5.4.2 Equivalent stress PSD in the frequency domain

Under stationary random loading, the stresses in the laminate are modelled as zero–mean Gaussian processes. The stochastic properties of the vector $\boldsymbol{\sigma}(t)$ are described by the PSD matrix $\mathbf{G}_\sigma(\omega)$, whose entries are the auto– and cross–PSDs of the stress components:

$$\mathbf{G}_\sigma(\omega) = \begin{bmatrix} G_1(\omega) & G_{1,2}(\omega) & G_{1,12}(\omega) \\ G_{2,1}(\omega) & G_2(\omega) & G_{2,12}(\omega) \\ G_{12,1}(\omega) & G_{12,2}(\omega) & G_{12}(\omega) \end{bmatrix}, \tag{5.52}$$

where G_1, G_2 and G_{12} are, respectively, the auto–PSDs of σ_1, σ_2 and τ_{12}, and $G_{i,j}$ are the corresponding cross–PSDs.
Taking the expectation of Eq. (5.50) and using the definition of the PSD matrix, one obtains

$$\mathbb{E}\big[\sigma_{\text{eq}}^2(t)\big] = K^2\,\mathbb{E}\big[\boldsymbol{\sigma}^{\text{T}}(t)\,\mathbf{Q}\,\boldsymbol{\sigma}(t)\big] = K^2 \int_0^\infty \text{Trace}\{\mathbf{Q}\,\mathbf{G}_\sigma(\omega)\}\; d\omega. \tag{5.53}$$

This motivates the definition of the PSD of the equivalent stress as

$$G_{\sigma_{\text{eq}}}(\omega) = K^2\,\text{Trace}\{\mathbf{Q}\,\mathbf{G}_\sigma(\omega)\}\,, \tag{5.54}$$

the *zeroth* spectral moment of $G_{\sigma_{\text{eq}}}$ coincides with $\mathbb{E}\left[\sigma_{\text{eq}}^2(t)\right]$. Equation (5.54) shows that the equivalent–stress PSD is a weighted linear combination of the auto– and cross–PSDs of the stress components, with weights directly determined by the Tsai–Hill criterion and the equivalent strength K.
In practice, the stress components are often first computed in a global coordinate system (x, y) by finite element analysis. If $\boldsymbol{\sigma}^0(t)$ denotes the stress vector in global axes and $\mathbf{T}(\theta)$ is the standard stress transformation matrix for a ply oriented at an angle θ with respect to the x–axis, then

$$\boldsymbol{\sigma}(t) = \mathbf{T}(\theta)\,\boldsymbol{\sigma}^0(t), \tag{5.55}$$

and the corresponding PSD matrices are related by

$$\mathbf{G}_\sigma(\omega_{eq}) = \mathbf{T}(\theta)\,\mathbf{G}_{\sigma^0}(\omega)\,\mathbf{T}^{\text{T}}(\theta). \tag{5.56}$$

This allows computing $G_{\sigma_{\text{eq}}}(\omega)$ in the material axes for each ply of the laminate, starting from the global random vibration analysis.

5.4.3 Fatigue hotspots identification

The RMS value of the equivalent Tsai–Hill stress is defined as

$$\mathrm{RMS}_{\sigma_{\mathrm{eq}}} = \sqrt{\int_0^\infty G_{\sigma_{\mathrm{eq}}}(\omega)\, d\omega}. \tag{5.57}$$

Since this quantity represents the average vibration energy of the damage parameter, it is used to identify the most critical region of the structure: the fatigue hotspot is defined as the point and ply for which $\mathrm{RMS}_{\sigma_{\mathrm{eq}}}$ attains its maximum value.
Numerical simulations performed by Gao et al. for T–shaped CFRP laminates under random base excitation show that the predicted hotspots are located at the edge of the notch hole, in $-45°$ plies, in agreement with the experimental failure location [158].

5.4.4 Random-vibration fatigue life estimation

Once the equivalent–stress PSD at the fatigue hotspot is known, the corresponding rainflow amplitude probability density function $p(S)$ is obtained by means of Dirlik's method, applied to $G_{\sigma_{\mathrm{eq}}}(\omega)$. Combining $p(S)$ with the uniaxial S–N curve in the fiber direction, $N(S)$, the fatigue life under random vibration is estimated by an equivalent cycle–counting approach. Following the total life N_T is written as

$$N_T = \left[\nu \int_0^\infty \frac{p(S)}{N(S)}\, dS\right]^{-1}, \tag{5.58}$$

where ν is the expected number of stress cycles per unit time (obtained from the spectral moments of $G_{\sigma_{\mathrm{eq}}}$). The integral in Eq. (5.58) represents the expected damage per cycle in the sense of Palmgren–Miner; its reciprocal gives the number of cycles to failure.
A key feature of this approach is that only the S–N curve in the fiber direction is required: the effects of transverse and shear stresses are already embedded in the equivalent stress definition through the Tsai–Hill weights and the equivalent strength K. This significantly reduces the experimental effort needed to characterise the fatigue behaviour of the laminate.

5.4.5 Applicability, assumptions and limitations

The equivalent spectral method for composites rests on assumptions that are largely analogous to those adopted for metallic structures in the frequency domain:

- the stress processes are modelled as stationary, ergodic, zero–mean Gaussian processes;

- the structural response is linear and time–invariant in the considered vibration range;
- fatigue damage accumulation follows a linear rule (Miner) when expressed in terms of equivalent stress cycles.

In addition, the present formulation assumes that the Tsai–Hill criterion remains representative of the failure modes under fatigue, and that the fiber–direction S–N curve is sufficient to capture the overall fatigue resistance of the laminate.
Despite these limitations, the method proposed by Gao et al. [158] based on the work of Zhou et al. [66] provides a computationally efficient and theoretically consistent framework for estimating the random–vibration fatigue life of composite laminates, and it integrates naturally with the frequency–domain fatigue methodology previously developed for metallic structures in this thesis.
It should be noted that the fatigue framework developed in this thesis is not fully uniform for metallic and composite structures. For metallic components, the frequency-domain approach is coupled with linear elastic fracture mechanics, so that damage evolution is described through crack growth and the corresponding update of the structural transfer matrix. For composite laminates, by contrast, fatigue assessment is performed through an equivalent-stress formulation based on the Tsai–Hill criterion in the frequency domain. This approach enables fatigue life estimation under multiaxial stochastic loading, but it does not explicitly account for progressive stiffness degradation during cyclic loading. Therefore, the composite fatigue model should be interpreted as a life-prediction tool.

Chapter 6

Gust power spectral density and load assessment

This chapter introduces the theoretical background and computational methodology adopted for modeling atmospheric turbulence and deriving the stochastic aerodynamic loads used in the subsequent fatigue analysis. The focus is on the von Kármán gust spectrum, a widely accepted representation of atmospheric turbulence that characterises gust intensity and spatial coherence through two fundamental parameters: the root-mean-square gust velocity and the turbulence scale length. Building upon this spectral description, the procedure for generating time-domain gust signals and computing the associated unsteady aerodynamic response is detailed. After defining the von Kármán spectrum, an inverse spectral approach is employed to reconstruct a gust velocity time history, which is then propagated through Küssner's unsteady aerodynamics model to obtain the corresponding lift fluctuations. The aerodynamic loads constitute the input for the structural random-response analysis conducted in Chapter 7, where CUF-based finite element models are used to compute stress PSD and estimate fatigue life.

6.1 Atmospheric turbulence and the von Kármán gust model

The stochastic loading produced by atmospheric turbulence represents one of the primary excitation mechanisms acting on aircraft structures during flight. As discussed extensively by Hoblit [145], turbulence may be modeled as a stationary Gaussian random field whose energy is distributed across a continuum of spatial and temporal scales. Although such an assumption greatly simplifies its mathematical formulation, it remains sufficiently accurate for engineering applications provided that the turbulence spectrum adopted for load analysis reproduces flight-test measurements. The most relevant of these features include the finite correlation length of turbulent eddies, the prevalence of large-scale energy-containing motions, and the gradual spectral decay

associated with the inertial cascade.

Within this framework, the gust encountered by an aircraft travelling at speed V is typically described through its one-dimensional power spectral density (PSD), which relates the energy content of the gust velocity fluctuations to the encounter frequency f. Hoblit identifies two spectra as the principal candidates for engineering gust-load calculations: the Dryden spectrum and the von Kármán spectrum. The former is historically appealing due to its algebraic simplicity and to the existence of exact filters capable of transforming a white-noise input into a Dryden-shaped gust time history. Its longitudinal PSD is expressed as

$$PSD_D(f) = \frac{2\,\sigma^2\,L}{\pi V}\frac{1}{\left[1+\left(\frac{2\pi L f}{V}\right)^2\right]^2}, \tag{6.1}$$

where σ denotes the root-mean-square gust velocity and L represents the turbulence scale length. The parameters have the same physical meaning as in the von Kármán model. Although Eq. (6.1) provides a convenient analytical form and has been widely employed in classical gust-response analyses, Hoblit notes that the Dryden spectrum does not accurately reproduce measured atmospheric turbulence, particularly with respect to the $-5/3$ decay observed at high frequencies and to the geometry of the knee region separating the low-frequency plateau from the inertial range.
For these reasons, and because it is more solidly rooted in turbulence theory, the von Kármán spectrum is generally recognized as providing a substantially better fit to flight-measured gust data and is therefore regarded as the standard choice for design analyses. Its longitudinal PSD takes the form

$$PSD_{vk}(f) = \frac{\sigma^2 L}{\pi V}\left[1+\frac{8}{3}\left(\frac{1.339\,2\pi L f}{V}\right)^2\right]\left[1+\left(\frac{1.339\,2\pi L f}{V}\right)^2\right]^{-11/6}, \tag{6.2}$$

The comparison between these two models is plotted in Fig. 6.1.

6.1.1 Effect of the scale length L

Hoblit emphasizes that L is not merely an empirical fitting constant but a physically meaningful measure of the characteristic size of the dominant turbulent eddies. He demonstrates that L directly determines the frequency at which the PSD transitions from its low-frequency plateau to the inertial-region decay. This transition, commonly referred to as the knee of the spectrum, occurs at a frequency of order V/L and can be identified clearly from the log–log plot in Fig. 6.2. Since structural modes are typically excited most strongly when the gust spectrum contains significant energy near the natural frequencies of the aircraft, the position of this knee plays a decisive role in shaping the dynamic response and consequently the fatigue loading.

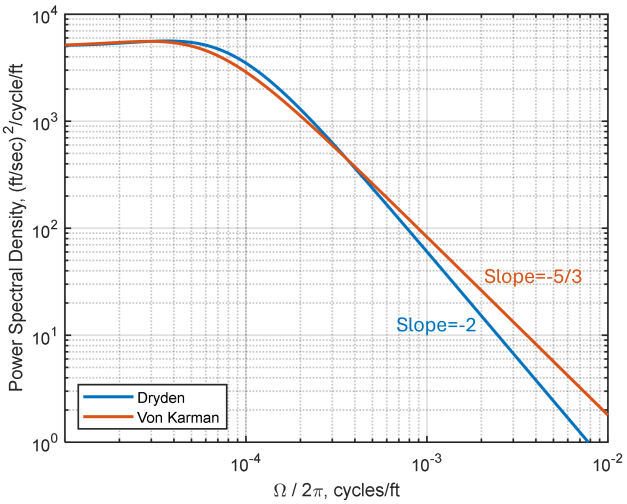

Figure 6.1: Von Kármán and Dryden gust PSD with $L = 2500$ ft, $V = 840$ fps and $\sigma = 1$ fps.

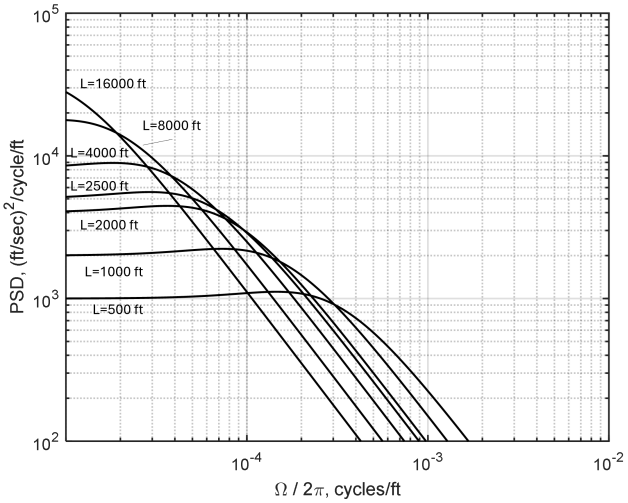

Figure 6.2: L effects on PSD of von Kármán vertical-lateral gust with $V = 840$ fps and $\sigma = 1$ fps [145].

Concerning the selection of representative values of L for engineering design, Hoblit notes that civil aircraft regulations traditionally adopt a constant value of $L = 2500\,\text{ft}$, approximately 760 m, reflecting a statistical interpretation of large-scale atmospheric turbulence. Nevertheless, he remarks that lower altitudes and specific meteorological conditions may be associated with significantly smaller values of L, especially for the vertical gust component. Such variations have a tangible effect on the shape of the spectrum: as L decreases, the knee shifts to higher frequencies, producing a gust field rich in rapid fluctuations. Conversely, large L values are associated with slowly varying gusts dominated by low-frequency content.

6.1.2 Effect of the turbulence intensity σ

In addition to the scale length L, the second parameter governing the von Kármán spectrum is the turbulence intensity σ, defined as the RMS value of the gust velocity fluctuations. Hoblit describes σ as the quantity that controls the overall energy contained in the turbulent field, and therefore the magnitude of the aerodynamic disturbances imposed on the aircraft. While L dictates how this energy is distributed across frequencies, σ determines its absolute level.
A variation in σ produces a uniform scaling of the PSD amplitude. From Eq. (6.2), it is evident that the von Kármán spectrum is proportional to σ^2 for all frequencies. Thus, a doubling of σ corresponds to a fourfold increase in the spectral density throughout the entire frequency range. Stronger atmospheric turbulence introduces larger gust velocity fluctuations, which in turn generate proportionally larger fluctuations in aerodynamic loads.
Unlike the scale length L, which modifies the shape of the spectrum by translating the location of the knee, the parameter σ does not affect the distribution of spectral energy among different frequencies. Its influence is therefore purely energetic rather than structural. Nevertheless, its role is crucial in the context of gust-response and fatigue analysis. In fact, fatigue damage accumulation is sensitive to the amplitude of stress cycles and even modest variations in σ can lead to significant changes in predicted fatigue life.
Hoblit remarks that σ exhibits substantial variability in atmospheric measurements, depending on meteorological conditions, flight altitude, and weather phenomena such as convective activity or wind shear. For design purposes, regulatory frameworks typically provide representative values or envelopes for σ, ensuring that load assessments remain conservative without becoming unrealistically severe. In continuous turbulence, the combined action of σ and L fully characterises the statistical environment in which the aircraft operates.
When interpreted within the context of structural dynamics, the distinction between the roles of L and σ becomes particularly relevant. The scale length L determines whether the excitation predominantly occurs near or far from the structural natural frequencies, whereas the intensity σ establishes the magnitude of that excitation. Together, these two parameters define the severity of the gust loading environment and serve as the primary inputs for subsequent unsteady aerodynamic modelling and structural fatigue assessment.

6.1.3 Time-domain reconstruction of von Kármán turbulence

Although the von Kármán spectrum provides a complete statistical description of the turbulence, structural analysis requires a time–domain realisation of the gust velocity history. Hoblit describes several procedures for generating such realisations;

among these, the inverse Fourier method is the most widely employed in modern applications. A synthetic gust signal is obtained by sampling the von Kármán spectrum over a sufficiently refined frequency grid, assigning random phases in accordance with the assumption of ergodicity, and enforcing the Hermitian symmetry required to produce a real-valued time series. An inverse fast Fourier transform then yields a gust velocity time history $v_g(t)$ whose statistical characteristics conform to the prescribed spectrum. The signal may subsequently be propagated through an unsteady aerodynamic model, such as Küssner's formulation, to obtain the corresponding load history acting on the wing.

6.2 Load assessment under von Kármán gust

The load assessment procedure adopted in this work follows a classical and well-established framework in aeroelasticity, widely used to relate stochastic gust models to unsteady aerodynamic loads [145]. In particular, the approach adopted here, as described by Valente et al. [159], allows the von Kármán gust velocity field to be converted into time-domain lift fluctuations acting on the wing structure. This methodology allows one to describe the stochastic gust environment through its power spectral density (PSD), to reconstruct a physically consistent gust velocity time history, and finally to evaluate the corresponding lift fluctuations using unsteady aerodynamic theory as shown in Fig. 6.3.

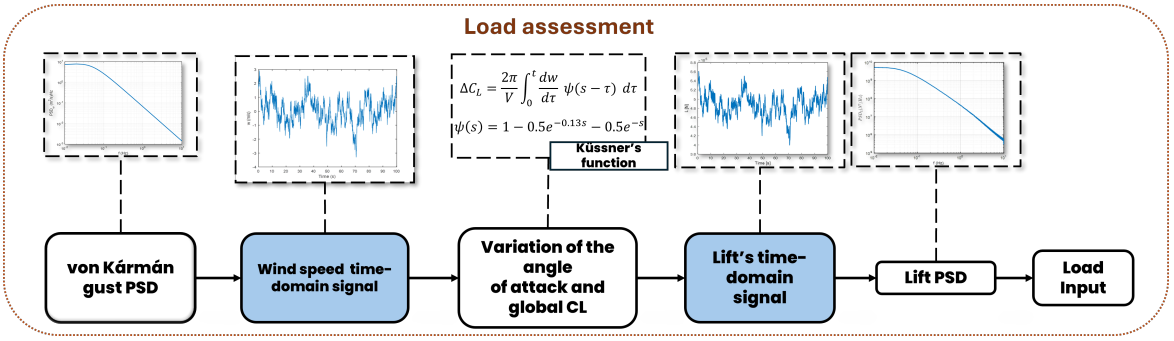

Figure 6.3: Load assessment starting from von Kármán gust speed PSD to lift PSD.

The resulting load history constitutes the excitation applied to the CUF-based structural model for the subsequent fatigue analysis.

6.2.1 Gust time-history generation

Once the atmospheric turbulence has been characterised through the von Kármán PSD (Eq. (6.2)), a time-domain realisation of the gust velocity $v_g(t)$ is required to excite the unsteady aerodynamic model. Following the approach described by [159], the gust signal is synthesized using the inverse spectral method.

Let a discrete frequency grid $\{f_k\}$ be defined over the bandwidth of interest. For each frequency, the spectral amplitude is computed as

$$A(f_k) = \sqrt{2\, PSD_{vk}(f_k)\, \Delta f},$$

and a random phase $\phi(f_k)$ uniformly distributed in $[0, 2\pi]$ is assigned. A complex-valued spectrum satisfying Hermitian symmetry is then constructed as

$$\widehat{v}_g(f_k) = A(f_k)\, e^{i\phi(f_k)}.$$

The gust velocity time history is finally obtained by means of an inverse Fast Fourier Transform:

$$v_g(t) = \mathcal{F}^{-1}\{\widehat{v}_g(f)\}.$$

The resulting signal retains the statistical and spectral characteristics of the von Kármán turbulence and is therefore suitable as aerodynamic input for the gust–response computation.

6.2.2 Küssner's function

When an aircraft penetrates a gust, the aerodynamic load does not respond instantaneously but evolves according to unsteady aerodynamic effects. To account for the effects described above, this work employs Küssner's aerodynamic lag model, which describes the incremental lift generated by an arbitrary gust profile [160].
For a vertical gust $v_g(t)$, the unsteady variation of the lift coefficient is expressed as

$$\Delta C_L(t) = \frac{2\pi}{V} \int_0^s \frac{dv_g}{d\tau}\, \psi(s-\tau)\, d\tau, \tag{6.3}$$

where V is the free-stream velocity, $s = Vt/c$ is the reduced time, and $\psi(s)$ is Küssner's indicial response function. The classical exponential approximation is adopted:

$$\psi(s) = 0.5\, \mathrm{e}^{-0.13s} - 0.5\, \mathrm{e}^{-s}. \tag{6.4}$$

Equation (6.3) naturally incorporates aerodynamic memory effects, since the instantaneous lift depends not only on the present gust velocity but on its past evolution as well. The resulting time history $\Delta C_L(t)$ represents the stochastic lift fluctuations experienced by the wing while traversing the turbulent field. By applying this formulation, it is possible to compute the time history of the lift coefficient variation induced by the gust and, consequently, to derive the corresponding lift PSD. It is worth noting that Eq. (6.3) is valid for the single airfoil, to derive the lift coefficient variation of the entire wing, the geometrical e.g., aspect ratio, and aerodynamic parameter e.g.,

Oswald factor, of the wing have to be known in advance. In this case, it is considered that same variation of the lift coefficient for both airfoil and wing, neglecting three–dimensional effects that would otherwise reduce the lift response.

Chapter 7

Numerical results of fatigue life

This chapter presents the numerical results of the fatigue analysis conducted in the frequency domain using the stress PSD obtained from CUF-based models. The first part focuses on both metallic and composite structures subjected to broadband random excitation modelled through a constant input PSD white noise. The computed stress spectra are used to evaluate crack-growth behaviour in metallic components, to compute fatigue damage indices, and to estimate fatigue life for both material classes according to established frequency-domain formulations. In the second part, the analysis is extended to more realistic loading conditions characteristic of aerodynamic environments, represented by a von Kármán gust PSD. This enables assessing the fatigue response of laminated composites under both idealized broadband excitation and physically-based turbulent spectra. Overall, the chapter aims to validate the proposed CUF-based frequency-domain framework across different materials, stochastic loading models, and fatigue metrics.

7.1 Constant PSD load cases

This subsection presents a first set of numerical cases aimed at assessing the accuracy and robustness of the proposed frequency-domain fatigue framework under simplified stochastic loading conditions. In particular, the applied excitations are defined through constant Power Spectral Density functions, which represent broadband random loads with uniform energy distribution over a prescribed frequency range. Although such loading conditions do not directly correspond to specific physical excitation mechanisms, constant PSD inputs are commonly employed as benchmark cases in frequency-domain fatigue studies. Their main advantage lies in the ability to isolate structural and material effects, such as geometry, boundary conditions, laminate stacking sequence, and stress transfer mechanisms, without the additional complexity introduced by frequency-dependent load spectra. As a result, constant PSD load

cases provide a controlled environment for method verification and comparative assessment. Two representative structures are analyzed within this framework. The first case considers a cantilever aluminum beam, selected as a reference metallic structure for validating fatigue life predictions against experimental and numerical data available in the literature. The second case involves a composite T-shaped structure, which introduces material anisotropy and laminate-dependent stress distributions, thereby offering a more challenging test for the fatigue methodology. The results discussed in this subsection focus on the identification of fatigue hot-spots, the comparison between different modeling approaches, and the influence of structural idealizations on fatigue life estimates.

7.1.1 Aluminum beam

The overall procedure adopted to evaluate the fatigue life of the structure under stationary random loading is summarised in the workflow reported in Fig. 7.1. The analysis begins with the definition of the reference test case, consisting of a cantilever beam containing two pre-existing cracks and subjected to a broadband random excitation. The structural response is computed through the two-dimensional CUF model, which provides the stress field along the beam. From this response, the corresponding stress power spectral density is obtained. The resulting PSD is subsequently used as input to Dirlik's formulation to derive the PDF of the stress amplitudes, as expressed in Eq. 5.24, which forms the basis for the ensuing fatigue-damage evaluation. Fatigue

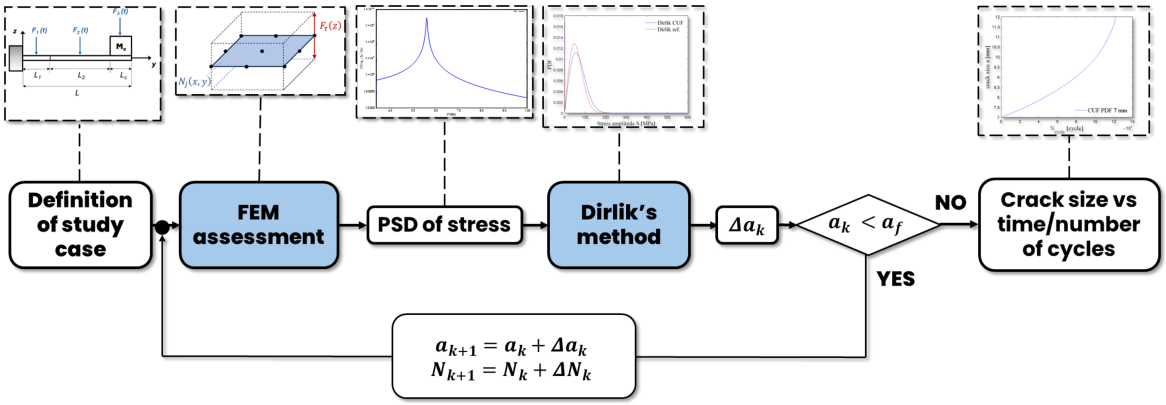

Figure 7.1: Methodological workflow for assessing the fatigue behaviour of a structure under stationary random loads.

damage is then computed iteratively by employing the average crack-growth-per-cycle law of Eq. 5.35, $C_0 = 2.71 \times 10^{-8} \frac{mm/cycle}{(MPa\sqrt{m})^m}$ and $m = 3.70$ are the material parameters of Walker's equation as described in [148]. The evolution of the crack length as a function of the accumulated number of cycles is obtained through a time-marching procedure based on the forward Euler scheme, which updates the crack size and cycle

count at each iteration according to:

$$\begin{cases} a_{k+1} = a_k + \Delta a_k, \\ N_{k+1} = N_k + \Delta N_k, \end{cases} \tag{7.1}$$

where a_k denotes the crack length at the k-th iteration, a_{k+1} its updated value, Δa_k the crack increment which is evaluated by advancing the crack tip over a non-uniform spatial discretisation, characterised by a locally refined mesh between the two cracks, N_k the cumulative number of cycles, and ΔN_k the corresponding cycle increment associated with each step.
The procedure is repeated until the crack size a_k reaches the value $a_f = 12\,\text{mm}$ which is chosen such that the corresponding stress intensity factor range remains well below the material fracture toughness, ensuring the validity of the linear elastic fracture mechanics framework adopted in the present analysis.

Test case definition

This section presents the numerical simulations carried out on the benchmark configuration experimentally investigated by Marques et al. [148]. The structure is a cantilever beam made of Al7075-T6, with a Young's modulus of 71 GPa, a Poisson's ratio of 0.33, and a mass density of 2800 kg/m^3. The beam has a thickness of 1.27 mm, and its geometry together with the clamped-free boundary condition are shown in Fig. 7.2a. The specimen contains two initial cracks of length 7 mm, each with a root radius of 0.2 mm. The total mass of the beam is 11 g, and an additional point mass of 4.5 g is attached at the free end of the beam.

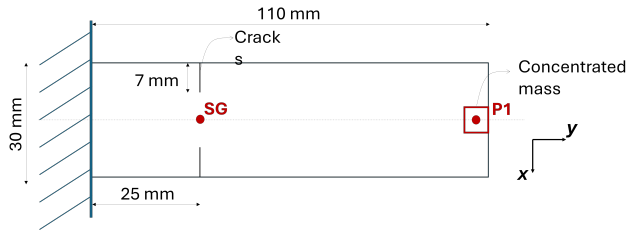

(a) Geometry

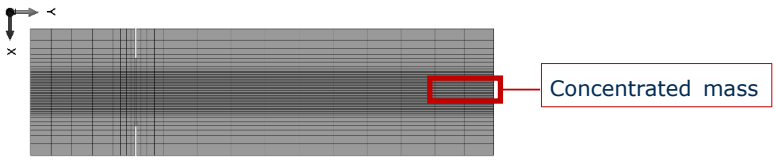

(b) Mesh

Figure 7.2: Test case definition: a) geometry and boundary condition of the aluminium clamped-free beam and b) 2D CUF mesh with 1280 Q9 elements and high-density elements modelling the added mass.

Two distinct numerical models were developed for the cantilever beam, one based on the CUF formulation and the other on FEMAP. In the CUF framework, the structure is represented by a two-dimensional model composed of 1280 bi-quadratic Q9 elements, with the thickness kinematics described by two LE1 expansions, leading to a total of $n_{DOF} = 47655$ in the initial healthy condition with 7 mm pre-cracks. The tip mass is represented through high-density elements placed at the free end, as illustrated in Fig. 7.2b. To enable a direct comparison with the experimental and numerical results reported by Marques et al. [148, 161], simulations were also performed using FEMAP/NASTRAN. In this case, a three-dimensional Hexmesh with 8168 solid elements was adopted, resulting in $n_{DOF} = 111348$.
Concerning the excitation, in the experimental setup described in [148, 161], an electrodynamic shaker ,hereafter referred to as the base, is attached to the rigid clamped region of the beam. The base is driven with a random acceleration along the z-direction in the frequency range 34–100.5 Hz, with a constant acceleration power spectral density of 0.2 g^2/Hz. The base acceleration induces inertial forces in the beam, which, due to the rigid attachment at the clamped end, generate bending stresses and promote crack propagation along the x-direction. The inertial loads can be defined in a reference frame attached to the beam, whose origin follows the motion of the base while maintaining a fixed orientation, as sketched in the upper part of Fig. 7.3. The resulting inertial load distribution along the beam is shown in Fig. 7.3b, whereas in Fig. 7.3c it is approximated by three equivalent concentrated forces. In this simplified representation, the load is condensed into three forces acting at the centres of three regions of the beam: F_1 over $0 < y < L_1$, F_2 over $L_1 < y < L$, and F_3 associated with the concentrated mass M_c. This approximation is introduced to simplify the inertial load representation while preserving the bending moment at the section $y = L_1$, which is crucial for an accurate evaluation of the stress PSD at the strain gauge (SG) location and, consequently, for the subsequent PDF estimation using Dirlik's method.

Modal analysis

The first three bending modes were calculated using different mesh densities for both FEMAP/NASTRAN (FEMAP/NX) and CUF, in order to perform a convergence study. The corresponding results are summarised in Table 7.1 and compared with the experimental measurements reported in [161]. On the basis of this study, a mesh with 1280 Q9-LE1 elements for the CUF model and 8040 HEX elements for the FEMAP/NX model was selected for the subsequent analyses, which consider different crack lengths and a frequency range from 10 to 2048 Hz.
The first three bending modes were then evaluated for different crack configurations and compared with the numerical results presented in [161], as reported in Table 7.2. For the initial configuration with 7 mm pre-cracks, the first three bending modes of the CUF model are shown in Fig. 7.5. The initial mesh consists of 1280 Q9 elements at

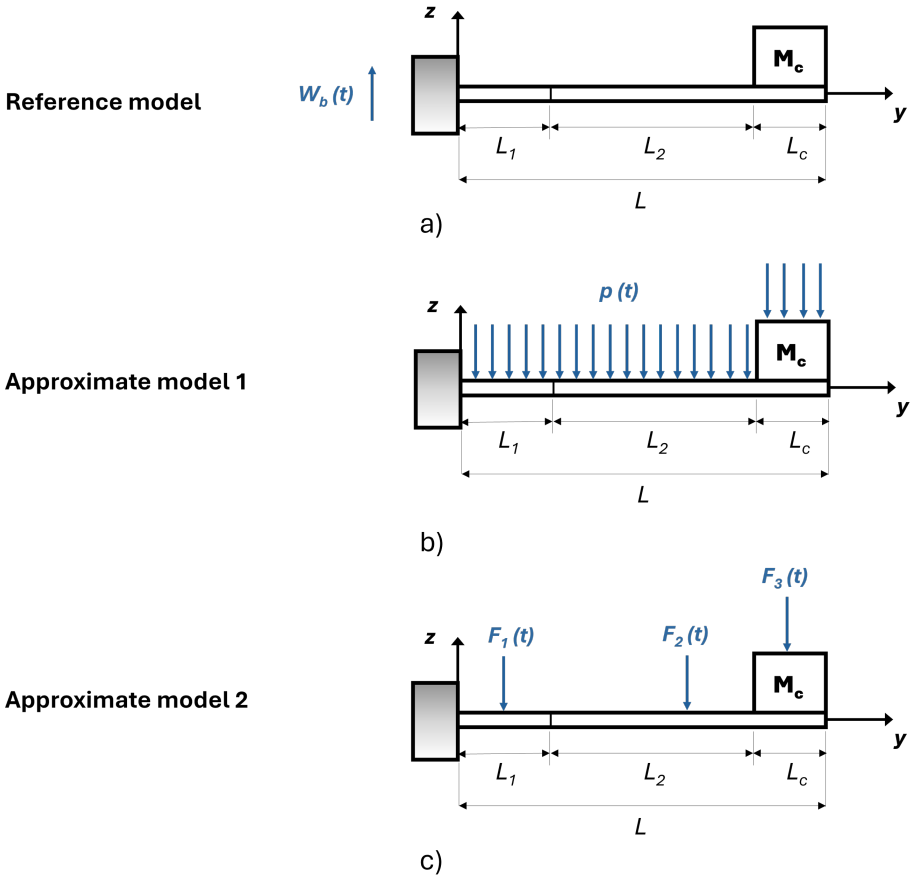

Figure 7.3: Loading condition of the clamped-free beam using three equivalent concentrated forces to reproduce the effect of the base acceleration.

$a = 7$ mm; as the crack grows, the mesh is locally modified and the number of elements gradually decreases to 1256 Q9, as summarised in Table 7.3. As already discussed in Fig. 7.1, the evolution of the crack is evaluated through an iterative procedure. At each crack increment, the mesh is regenerated to correctly capture the stress PSD.
The reduction in the number of elements with increasing crack size is not linear, since a non-uniform spatial discretisation Δa is adopted to refine the mesh between the two cracks, as shown in Fig. 7.4.
Figure 7.6 reports the evolution of the first natural frequency as a function of crack length for both CUF and FEMAP models, together with the ABAQUS and Ritz method results from [148]. The ABAQUS 3D finite element model employs 47400 solid elements.

Based on the modal analysis results, the following observations can be made:

1. For the crack size $a = 7$ mm, both the CUF and FEMAP/NX solid models provide a reasonable prediction of the first natural frequency when compared with the ABAQUS 3D reference solution (Table 7.2). The FEMAP/NX 3D model exhibits a slightly closer agreement with the reference value, while the

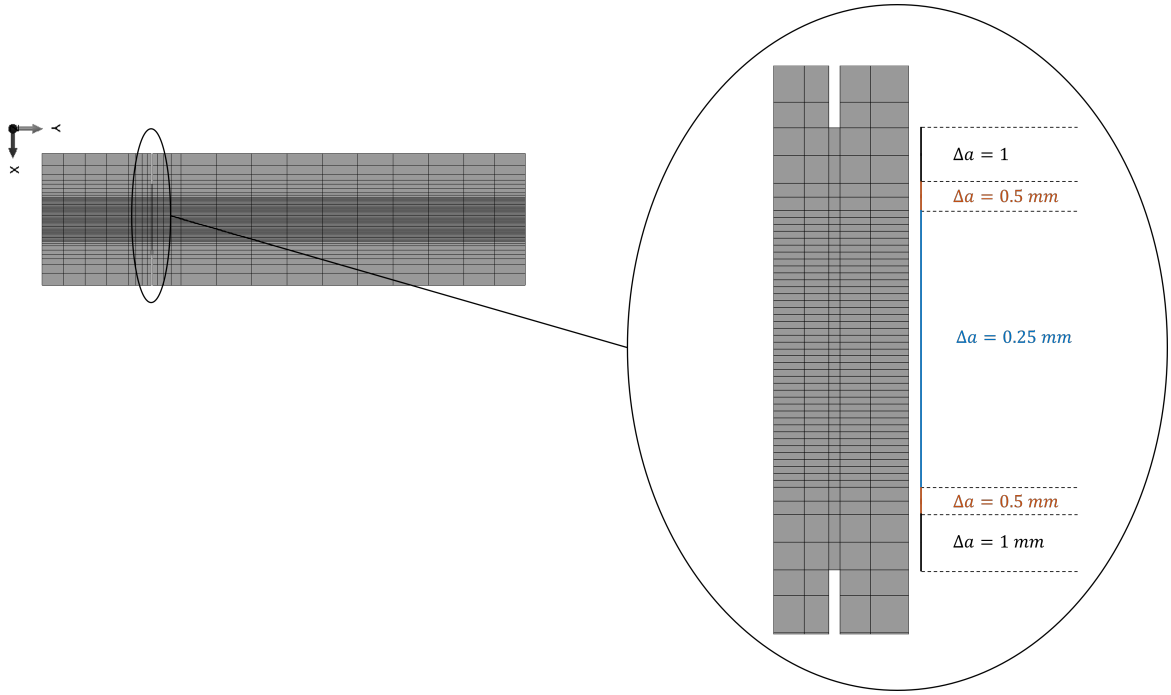

Figure 7.4: Mesh refinement in the crack region with different crack step sizes.

Table 7.1: First three natural frequencies of the intact beam for CUF and FEMAP/NX models. Comparison with ABAQUS numerical results from [148] and experimental values from [161].

Method	N_{ele}	Natural frequencies (Hz) 1^{st}	2^{nd}	3^{rd}
CUF	1472 Q9-LE1	57.2	457.3	1251.5
	1280 Q9-LE1	57.2	457.3	1252.3
	754 Q9-LE1	57.3	457.5	1253.1
	546 Q9-LE1	57.4	457.4	1253.3
FEMAP/NX	18960 HEX	58.2	465.4	1347.1
	8040 HEX	58.2	465.4	1347.2
	4748 HEX	58.3	465.5	1346.4
	2010 HEX	58.4	465.9	1348.3
ABAQUS Ref. [148]	47600 C3D20R	56.4	440.7	1258.8
Experimental Ref. [161]	-	57.4	455.1	1327.3

CUF solution shows a modest overestimation. Nevertheless, the discrepancy remains limited, and the CUF model captures the correct order of magnitude of the fundamental bending frequency. Differences between the two numerical approaches can also be attributed to the different modeling of the concentrated mass at the beam tip, which is inherently defined in a different manner in the 2D CUF formulation and in the 3D solid discretisation adopted in FEMAP.

2. Table 7.2 and Fig. 7.6 show that the first natural frequency decreases as the crack length increases, and both CUF and FEMAP models capture this behavior accurately.

Table 7.2: First three natural bending frequencies of the cracked cantilever beam. Comparison with ABAQUS 3D and Ritz method results from [161, 148].

	Natural frequencies (Hz)			
Method	$\mathbf{1}^{st}$	$\mathbf{2}^{nd}$	$\mathbf{3}^{rd}$	**Crack size a (mm)**
CUF (1280 Q9-LE1)	56.1	474.8	1383.3	7
FEMAP/NX 3D	55.6	463.2	1327.7	
CUF	55.2	473.8	1373.0	8
FEMAP/NX 3D	54.8	462.2	1317.7	
ABAQUS 3D Ref. [161]	53.1	448.6	1299.9	
Ritz method Ref. [161]	53.8	445.0	1306.5	
CUF	49.6	386.3	1311.6	12
FEMAP/NX 3D	49.5	311.5	1263.1	
ABAQUS 3D Ref. [161]	48.1	443.9	1245.0	
Ritz method Ref. [161]	49.4	444.8	1265.2	

Table 7.3: Mesh discretisation for the CUF model as the crack size increases.

Crack size (m)	**Number of Q9 elements**
7	1280
8	1278
9	1276
10	1272
11	1264
12	1256

3. For all crack configurations, the CUF model exhibits a difference lower than 4% with respect to both reference solutions (ABAQUS and Ritz method) for the first natural frequency.

4. The FEMAP 3D model shows slightly better agreement with the reference values but at the cost of a much larger number of degrees of freedom due to the solid discretisation. In contrast, the CUF model achieves comparable accuracy with a significantly reduced computational effort.

Random response analysis

Starting from the modal properties, the random dynamic response analysis is carried out following the loading configuration depicted in Fig. 7.3. Experimental investigations in [148] reported a modal damping ratio of 0.30% for the first bending mode;

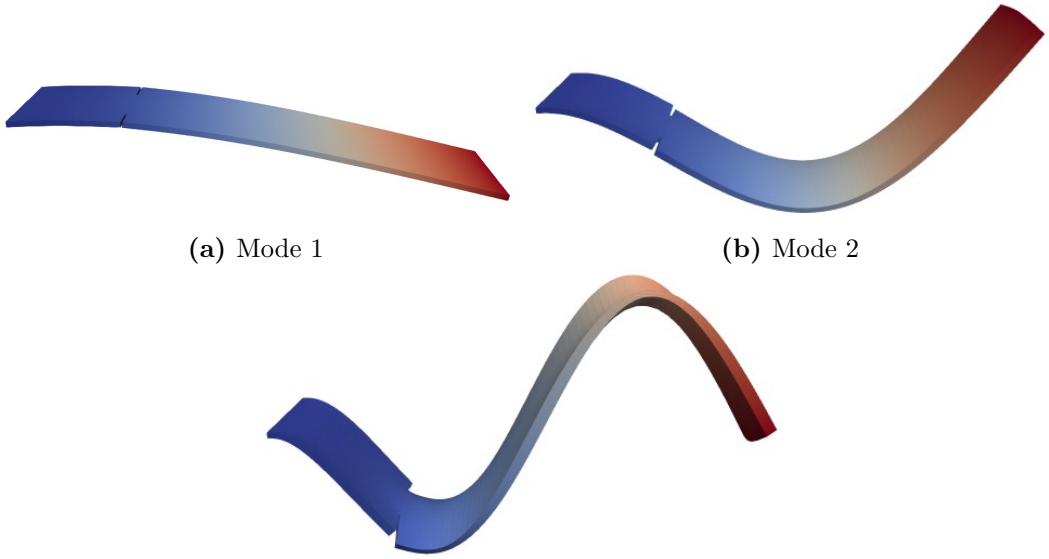

(a) Mode 1 **(b)** Mode 2

(c) Mode 3

Figure 7.5: First three bending modes of the cracked cantilever beam with $a = 7$ mm, modelled with 1280 Q9-LE1 elements in the CUF framework.

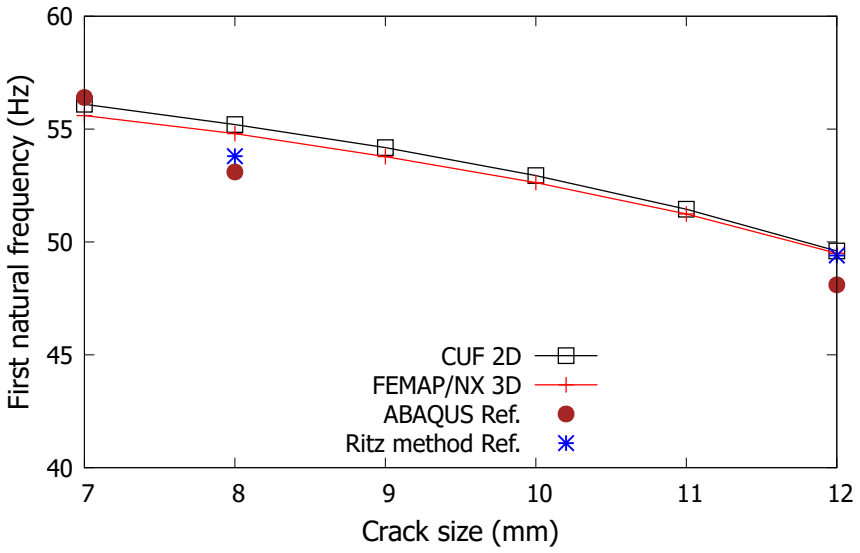

Figure 7.6: Variation of the first natural frequency with crack size. Comparison between CUF, FEMAP/NX, ABAQUS and Ritz method results.

this value is adopted here in the random response simulations. Since a modal reduction strategy is used, it is necessary to verify that a sufficient number of modes is retained to accurately reproduce the structural response. As shown in Fig. 7.7, considering the first ten modes ensures that more than 95% of the mass is involved in the response along the z-direction.

Figure 7.8 presents the FRF of the stress component σ_{yy} at the SG point, located

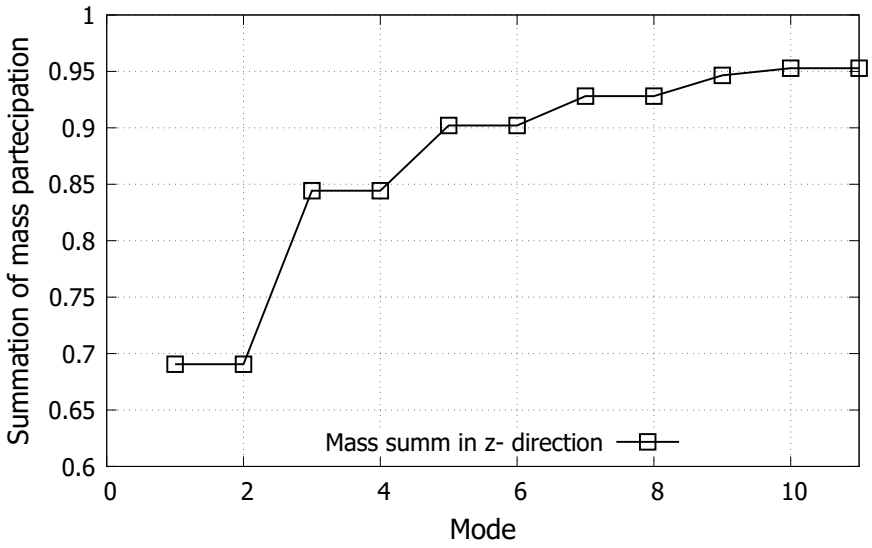

Figure 7.7: Cumulative mass participation as a function of the number of modes.

between the two cracks at 15 mm along x and 25 mm along y. In Fig. 7.8a, the FRFs obtained with the FEMAP model are shown for two different load representations: the direct excitation through base acceleration and the equivalent three-force scheme. The numerical results are compared with the experimental data reported in [148], showing good agreement. In Fig. 7.8b, the response predicted by the CUF model with 7 mm pre-cracks is compared with the FEMAP/NX model using the three-force approximation, and with the experimental and FEM–ABAQUS results from [148].

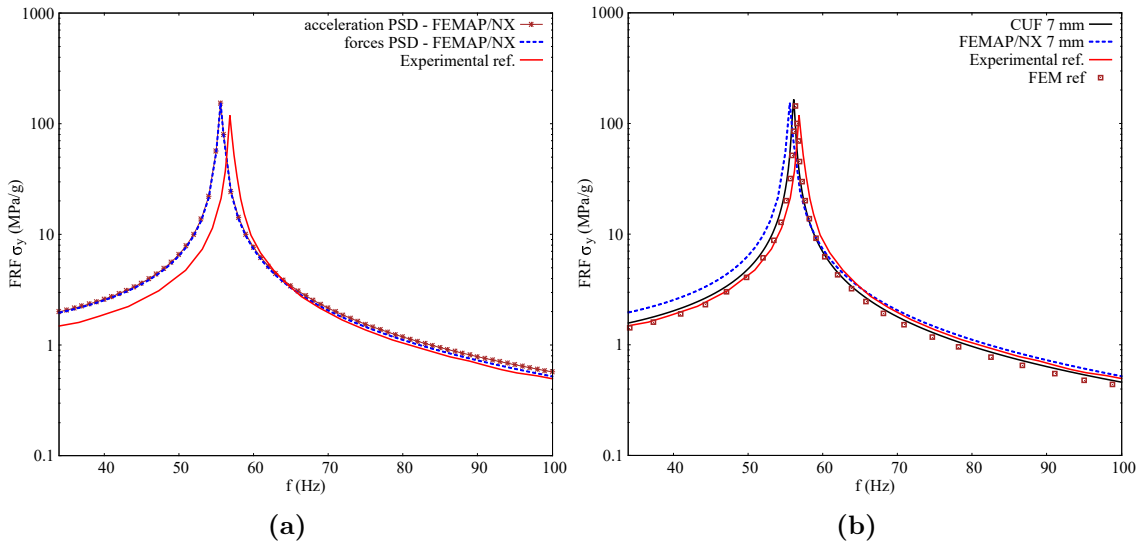

Figure 7.8: Frequency response functions (FRFs) of the stress σ_{yy} at the SG point: a) FEMAP/NX model, comparison between base-acceleration excitation and three-force approximation; b) CUF model with 7 mm pre-cracks compared with FEMAP/NX, experimental data and ABAQUS results from [148].

From the random response analysis, the following conclusions can be drawn:

1. As shown in Fig. 7.7, the inclusion of ten modes is sufficient to ensure more than 95% mass participation in the z-direction, thus guaranteeing an accurate modal representation of the dynamic response.

2. The simplified three-force loading model reproduces accurately the FRF of the stress at the SG point when compared with the direct base-acceleration excitation, as illustrated in Fig. 7.8a.

3. The CUF model with 7 mm pre-cracks yields FRFs in good agreement with both the experimental measurements and the solid-element finite element results, while requiring significantly fewer degrees of freedom and thus a lower computational cost.

Damage index

As outlined in Section 5.3.4, one possible way to quantify the effect of damage on the dynamic response is through a damage index. In the present work, the DI is evaluated using the magnitude of the velocity FRF at the free tip of the beam (point P1 in Fig. 7.2a), following the approach proposed in [148]. Figure 7.9 shows the evolution of the velocity FRF v_z (along the z-direction) at point P1 for different damage states, represented by crack lengths ranging from 7 mm to 12 mm in the frequency interval 34–100 Hz. Figures 7.9a and 7.9b display the results for the FEMAP and CUF models, respectively.

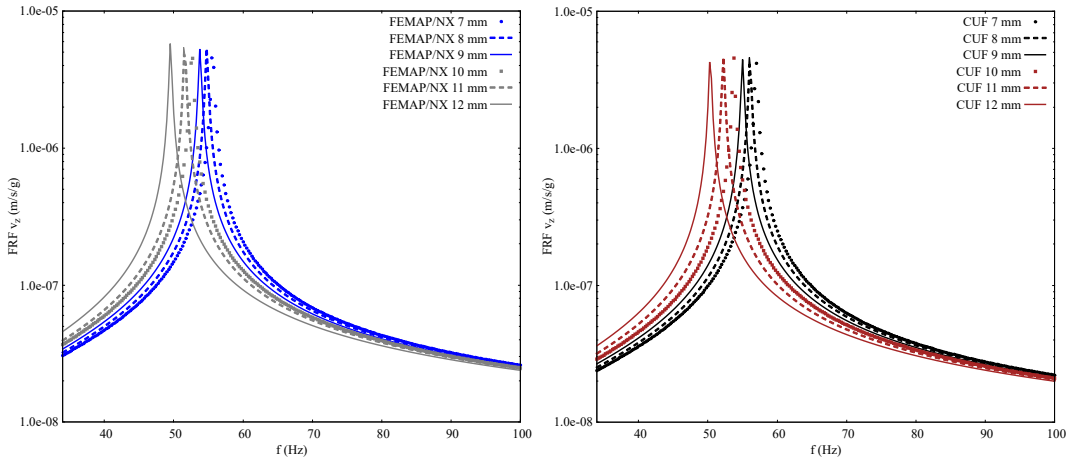

(a) FEMAP model **(b)** CUF model

Figure 7.9: Velocity FRFs along z at point P1 for different damage states: a) FEMAP model; b) CUF model.

For the calculation of the damage index, a wider frequency band from 34 Hz to 550 Hz with a resolution of 0.25 Hz is adopted, as depicted in Fig. 7.10. This choice is

motivated by the fact that the dominant contribution to the DI arises from the FRF amplitudes around the first two natural frequencies. In the experiments reported in [148], the DI is computed over the frequency range 34–2048 Hz with a resolution of 0.125 Hz, using a scanning laser vibrometer to measure the velocity in the z-direction at point P1. Figure 7.11 shows the DI as a function of crack size for both CUF and FEMAP/NX models, together with the 95% prediction band derived from the experimental data in [148], which is based on four tested specimens.

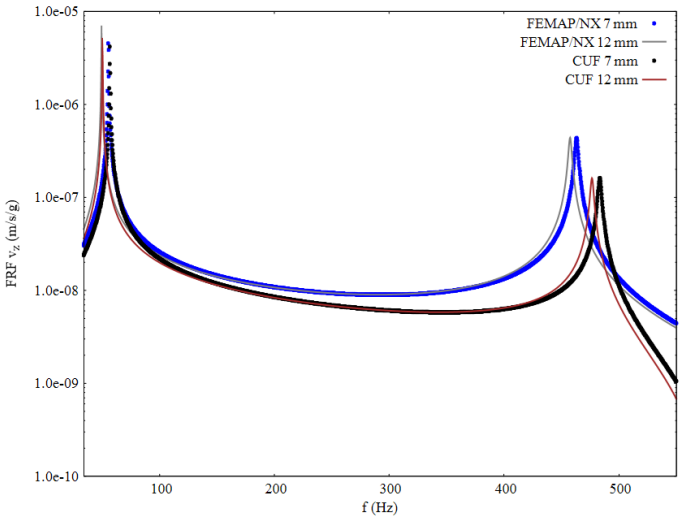

Figure 7.10: Velocity FRFs along z at point P1 in the 34–550 Hz range used for the DI computation. Comparison between the intact and final damage states for FEMAP/NX and CUF models.

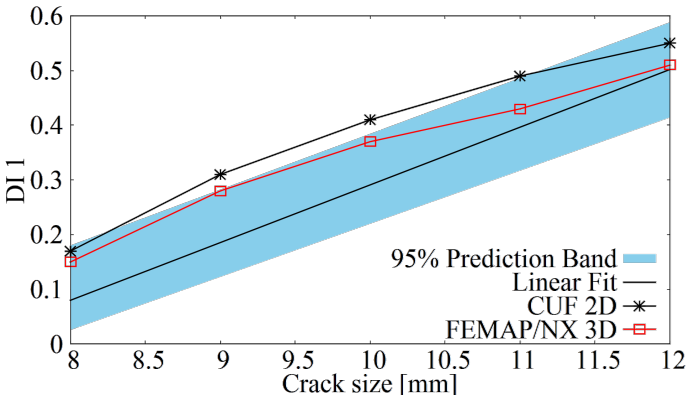

Figure 7.11: Damage index as a function of crack size. Comparison between CUF and FEMAP/NX predictions and the experimental 95% prediction band.

From the damage index analysis, the following remarks can be made:

1. As seen in Fig. 7.9, in the vicinity of the first natural frequency, the velocity FRFs at point P1 exhibit a similar trend for both numerical models. The percentage

reduction in the first natural frequency between $a = 7$ mm and $a = 12$ mm is about 11.0% for FEMAP/NX and 11.5% for CUF.

2. Figure 7.10 highlights that, near the first two natural frequencies, the CUF model predicts lower FRF amplitudes than the FEMAP/NX model.

3. As shown in Fig. 7.11, after reconstructing the absolute tip velocity in the numerical post-processing, the damage index predicted by both CUF and FEMAP/NX models exhibits a much closer agreement with the experimental 95% prediction band over the entire range of crack sizes. The differences are limited and can be attributed to modeling assumptions, such as the representation of the crack, damping, boundary conditions, and the implementation of the tip mass.

Fatigue life estimation

The final step of the analysis concerns fatigue life estimation. As described in Section 5.2.1, the stress amplitude PDF can be obtained using Dirlik's method, assuming a stress ratio $R = -1$. In Fig. 7.12, the stress PDF computed with Dirlik's method from the CUF-based stress PSD is compared with the numerical reference from [148] for the initial configuration with crack size $a = 7$ mm. The PDF corresponding to the subsequent crack lengths $a = 7, 8, 9, 10, 11$, and 12 mm are reported in Fig. 7.15.

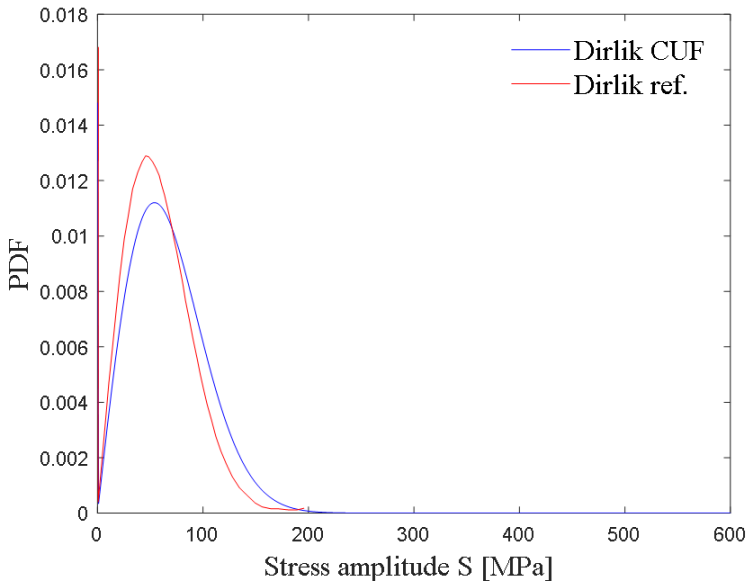

Figure 7.12: Stress PDF at $a = 7$ mm obtained via Dirlik's method using the CUF model, compared with numerical reference data from [148].

In [148], it is not explicitly stated whether the PDF used in the iterative crack-growth process is kept constant (evaluated at 7 mm) or updated as the crack propagates. To clarify this aspect, an analytical study was performed in which the modal

damping was adjusted to reproduce a FRF more closely aligned with the reference model, as illustrated in Fig. 7.13.

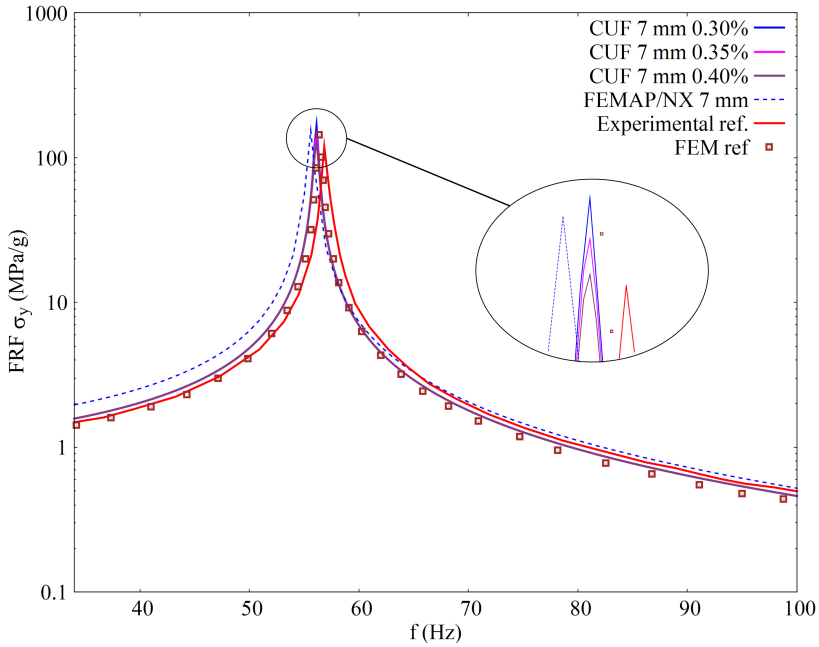

Figure 7.13: Comparison of stress FRFs for modal damping ratios of 0.30%, 0.35% and 0.40%.

The effect of varying the modal damping between 0.30% and 0.40% on the stress PDF is shown in Fig. 7.14a. The CUF model with a damping ratio of 0.40% provides the best match with the reference PDF.

Using a constant PDF evaluated at $a = 7$ mm, the fatigue life in terms of time can be derived from the crack growth analysis. Figure 7.14b shows the crack length versus time for the CUF model with the three considered damping ratios (0.30%, 0.35% and 0.40%).

The decision to keep the PDF fixed at the initial crack length of 7 mm rather than updating it as the crack grows can be motivated by several reasons. First, using a constant PDF simplifies the numerical procedure by avoiding the additional complexity associated with recalculating the stress distribution at each crack increment. Second, the reference model may have been calibrated based on the initial stress conditions at 7 mm, ensuring consistency of the fatigue life predictions. Third, allowing the PDF to evolve with crack size introduces further variability that may not be explicitly addressed in the original numerical or experimental framework. In the present study, however, the influence of PDF variation is explicitly examined, as illustrated in Fig. 7.15, where the PDFs corresponding to crack sizes $a = 7, 8, 9, 10, 11$ and 12 mm are reported.

To quantify the impact of this variability, Fig. 7.16 compares the crack growth curves obtained with the CUF approach for two scenarios: a constant PDF equal

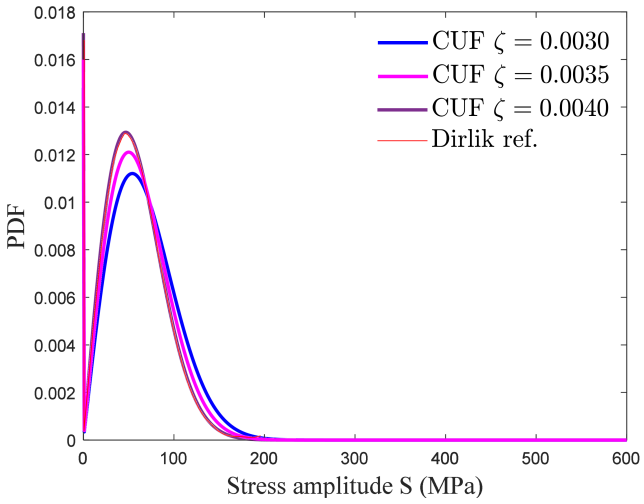

(a) Stress PDF

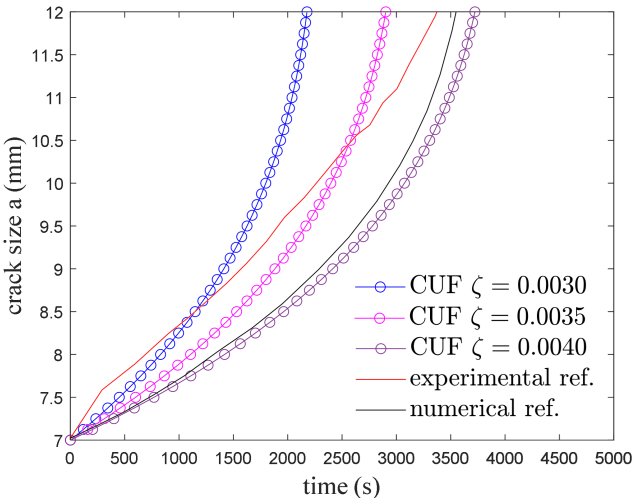

(b) Crack size versus time

Figure 7.14: Effect of modal damping (0.30%, 0.35% and 0.40%) on a) stress PDFs and b) crack growth curves.

to that at $a = 7$ mm and a variable PDF updated as the crack propagates. The results are compared with the experimental and numerical data reported in [148]. Maintaining a constant PDF corresponding to $a = 7$ mm in Fig. 7.18, the influence of mesh refinement on the predicted crack growth history is investigated. Since the PDF is kept fixed, the iterative update of the probabilistic description with increasing crack size is not considered. Under this assumption, progressively coarser meshes with a modal damping of 0.40% are employed to assess their impact on the crack size–time evolution. This analysis is not intended to represent a formal mesh convergence study, as convergence was already verified for the intact beam through modal analyses; rather, it aims at evaluating the sensitivity of the crack growth predictions

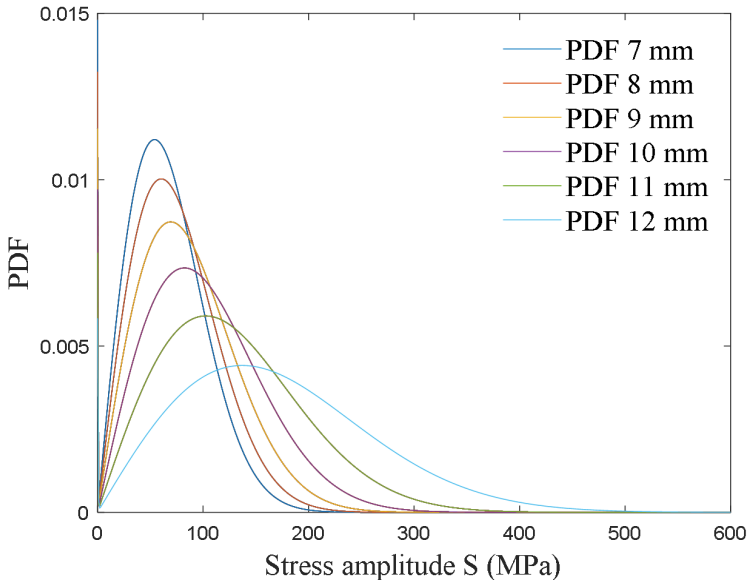

Figure 7.15: Stress PDFs obtained by Dirlik's method using the CUF model for crack sizes $a = 7, 8, 9, 10, 11$ and 12 mm.

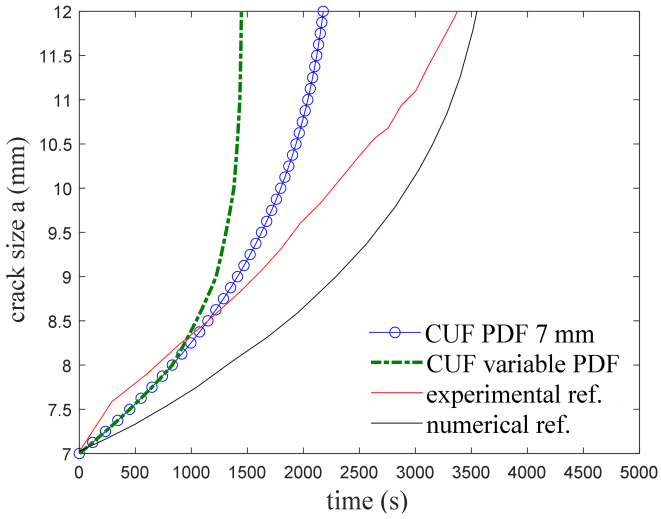

Figure 7.16: Crack size versus number of cycles obtained with the CUF model, comparing a constant PDF (evaluated at $a = 7$ mm) with variable PDFs updated for each crack size with a modal damping of 0.30%.

to mesh refinement under controlled probabilistic loading conditions. The comparison highlights a clear sensitivity of the predicted crack growth rate to the mesh density: as the number of elements is reduced, the numerical response shifts toward shorter propagation times, indicating an accelerated crack growth. This behavior can be attributed to the reduced capability of coarser meshes to accurately resolve local stress

gradients in the vicinity of the crack tip, which directly affects the damage driving quantities entering the growth law. Conversely, the finest mesh provides a smoother and more gradual crack propagation curve, closer to the numerical reference solution. For reference, Fig. 7.17 shows the finite element discretization corresponding to the coarsest configuration, consisting of 538 Q9-LE1 elements. In addition, Fig. 7.18 also reports the results obtained by adopting a higher-order CUF expansion (LE2) on the coarsest mesh. The 538 Q9-LE2 model provides a crack growth curve that closely approaches the response obtained with the finest 1280 Q9-LE1 configuration. This result highlights the capability of higher-order kinematic expansions to compensate for mesh coarsening, yielding comparable accuracy with a significantly reduced number of degrees of freedom. In particular, the 538 Q9-LE2 model involves 34065 DOF, whereas the 1280 Q9-LE1 model requires 47655 DOF, demonstrating a substantial gain in computational efficiency without a noticeable loss of accuracy.

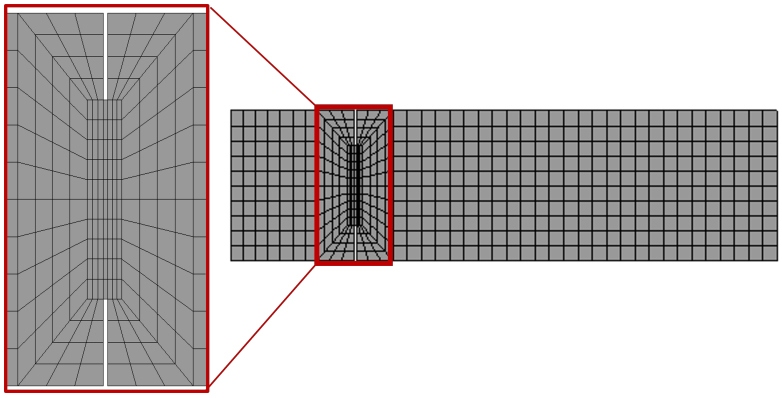

Figure 7.17: Mesh discretization of the structure with 538Q9 in CUF-2D.

From the analysis of the PDFs and the corresponding fatigue life estimates, the following conclusions can be drawn:

1. Even small differences in the stress FRF between the CUF model and the reference solution lead to noticeable deviations in the stress PDF for $a = 7$ mm, as shown in Fig. 7.12.

2. The stress amplitude PDF obtained via Dirlik's method with the CUF model shifts progressively towards higher stress values as the crack length increases from 7 mm to 12 mm, see Fig. 7.15. This behaviour indicates that crack propagation enhances local stress concentrations and raises the probability of high stress amplitudes. Although the global stiffness reduction tends to lower the natural frequencies, the modified stress field and possible modal interactions in the vicinity of the crack front can amplify local responses. As a result, the PDFs broaden and move towards higher stresses, indicating an increased likelihood of damaging load cycles.

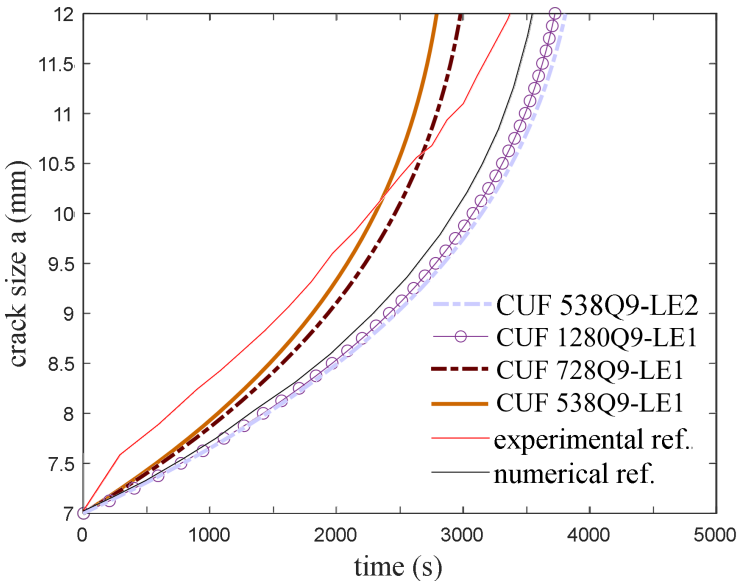

Figure 7.18: Crack size versus number of cycles obtained with the CUF model, maintaning a constant PDF (evaluated at $a = 7$ mm) reducing the number of the elements of the mesh of the beam with a modal damping of 0.40%.

3. In the iterative procedure used to estimate fatigue life in terms of both cycles and time, accounting for the evolving PDF leads to shorter predicted life. For a given crack size, the case with variable PDFs results in fewer cycles and a shorter time to failure than the constant-PDF case, as shown in Fig. 7.16.

4. Increasing the damping in the CUF model improves the agreement between the predicted PDF and the reference, as the FRF peaks are reduced. With a modal damping of 0.40%, the crack growth curve approaches the reference trend more closely, as illustrated in Fig. 7.14b.

5. When the PDF is kept constant and the iterative update with increasing crack size is not considered, the predicted crack growth history still exhibits a marked sensitivity to mesh refinement. As the number of elements is reduced, the crack size–time curves progressively shift towards shorter propagation times, indicating an acceleration of crack growth. This effect is attributed to the reduced capability of coarser meshes to accurately capture the local stress gradients near the crack tip.

6. The use of higher-order CUF kinematic expansions LE2 is shown to effectively reduce the sensitivity of crack growth predictions to mesh refinement, providing accuracy comparable to finer LE1 discretizations with a lower number of degrees of freedom.

7.1.2 T-shape composite specimen

This subsection introduces the fatigue assessment of a T-shaped composite structure subjected to broadband random excitation. The study is aimed at defining a representative composite test case, analysing its modal behaviour, and evaluating the random stress response and fatigue life for different laminate stacking sequences within a frequency-domain framework.

Test case definition

The investigated structure is a clamped-free T-shaped composite specimen manufactured in carbon-fibre reinforced polymer of T700 7.4. The in-plane geometry has an overall height of 166 mm and a maximum width of 110 mm. The vertical web has a width of 60 mm, while the root region is narrowed to 18 mm. A circular cut-out with radius $R = 15$ mm is introduced in the central region as illustrated in Fig. 7.19, producing a significant local stress concentration.

Table 7.4: Properties of T700 composite laminate.

Property	**Symbol**	**Value**
Modulus of elasticity along fibre direction	E_{11}	126 GPa
Modulus of elasticity across fibre direction	E_{22}, E_{33}	8.7 GPa
Shear modulus in plane 1–2 and 1–3	G_{12}, G_{13}	4 GPa
Shear modulus in plane 2–3	G_{23}	3.258 GPa
Poisson's ratio	ν_{12}, ν_{13}	0.3
Poisson's ratio	ν_{23}	0.335
Longitudinal tensile strength of lamina	X_T	1800 MPa
Longitudinal compressive strength of lamina	X_C	550 MPa
Transverse tensile strength of lamina	Y_T	25 MPa
Transverse compressive strength of lamina	Y_C	90 MPa
Shear strength of lamina in plane 1–2 and 1–3	S_{12}, S_{13}	180 MPa
Shear strength of lamina in plane 2–3	S_{23}	50 MPa
Density	ρ	1540 kg/m^3

The baseline laminate adopted for the reference configuration is a symmetric stacking sequence $[90/-45/45/0]_s$, which is representative of quasi-orthotropic composite layouts commonly used in lightweight structural components. Additional symmetric laminations are subsequently analysed to investigate the influence of ply orientation on the dynamic response and fatigue behaviour. Each layer of the laminate has a thickness of 0.125 mm. The geometry refers to the work developed in [66, 158].

Modal analysis

A preliminary modal analysis is performed in order to identify the dominant vibration modes and define the frequency range of interest for the random response analysis.

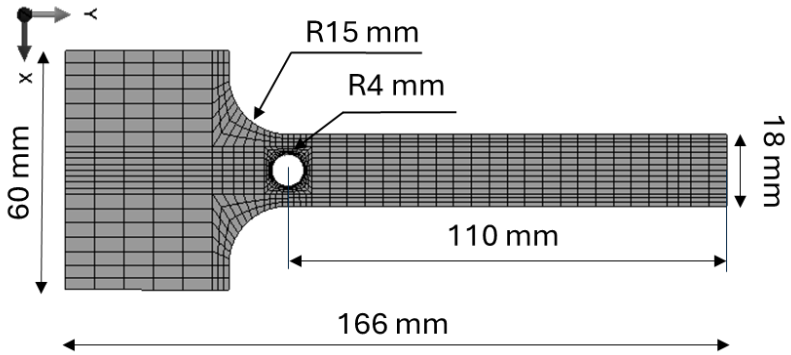

Figure 7.19: Geometry and mesh of T-shape T-700 composite laminate.

For the baseline laminate configuration, the first three natural modes are extracted and retained for the construction of a reduced-order modal basis. The structure is discretized in CUF-2D model by using 798 bi-quadratic element Q9 in plane and with a linear Lagrange expansion function LE1 for each layer along the thickness, resulting in 90828 DOFs. First, a modal analysis is conducted in order to evaluate and compare the natural frequencies obtained by 2D-CUF model and commercial software FEMAP/NX with both 2D and 3D approach as shown in Table 7.5. Table 7.6 compares the nu-

Table 7.5: Natural frequencies of the first three vibration modes of the T-shaped composite structure.

Natural frequencies	CUF–2D (Hz)	FEMAP/NX 2D (Hz)	FEMAP/NX 3D (Hz)
f_1	28.26	28.42	28.36
f_2	156.32	156.39	156.30
f_3	365.38	365.40	365.38

Table 7.6: Comparison of numerical models in terms of discretization and degrees of freedom.

Model	Elements	DOF
CUF–2D	798 Q9–LE1	90 828
FEMAP/NX 2D	728 shell	2 652
FEMAP/NX 3D model A	850 CHEXA	19 284
FEMAP/NX 3D model B	2 434 CHEXA	53 955

merical models in terms of discretization strategy and number of degrees of freedom. The FEMAP/NX 2D model is based on a laminated plate formulation using quadratic shell elements with eight nodes. The FEMAP/NX 3D models employ quadratic solid-laminate elements with twenty nodes. Two different meshes are considered, namely a coarser discretization (Model A) and a refined one (Model B). It should be noted that, when using solid-laminate elements, it is not straightforward to increase the number of elements along the thickness direction. Achieving a more refined through-thickness

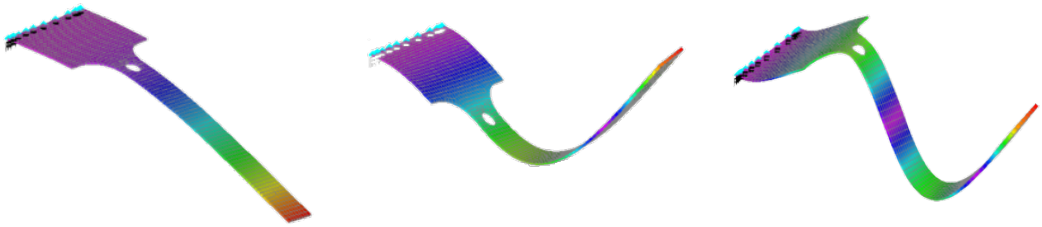

(a) FEMAP model **(b)** CUF model **(c)** CUF model

Figure 7.20: First three shape modes at a) f_1= 28.26 Hz, b) f_2= 156.32 Hz and c)f_2= 365.38 Hz.

stress representation would therefore require a different three-dimensional discretization strategy, which would lead to a substantial increase in the computational cost. As a consequence, the CUF approach represents an effective compromise between accuracy and computational efficiency for the analysis of laminated composite structures under random vibration.

Random response analysis

Following the modal characterization of the structure, a random vibration analysis is performed in order to evaluate the stochastic stress response of the T-shaped composite structure under broadband excitation. The analysis is carried out in the frequency domain, assuming linear elastic behavior, stationary Gaussian input loading and ten modes in the modal reduction strategy. The structure is subjected to a two concentrated forces described by a constant power spectral density of 0.5 g^2/Hz, representative of broadband random excitation, as shown in Fig. 7.21. The response

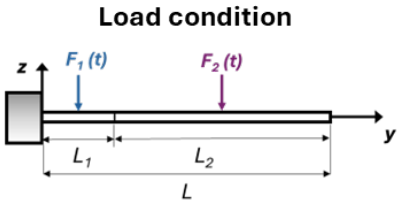

Figure 7.21: Boundary and loading condition of the T-shape composite structure.

is computed by exploiting the modal reduction introduced in the previous subsection. Only the first three vibration modes are retained, as they are sufficient to accurately capture the dynamic response within the frequency range of interest.
For a linear time-invariant system, the displacement response in the frequency domain is obtained by solving the reduced equilibrium equations in modal coordinates. The corresponding stress response is then reconstructed and expressed in terms of power spectral density functions.

Due to the multiaxial stress state arising within each composite ply, the individual stress components are combined into an equivalent stress extending the Tsai-Hill failure criterion, allowing the construction of an equivalent stress PSD at each material point. This approach enables the reduction of the multicomponent stochastic response to a scalar quantity while preserving the anisotropic nature of the laminate.
The spatial distribution of the equivalent stress RMS highlights the presence of a critical region in the vicinity of the geometric discontinuity introduced by the circular cut-out. This location is identified as the fatigue hot-spot and is therefore selected for subsequent fatigue life estimation, Fig. 7.22. The stress response is also evaluated at the ply level, allowing the identification of the critical ply governing damage initiation. For the $[90/-45/45/0]_s$ laminate, Fig. 7.23 shows the equivalent stress power spectral

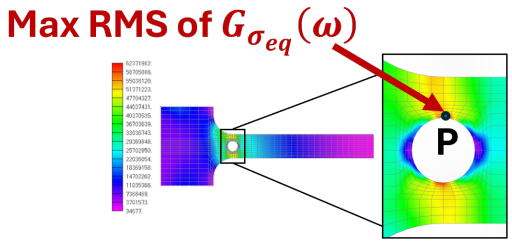

Figure 7.22: Maximum value of root mean square of the equivalent stress near the hole representing the fatigue hotspot by using FEMAP/NX.

densities evaluated in the 90°, −45° and 0° plies. In addition to the CUF-2D results obtained using a linear expansion (LE1), the figure also includes the corresponding predictions obtained with a higher-order CUF formulation (LE2). For the outer 90° ply, the CUF-2D results are compared with those obtained from FEMAP/NX using a two-dimensional shell model and two three-dimensional solid-laminate models characterised by different mesh densities.
A very good agreement is observed between the CUF-2D solution and the refined FEMAP/NX 3D model (Model B), whereas larger discrepancies are found when using the coarser three-dimensional discretization (Model A) and the two-dimensional shell model. The CUF-LE2 solution shows a slightly improved agreement with the 3D reference compared to LE1, confirming the enhanced through-thickness stress reconstruction provided by higher-order expansions. For the subsequent analyses, the comparisons are performed with respect to the FEMAP/NX 3D Model A. This choice is motivated by the need to balance accuracy and computational cost.
From the equivalent stress PSDs, it is also observed that the responses associated with the 0° plies are almost coincident across the different modeling approaches. In contrast, larger discrepancies arise in the ±45° plies, where the stress state is dominated by shear components. In these plies, the accuracy of the stress prediction is more sensitive to the through-thickness discretization, which explains the increased differences between the CUF formulation and the solid-laminate FEMAP/NX models.

Although the CUF-2D model involves a larger number of degrees of freedom than the FEMAP/NX models considered (see Table 7.6), the additional DOFs arise from higher–order kinematic terms introduced along the thickness direction. This allows an accurate reconstruction of the through-thickness stress distribution without resorting to a fully three-dimensional mesh. It is worth noting that refining the thickness resolution in solid–laminate models typically requires additional through–thickness discretisation, which may increase the overall model size. In the present study, the observed convergence of the FEMAP/NX results towards the CUF predictions is accompanied by a marked growth in degrees of freedom (Table 7.6). However, the improved accuracy obtained with the LE2 formulation is accompanied by a substantial increase in the number of 233223 degrees of freedom, resulting in significantly higher computational times. Since the subsequent analyses involve random vibration and fatigue simulations over long time histories and multiple parameter combinations, the LE2 models are therefore employed here as an accuracy benchmark, while the LE1 formulation is adopted for the subsequent parametric and fatigue analyses.

In order to compute the fatigue life in the fatigue hot-spot (point P), appropriate S–N curves must be introduced. In the reference work by Zhou et al. [66], the fatigue behavior of the composite material is described by means of normalized S-N curves derived from unidirectional specimens, expressed in terms of the equivalent stress ratio S/X, where X denotes the corresponding static strength. The failure of the laminate is assumed to be governed by the fatigue life of the critical ply.
The reference formulation provides different S-N relationships for several stress ratios R, and accounts for mean stress effects by interpolating the fatigue strength as a function of R at the cycle level. In the present work, in order to maintain consistency with the adopted frequency-domain fatigue framework and to avoid the introduction of additional cycle-by-cycle corrections, a constant stress ratio $R = -1$ is assumed for the equivalent stress. This choice corresponds to a fully reversed loading condition and represents a conservative approximation for broadband random vibration, where both tensile and compressive stress excursions are expected.
Accordingly, the S-N curve corresponding to $R = -1$ is employed for fatigue life estimation at the critical location and is expressed in the following logarithmic form:

$$\frac{S}{X} = 1 - 0.0515 \log_{10} N, \tag{7.2}$$

where N denotes the number of cycles to failure. The corresponding S-N curve is shown in Fig. 7.24. While a variable stress ratio formulation could further refine the fatigue life prediction, the adopted assumption ensures robustness and consistency in the comparative assessment of different laminate configurations under random vibration loading. In order to compute the fatigue life, the stress-range probability density function must be introduced. Figure 7.25 shows the probability density functions of the equivalent stress amplitude evaluated at the fatigue hot-spot for the individual

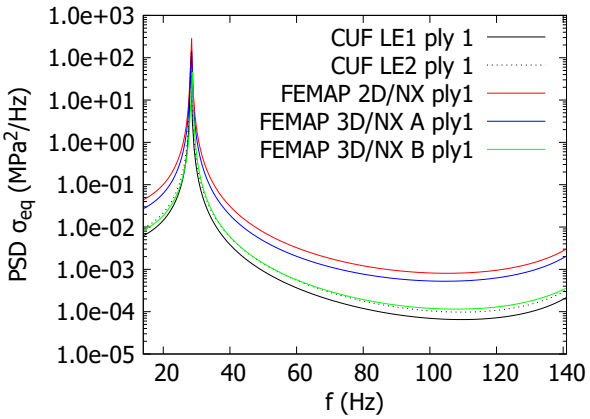

(a) Ply 90°

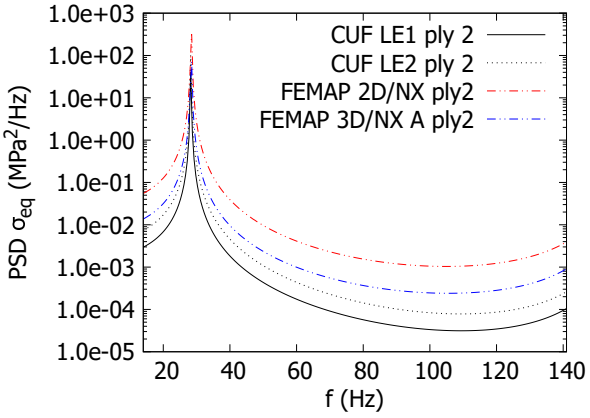

(b) Ply -45°

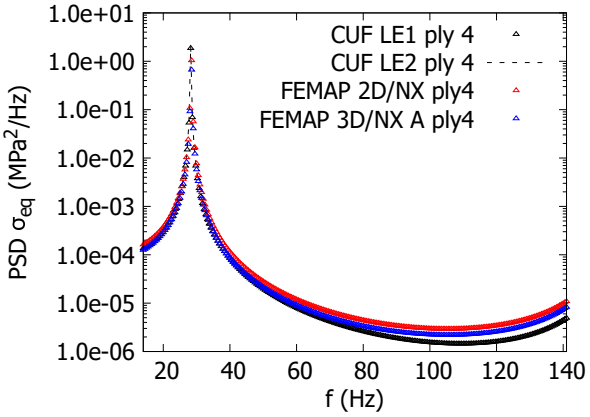

(c) Ply 0°

Figure 7.23: Equivalent stress PSD for $[90/-45/45/0]_s$ laminate in a) ply at 90°, b) ply at -45 ° and c)ply at 0°. Comparison with FEMAP 2D and both 3D model A and B for ply 90°

plies of the $[90/-45/45/0]_s$ laminate. The distributions are obtained from the equivalent stress power spectral density and describe the statistical occurrence of stress

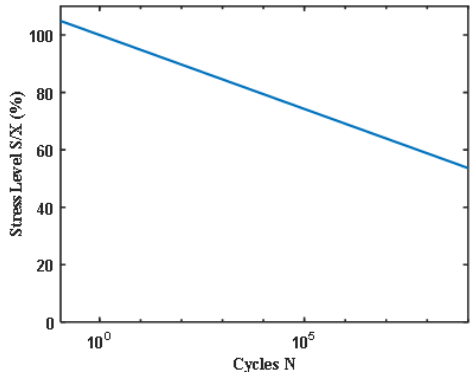

Figure 7.24: S-N curve of tension-compression with $R = -1$ [66].

cycles of different amplitudes under random vibration loading. As expected, the probability density functions exhibit higher values at low stress amplitudes, corresponding to a large number of small-amplitude cycles, while the probability of high-amplitude stress cycles rapidly decreases. Differences among the plies reflect the influence of ply orientation on the local stress response and, consequently, on the fatigue damage accumulation. Finally, the fatigue life estimates obtained for the different plies of the

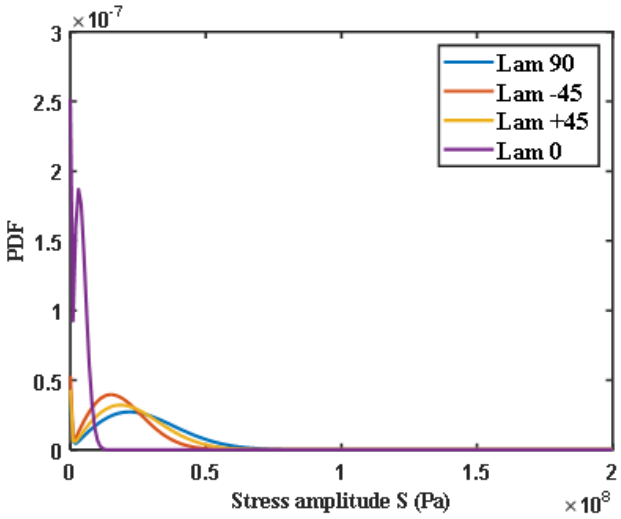

Figure 7.25: Probability density function of cycle stress amplitude for $[90/-45/45/0]_s$ laminate.

$[90/-45/45/0]_s$ laminate are shown in Fig. 7.26. The results are reported in terms of the normalized fatigue life ratio $T/T_{\min}$ and are compared against FEMAP/NX solutions using both a two-dimensional shell model and a three-dimensional solid-laminate model (Model A). $T_{\min}$ represents the minimum value of fatigue time, obtained as the lowest value of fatigue time among all laminate layers, consistently evaluated for both CUF-based theories and the FEMAP/NX model. In Fig. 7.26a, corresponding to the comparison with the FEMAP/NX 2D model, significant discrepancies are observed for

most plies. In particular, the predicted fatigue lives obtained from the shell-based formulation tend to deviate markedly from the CUF results, especially for the ±45° plies. This behaviour can be attributed to differences in the stress reconstruction strategy adopted by the two formulations. Although both models are based on two–dimensional kinematics, the CUF approach employs a refined layer–wise representation that allows a more accurate evaluation of in–plane shear stress components. In contrast, the shell–based formulation relies on classical laminate assumptions, which may lead to less accurate predictions of shear–dominated stress states.

Figure 7.26b plot reports the comparison between the CUF–2D model and the FEMAP/NX 3D Model A. In this case, a much closer agreement is observed for all plies, with the majority of the points lying near the bisector. Points located above the bisector correspond to cases in which FEMAP/NX predicts a longer fatigue life than CUF, whereas points below the bisector indicate more conservative CUF predictions. Overall, the results confirm that the CUF approach provides fatigue life estimates consistent with those obtained from a three-dimensional formulation, while maintaining a controlled computational cost.

As already observed in the stress PSD comparison, the best agreement is obtained for the 0° plies, whose response is mainly governed by normal stresses. Larger deviations are found for the ±45° plies, where shear stresses dominate and the accuracy of the fatigue prediction is more sensitive to the through-thickness stress reconstruction. For

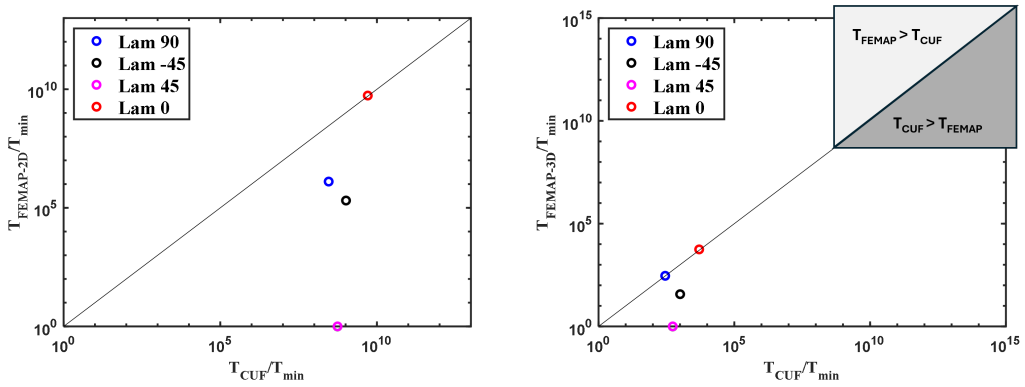

(a) Comparison with FEMAP/NX 2D **(b)** Comparison with FEMAP/NX 3D

Figure 7.26: Fatigue life comparison of $[90/-45/45/0]_s$ laminate between CUF-2D and a) FEMAP/NX 2D and b)FEMAP/NX 3D.

completeness, Fig. 7.27 additionally reports the comparison between the fatigue life estimates obtained with the CUF LE1 and LE2 formulations and the FEMAP/NX 3D Model A. The figure is included for illustrative purposes, in order to highlight the effect of increasing the expansion order on the predicted fatigue life. The results show that the adoption of the higher-order LE2 formulation generally leads to fatigue life estimates that move closer to the three-dimensional reference, particularly for the ±45° plies. This behavior is consistent with the trends observed in the stress PSD

analysis and reflects the improved through-thickness stress reconstruction provided by the higher-order CUF theory. For the 0° plies, whose response is mainly governed by normal stresses, the differences between LE1 and LE2 remain negligible. The influence

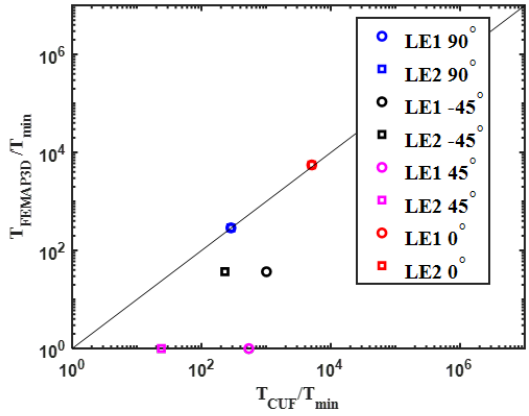

Figure 7.27: Comparison of the normalized fatigue life estimates obtained with CUF LE1 and LE2 formulations against the FEMAP/NX 3D Model A for the $[90/-45/45/0]_s$ laminate.

of the laminate stacking sequence on the random response is investigated by repeating the analysis for other two symmetric layups, $[0/45/-45/90]_s$ and $[0/90/0/90]_s$. Significant variations are observed in both the magnitude of the equivalent stress RMS and the shape of the stress PSD, reflecting the strong dependence of the dynamic behaviour on ply orientation and laminate anisotropy. These differences directly affect the statistical properties of the stress cycles and, consequently, the fatigue life predicted in the frequency domain. Figure 7.28 shows the probability density functions of the equivalent stress amplitude evaluated at the fatigue hot-spot located in point P (see Fig. 7.22)for the individual plies of the $[0/45/-45/90]_s$ laminate. In Fig.

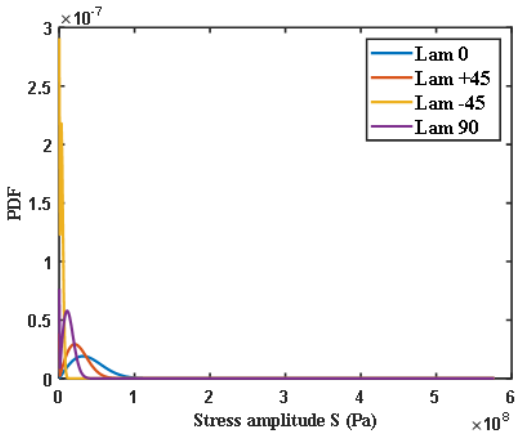

Figure 7.28: Probability density function of cycle stress amplitude for $[0/45/-45/90]_s$ laminate.

7.29 and Fig. 7.30 the fatigue life estimates obtained for the different plies of the $[0/45/-45/90]_s$ and $[0/90/0/90]_s$ laminate reported and listed in Table 7.7 and 7.8.

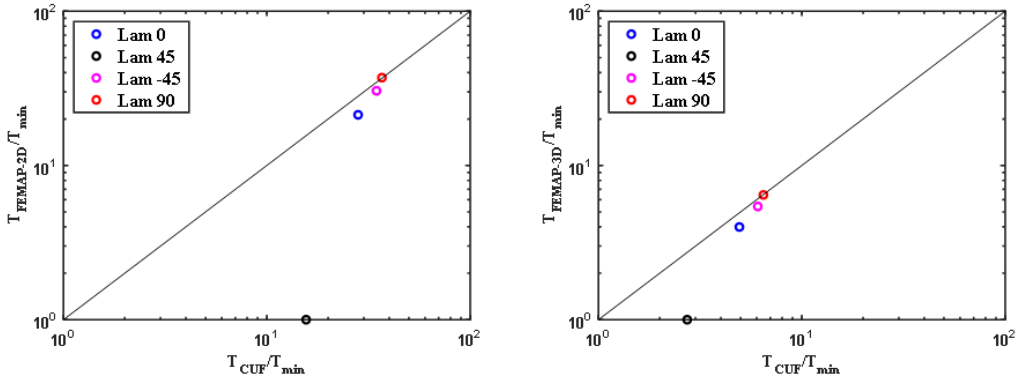

(a) Comparison with FEMAP/NX 2D **(b)** Comparison with FEMAP/NX 3D

Figure 7.29: Fatigue life comparison of $[0/45/-45/90]_s$ laminate between CUF-2D and a) FEMAP/NX 2D and b)FEMAP/NX 3D.

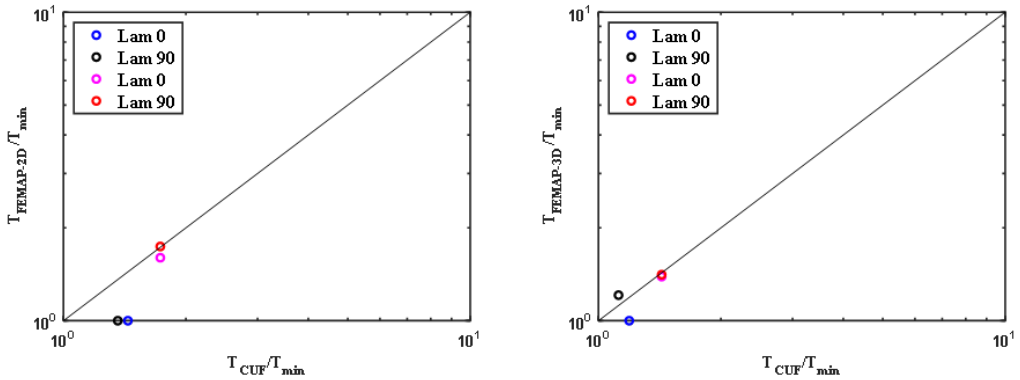

(a) Comparison with FEMAP/NX 2D **(b)** Comparison with FEMAP/NX 3D

Figure 7.30: Fatigue life comparison of $[0/90/0/90]_s$ laminate between CUF-2D and a) FEMAP/NX 2D and b)FEMAP/NX 3D.

For the $[0/45/-45/90]_s$ laminate, both CUF and FEMAP/NX identify the 45° ply as the fatigue hot-spot. In this case, the predicted fatigue lives show good agreement between CUF and FEMAP/NX, especially when compared with the three-dimensional model.

In the $[0/90/0/90]_s$ laminate, the fatigue hot-spot is located in the same ply for all approaches. The resulting fatigue lives exhibit a very good agreement between CUF and FEMAP/NX, with relative differences below approximately 16% for the three-dimensional model, as shown in Fig. 7.31. The reduced sensitivity to modelling assumptions in this configuration is associated with the dominance of normal stresses and the limited contribution of shear effects. Overall, the results clearly show that

Table 7.7: Fatigue life of the T-shaped composite structure with $[0/45/-45/90]_s$ under constant PSD excitation for each ply and comparison with FEMAP/NX 2D and 3D model.

Lamination	$\mathbf{T_f^{CUF2D}}$ (s)	$\mathbf{T_f^{FEMAP\ 2D}}$ (s)	$\mathbf{T_f^{FEMAP\ 3D}}$ (s)
0°	2.11×10^{18}	1.60×10^{18}	1.71×10^{18}
45°	1.17×10^{18}	7.52×10^{16}	4.28×10^{17}
−45°	2.60×10^{18}	2.29×10^{18}	2.32×10^{18}
90°	2.77×10^{18}	2.79×10^{18}	2.76×10^{18}

Table 7.8: Fatigue life of the T-shaped composite structure with $[0/90/0/90]_s$ under constant PSD excitation for each ply and comparison with FEMAP/NX 2D and 3D model.

Lamination	$\mathbf{T_f^{CUF2D}}$ (s)	$\mathbf{T_f^{FEMAP\ 2D}}$ (s)	$\mathbf{T_f^{FEMAP\ 3D}}$ (s)
0°	2.12×10^{18}	1.48×10^{18}	1.78×10^{18}
90°	2.01×10^{18}	1.46×10^{18}	2.15×10^{18}
0°	2.56×10^{18}	2.37×10^{18}	2.48×10^{18}
90°	2.56×10^{18}	2.57×10^{18}	2.52×10^{18}

the laminate stacking sequence plays a key role in determining both the location of the fatigue hot-spot and the magnitude of the predicted fatigue life. Discrepancies between CUF and FEMAP/NX are more pronounced in laminates where off-axis plies govern the response and shear stresses dominate, whereas excellent agreement is obtained for laminates dominated by 0° and 90° plies. From a modeling perspective, FEMAP/NX 2D shell models tend to underestimate or overestimate the fatigue life in configurations where through-thickness stress effects are relevant. In contrast, the CUF-2D formulation provides fatigue life estimates that are consistently close to those obtained with the three-dimensional FEMAP/NX model, while maintaining a controlled computational cost. These findings confirm the suitability of the CUF approach for frequency-domain fatigue analysis of laminated composite structures under random vibration loading. In particular, Fig. 7.32 summarises the effect of the laminate stacking sequence on the fatigue response at the fatigue hot-spot and in the most critical ply. Figure 7.32a reports the probability density functions of the equivalent stress amplitude for the four laminate configurations $[90/-45/45/0]_s$, $[0/45/-45/90]_s$, $[0/90/0/90]_s$ and $[-45/45/-45/45]_s$, while Fig. 7.32b shows the corresponding RMS values of the equivalent stress. The resulting fatigue life predictions obtained with the CUF–2D formulation are finally reported in Fig. 7.32c.

The comparison clearly indicates that the laminate configuration exhibiting the lowest RMS stress does not necessarily correspond to the longest fatigue life. Although the RMS provides a global measure of the energy content of the stress response, it does not capture the distribution of stress amplitudes governing fatigue damage. As shown in Fig. 7.32a, significant differences arise in the shape of the stress-range probability

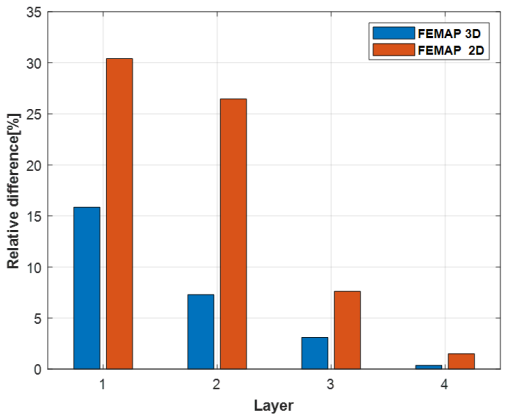

Figure 7.31: Differences in fatigue life prediction with respect to the CUF solution for each laminate ply of the $[0/90/0/90]_s$ laminate. Results obtained using FEMAP/NX 2D and FEMAP/NX 3D models are compared.

density functions, particularly in the distribution tail associated with higher stress amplitudes, which plays a dominant role in fatigue damage accumulation.
Furthermore, laminates characterized by similar RMS levels may still exhibit markedly different fatigue lives due to differences in the stress-cycle rate and in the overall shape of the PDF. As a consequence, a direct correlation between RMS and fatigue life cannot be established, as also evidenced by the comparison between Fig. 7.32b and Fig. 7.32c. These findings are fully consistent with the fundamental principles of frequency-domain fatigue analysis. Bishop and Sherratt [162] demonstrated that fatigue damage cannot be inferred from the stress variance alone, while Dirlik [52] and Lutes and Sarkani [54] showed that fatigue damage is governed by the stress-range probability density function and by the cycle rate rather than by the RMS value of the stress process. Similar conclusions were reported for composite laminates subjected to random loading by Zhou et al. [80], further supporting the physical consistency of the present results.

7.2 Von Kármán gust PSD load cases

This section addresses fatigue analyses performed under stochastic aerodynamic excitations modeled through a von Kármán (VK) turbulence spectrum. Two representative structural configurations are investigated in this subsection. The first case considers the composite T-shaped structure previously analyzed under constant PSD loading, now subjected to VK gust excitation in order to assess the influence of turbulence-driven loads on fatigue hot-spot location and life prediction. The second case involves a more complex wing box–beam model, representative of a simplified aircraft lifting structure, allowing the evaluation of the proposed frequency-domain fatigue framework under conditions that closely resemble real operational environments.

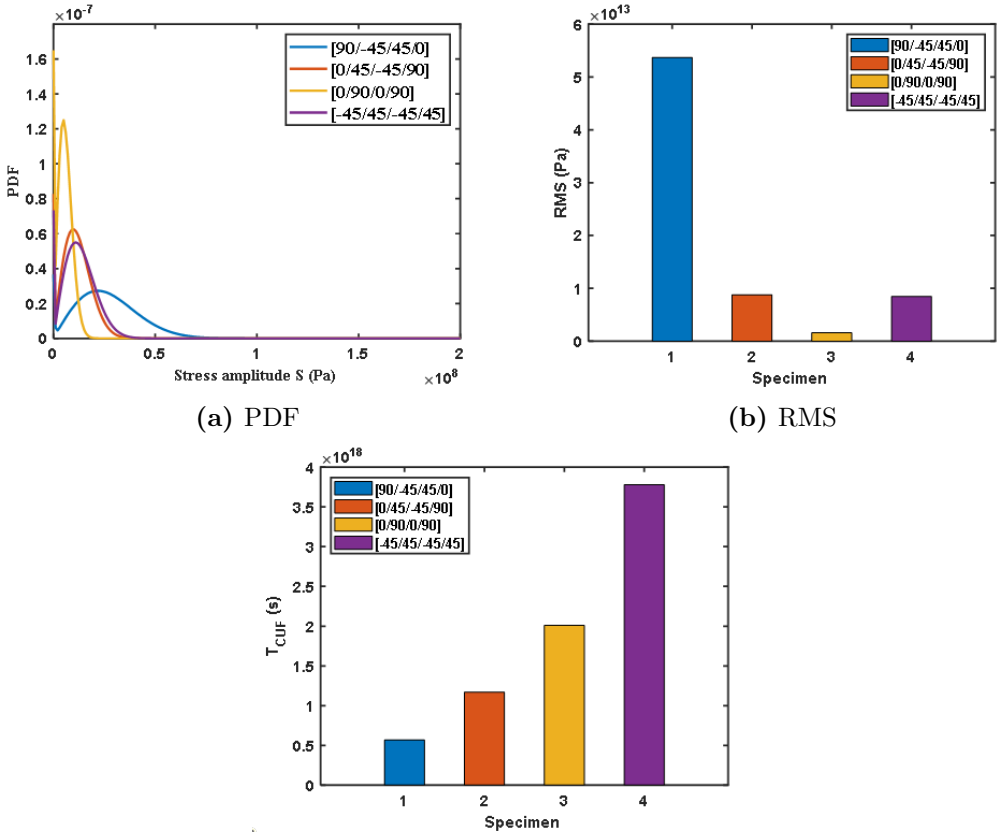

(a) PDF **(b)** RMS

(c) Fatigue life

Figure 7.32: Comparison of the fatigue response at the critical location for different laminate stacking sequences in terms of a) PDF of the equivalent stress amplitude, b) RMS values of the equivalent stress, and c) corresponding fatigue life predictions obtained with the CUF-2D formulation under broadband random excitation.

For both configurations, fatigue life predictions obtained using the CUF-based formulation are compared against reference finite element models, with particular attention paid to the role of laminate stacking sequence, load transfer mechanisms, and the interaction between aerodynamic excitation and structural dynamics.

7.2.1 T-shape composite specimen

Following the baseline analyses performed under constant PSD excitation, the same T-shaped composite specimen with $[90/-45/45/0]_s$ lamination is now investigated under stochastic aerodynamic loading modeled through a von Kármán gust spectrum. The discretization of CUF-2D model is of 798Q9-LE1, as in the previous case. In the present analysis, three different von Kármán spectra are considered by varying the scale length ($L = 0.5$, 1, and 2 m), while keeping the mean flow velocity constant. The selected values of L are chosen such that the knee of the gust PSD occurs in the

vicinity of the first natural frequency of the structure, in order to emphasize dynamic amplification effects, as in Fig 7.33. The gust velocity PSD is transferred to the

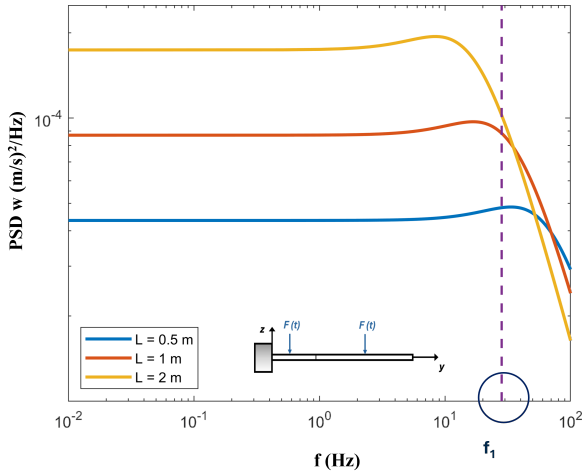

Figure 7.33: Gust von Kármán PSD varying by varying the scale length ($L = 0.5$, 1, and 2 m), while keeping $\sigma = 0.1$ m/s.

structural domain through the adopted load-assessment procedure, yielding the stress PSD at the most critical location of the structure. The fatigue assessment is carried out in the frequency domain using Dirlik's method, while multiaxial stress effects are accounted for through an equivalent stress definition based on the Tsai-Hill criterion. Consistently with the results obtained under constant PSD loading, the most critical ply is identified as the $+45°$ lamina, where shear-dominated stress components govern the fatigue damage accumulation as seen in Fig. 7.34 . The numerical results highlight

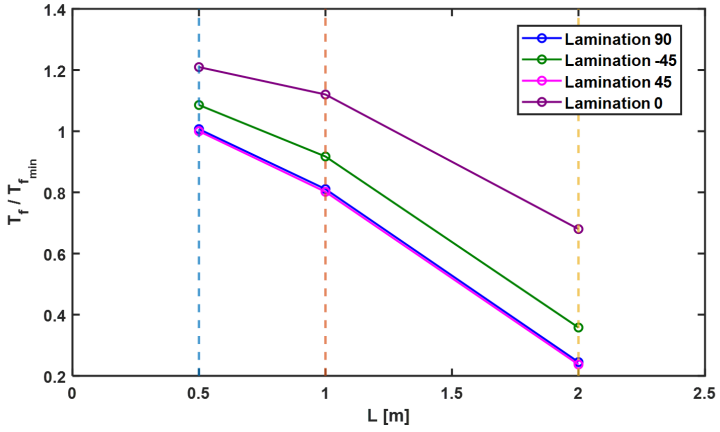

Figure 7.34: Fatigue response by varying the scale length ($L = 0.5$, 1, and 2 m), while keeping $\sigma = 0.1$ m/s for $[90/-45/45/0]_s$ laminate of T-shape composite structure.

a strong sensitivity of the predicted fatigue life to the characteristics of the von Kármán

spectrum. As L increases, significant variations in fatigue life are observed for all plies, with different trends depending on the lamina orientation, as reported in Fig. 7.34. In contrast to the constant PSD cases, the von Kármán excitation leads to non-uniform changes in fatigue life across the laminate, highlighting the influence of the turbulence parameters on the fatigue response. These results indicate that the fatigue behaviour of the T-shaped composite structure under VK excitation strongly depends on the characteristics of the imposed gust spectrum.

7.2.2 Composite wing box–beam

In order to investigate the applicability of the proposed frequency-domain fatigue framework to a more realistic aerospace structure, a composite wing box-beam model is considered in this subsection. The analyzed component represents a simplified structural approximation of the wing of the Pilatus PC-12 aircraft, selected as a representative example of a light turboprop configuration.
The wing is modeled as a straight box–beam structure with constant cross-section, whose geometry and material layout are designed to reproduce the main load-carrying mechanisms of the actual wing. This modeling choice allows retaining the essential features of the wing structural response, such as bending, torsion, and shear coupling, while enabling an efficient fatigue analysis within the CUF-based one-dimensional formulation.
Figure 7.35 provides a schematic overview of the reference aircraft and the corresponding box–beam idealization adopted in the present study. The von Kármán gust excitation is applied assuming a constant flight velocity, corresponding to the cruise condition of the aircraft, while turbulence parameters are varied to assess their influence on the fatigue response. The main geometric and operational characteristics of

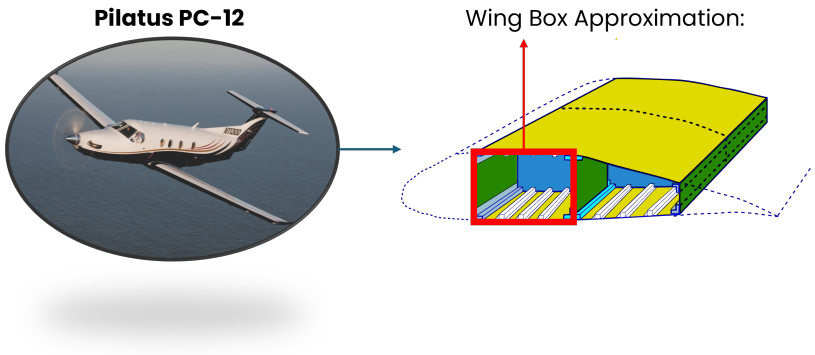

Figure 7.35: Wing box-beam approximation of Pilatus PC-12.

the Pilatus PC-12 aircraft, used as reference for the definition of the box–beam model and loading conditions, are summarized in Table 7.9 and derived from publicly available manufacturer data for the Pilatus PC-12 aircraft of EASA [163]. The box–beam

Table 7.9: Main characteristics of the Pilatus PC-12 aircraft [163].

Aircraft characteristic	**Value**
Length	14.40 m
Wingspan	16.28 m
Height	4.26 m
Wing area	25.81 m^2
Maximum take-off weight (MTOW)	4740 kg
Passengers	9 (standard)
Cruise speed	519 km/h

structure is assumed to be entirely made of composite material. Specifically, a T700 carbon fiber reinforced laminate is adopted as for T-shape specimen, whose elastic properties and strength parameters are reported in Table 7.4. This choice allows a realistic representation of the anisotropic mechanical behavior of modern composite wing structures while maintaining consistency with the fatigue material model employed in the subsequent analyses.
The thickness t of the box-beam skins is determined through a preliminary static sizing procedure, rather than being prescribed a priori. The sizing is performed by considering the maximum lift force acting on the wing under limit flight conditions, which is evaluated as

$$L_{\max} = n_{\max}\,\mathrm{MTOW}\,g, \tag{7.3}$$

where $n_{\max}$ is the maximum load factor and MTOW is the maximum take-off weight of the aircraft. According to the EASA Type Certificate Data Sheet No. EASA.A.089, the Pilatus PC-12 aircraft is characterized by $n_{\max} = 3.4$ and MTOW = 4740 kg.
Assuming a bending-dominated response and a thin-walled box-beam behavior, the maximum normal stress in the skins can be approximated as

$$\sigma \approx \frac{M}{b\,h\,t}, \tag{7.4}$$

where M is the bending moment, and b and h denote the width and height of the box cross-section, respectively. The thickness t is therefore selected so as to satisfy a strength-based constraint in compression, expressed as

$$t \geq \frac{M}{b\,h\,\sigma_{\mathrm{allow}}}, \tag{7.5}$$

where the allowable stress is conservatively taken as the longitudinal compressive strength of the lamina, $\sigma_{\mathrm{allow}} = X_C = 550$ MPa, as reported in Table 7.4.
The composite box-beam is modeled as a clamped–free structure, representative of a cantilever wing configuration. The adopted geometry and boundary conditions of the box-beam model are illustrated in Fig. 7.36. The composite box-beam cross-section

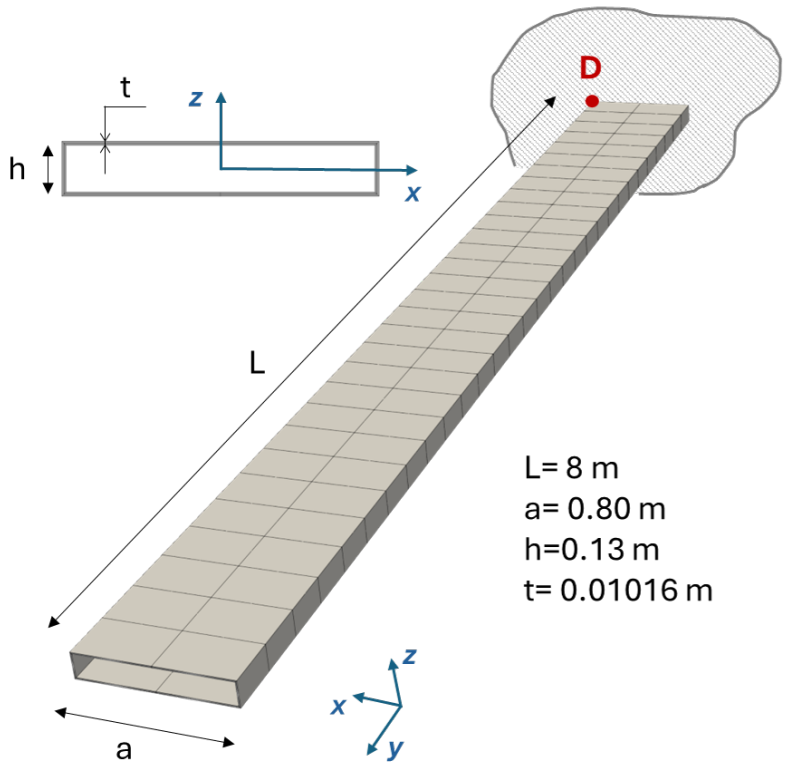

Figure 7.36: Geometry and boundary condition of wing box-beam structure..

is modeled using a two-layer laminate configuration, as schematically illustrated in Fig. 7.37. The laminate is characterized by two distinct ply orientation angles, denoted as θ_1 and θ_2, which are assigned to the outer and inner layers of the box–beam skins, respectively. This simplified layup allows investigating the influence of fiber orientation on the dynamic and fatigue response of the structure while keeping the model complexity limited. For the modal analysis presented in this subsection, a

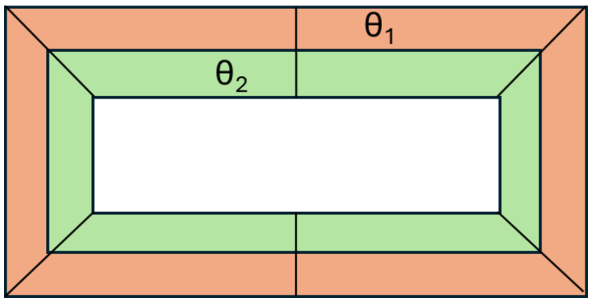

Figure 7.37: Schematic representation of the composite box–beam cross-section with a two-layer laminate configuration. The outer and inner layers are characterized by the ply orientation angles θ_1 and θ_2, respectively.

baseline configuration is considered in which both layers are aligned with the longitudinal axis of the beam, i.e. $\theta_1 = \theta_2 = 0°$. This choice provides a reference case dominated by axial stiffness and bending behavior, facilitating the interpretation of the modal characteristics and the convergence study of the CUF model. The effect of different laminate configurations, obtained by varying θ_1 and θ_2, is addressed in the subsequent random response and fatigue analyses.

Modal analysis

A preliminary modal analysis is carried out on the composite wing box-beam model in order to identify its dynamic characteristics and to select an appropriate level of kinematic refinement for the subsequent random response and fatigue analyses. The structure is analyzed in a clamped–free configuration, representative of a cantilever wing, as described in the previous subsection.
The structural model is developed within the Carrera Unified Formulation (CUF) framework using a one-dimensional finite element discretization along the beam axis. A total of 30 four-node beam elements (B4) are employed in the longitudinal direction. Across the cross-section, the displacement field is approximated using Taylor-type expansion functions with increasing orders to assess the convergence of the modal solution.
The convergence of the analysis is evaluated by monitoring the natural frequencies of the lowest vibration modes as the expansion order increases, as shown in Table . The results show that a Taylor Expansion of order TE7 provides a satisfactory compromise between accuracy and computational efficiency, yielding natural frequencies in close agreement with those obtained from a two-dimensional FEM model developed in FEMAP/NX. In particular, the reference FEMAP/NX 2D shell model features a total of 18 240 degrees of freedom, whereas the CUF-based model with TE7 expansion requires only 9 228 degrees of freedom, while preserving comparable modal accuracy. Increasing the expansion order beyond TE7 does not lead to significant improvements

Table 7.10: Comparison of the first five natural frequencies of the composite wing box–beam obtained with different CUF Taylor expansion orders and the FEMAP/NX 2D model.

Model	$\mathbf{f_1}$ (Hz)	$\mathbf{f_2}$ (Hz)	$\mathbf{f_3}$ (Hz)	$\mathbf{f_4}$ (Hz)	$\mathbf{f_5}$ (Hz)
FEMAP 2D	5.40	19.16	22.22	22.45	47.76
CUF TE1 (FSDT)	6.23	22.87	36.74	41.89	91.41
CUF TE3	5.90	22.31	22.14	28.41	63.19
CUF TE6	5.63	20.19	22.27	24.90	52.07
CUF TE7	5.53	18.74	22.25	23.82	41.55
CUF TE8	5.53	18.60	22.25	23.16	40.65

in the predicted modal properties, while it considerably increases the computational

cost. Based on these observations, the TE7 expansion is selected for the box-beam model and adopted in all subsequent analyses. This choice ensures an accurate representation of the structural dynamic behavior while preserving the numerical efficiency required for frequency-domain random response and fatigue life estimation.

Random response results

The random response of the composite wing box-beam under von Kármán gust excitation is investigated by adopting the load assessment procedure described in Chapter 6, where the gust power spectral density and the associated aerodynamic load transfer are introduced in detail. In the present analysis, the atmospheric turbulence is modeled through the von Kármán spectrum, and its effect on the structure is represented by an equivalent time-dependent distributed load derived from the unsteady lift response.
Specifically, the gust-induced vertical velocity fluctuations are first converted into variations of the lift coefficient by means of Küssner's model, accounting for the aerodynamic lag effects and the aircraft parameters in Table 7.9. The number of modes considered in modal reduction strategy are fourteen, in order to capture the correct dynamic behavior of the structure. The resulting lift spectrum is then transformed into a distributed load spectrum applied along the beam span. The load representation is shown in Fig. 7.38. The stress power spectral densities at the selected critical location

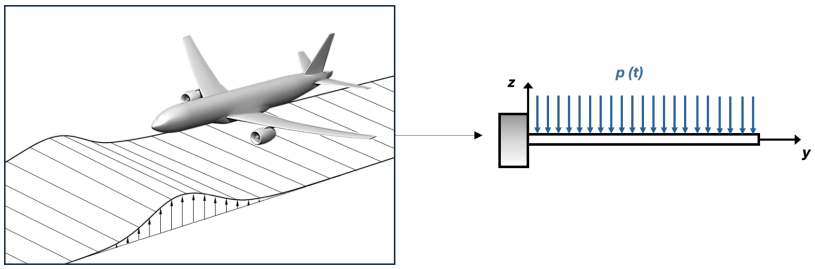

Figure 7.38: Representation of load condition of gust on the box-beam structure.

are computed using the CUF-based box-beam model with TE7 kinematic refinement. The random stress response is subsequently characterized in terms of stress-amplitude probability density functions (PDFs), evaluated through Dirlik's method. The analysis is carried out by varying the turbulence parameters, namely the turbulence intensity $\sigma = 0.1,\ 0.2,\ 0.3,\ 0.4$, and 0.5 m/s and turbulence scale length $L = 1,\ 5,\ 10$, and 15 m, while maintaining a constant flight velocity of 519 km/h as in Table 7.9. Figure 7.39 shows the von Kármán gust spectrum varying turbulence intensity σ and scale length L considering the knee of PSD near the first natural frequencies of the structure. The random response analysis is performed by considering two different laminate configurations for the composite box-beam. The first configuration corresponds to a fully aligned layup, with $\theta_1 = \theta_2 = 0°$, while the second one represents a cross-ply

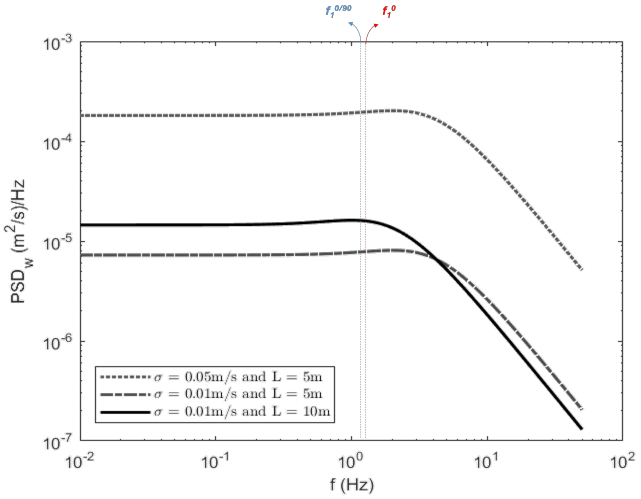

Figure 7.39: Von Kármán gust spectrum varying turbulence intensity σ and scale length L. Knees of the curves near the first natural frequencies of the structure.

arrangement, with $\theta_1 = 0°$ and $\theta_2 = 90°$. This choice allows investigating the influence of laminate anisotropy on the structural response under gust-induced loading.
The results are discussed in terms of the evolution of the stress-amplitude PDFs and their sensitivity to the gust parameters. Particular attention is paid to the broadening of the distributions and to the increase in the probability of large stress amplitudes as the turbulence intensity increases, which directly reflects a more severe fatigue loading condition for the composite box-beam. The stress-amplitude PDFs obtained for the two laminate configurations are reported in Figs. 7.40 and 7.41.

As seen in these figures, higher values of σ produces broader distributions with longer tails, while increasing L lowers the overall probability density. This indicates that larger turbulence intensity increases the variability of stress cycles, making higher stresses more likely, whereas increasing the characteristic length L increases the probability of large stress excursions and therefore leads to a less severe fatigue loading. In addition, a clear influence of the laminate configuration can be observed by comparing Figs. 7.40 and 7.41. For the same gust parameters, the cross-ply configuration generally exhibits broader stress-amplitude PDFs and a higher probability of medium-to-large stress amplitudes compared to the fully aligned layup. This behavior is attributed to the reduced load-carrying efficiency of the 90° plies under bending-dominated loading, which results in a more pronounced multiaxial stress state and increased stress fluctuations in the load-aligned plies. These trends anticipate a lower fatigue resistance and a higher sensitivity to turbulence intensity for the $\theta_1 = 0°$, $\theta_2 = 90°$ configuration, as further quantified in the fatigue life analysis presented in the following subsection.

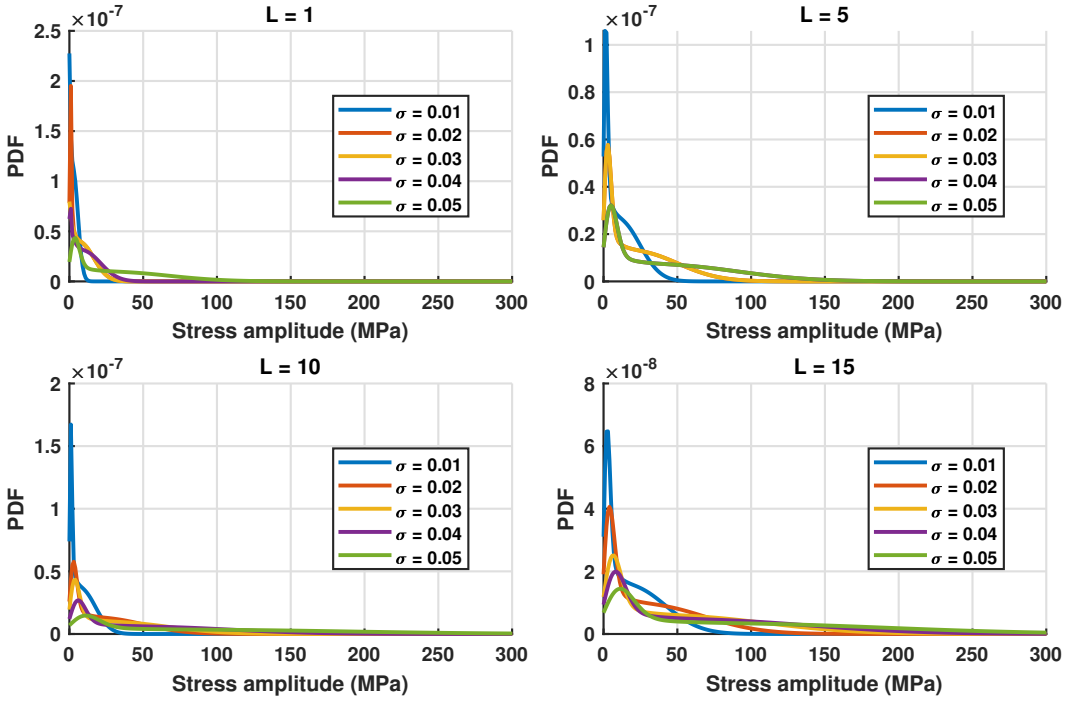

Figure 7.40: Stress-amplitude probability density functions (PDFs) evaluated at the selected critical location for different values of the turbulence intensity $\sigma = 0.1,\ 0.2,\ 0.3,\ 0.4$, and 0.5 m/s and turbulence scale length $L = 1,\ 5,\ 10$, and 15 m with $\theta_1 = \theta_2 = 0°$.

Fatigue life results

The fatigue life of the composite wing box-beam under von Kármán gust excitation is evaluated by coupling the stress-amplitude PDFs discussed in the previous subsection with the adopted fatigue damage model. The results are summarized in Fig. 7.42, which reports the iso-curves of the normalized fatigue life $T/T_{\min}$ as a function of the turbulence intensity σ and the integral scale length L for the two laminate configurations under consideration.

For the fully aligned laminate ($\theta_1 = \theta_2 = 0°$, Fig. 7.42a), the fatigue life exhibits a strong dependence on the turbulence intensity. Increasing σ leads to a rapid reduction of $T/T_{\min}$ over several orders of magnitude, indicating that the fatigue response is dominated by the energy content of the gust excitation. $T_{\min}$ corresponds to the minimum fatigue time obtaining by using different L and σ condition. The influence of the turbulence scale length L is less pronounced than that of the turbulence intensity σ, but it exhibits a clear monotonic trend. For both low and high values of σ, increasing L leads to a progressive reduction of the fatigue life. This behavior can be attributed to the shift of the gust spectral content toward lower frequencies, which enhances the excitation of the dominant bending modes of the structure and results in higher stress amplitudes.

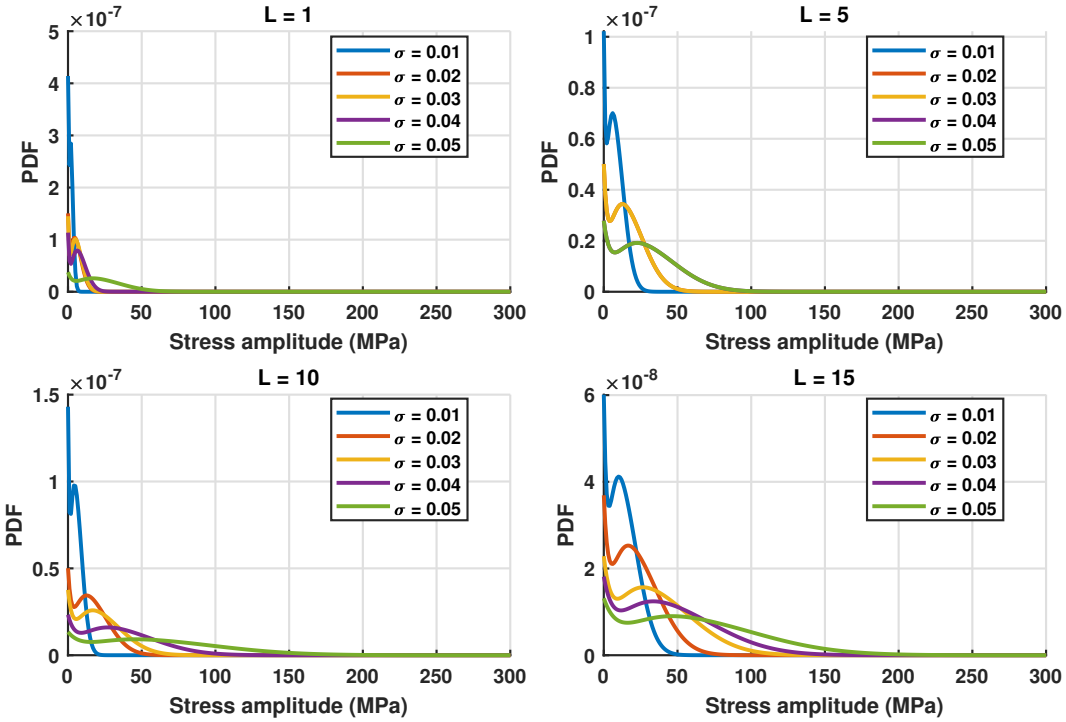

Figure 7.41: Stress-amplitude probability density functions (PDFs) evaluated at the selected critical location for different values of the turbulence intensity $\sigma = 0.1,\ 0.2,\ 0.3,\ 0.4$, and 0.5 m/s and turbulence scale length $L = 1,\ 5,\ 10$, and 15 m with $\theta_1 = 0°$ and $\theta_2 = 90°$.

A different behavior is observed for the cross-ply configuration ($\theta_1 = 0°$, $\theta_2 = 90°$, Fig. 7.42b). Although the same qualitative trends with respect to σ and L are preserved, the normalized fatigue life is generally lower compared to the fully aligned case. In addition, although the cross-ply configuration exhibits a lower overall fatigue life, the corresponding iso-contours are wider in the (σ, L) space. This indicates a reduced sensitivity of the fatigue life to variations in turbulence intensity and scale length, as the structure operates in a consistently fatigue-critical regime over a broad range of gust parameters.

Overall, the comparison between the two configurations highlights the dominant role of turbulence intensity σ in governing fatigue life, while the turbulence scale length L acts as a secondary parameter modulating the severity of the response through its interaction with the structural dynamics. The fully aligned laminate provides a more fatigue-resistant solution under gust loading, whereas the cross-ply configuration, despite offering reduced sensitivity in some regions of the parameter space, exhibits lower fatigue life due to the less efficient load transfer in the presence of transverse plies.

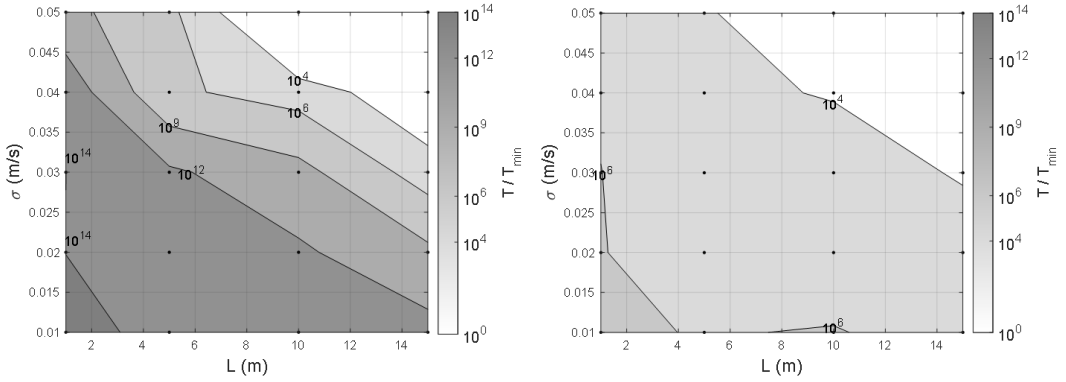

(a) 0° **(b)** 90°

Figure 7.42: Iso-curves of the normalized fatigue life $T/T_{\min}$ of the composite wing box-beam under von Kármán gust excitation as a function of the turbulence intensity σ and the integral scale length L: (a) fully aligned laminate $\theta_1 = \theta_2 = 0°$; (b) cross-ply laminate $\theta_1 = 0°$, $\theta_2 = 90°$.

7.3 Discussion

The results presented in this chapter demonstrate the effectiveness of the proposed frequency-domain framework for fatigue life prediction of both metallic and composite structures subjected to stochastic loading conditions. By combining high-fidelity CUF-based structural models with spectral fatigue methods, the approach enables an accurate yet computationally efficient assessment of fatigue damage under broadband random excitations.

For constant PSD load cases, the numerical results have highlighted the capability of the CUF formulation to capture the key features of the stress response governing fatigue damage, while maintaining a significantly reduced number of degrees of freedom compared to conventional finite element models. In metallic structures, the agreement with reference solutions confirms the reliability of frequency-domain fatigue methods when the stress response can be adequately characterized by second- order statistics. In composite configurations, the comparison between CUF and commercial FEM models has shown that high-order kinematic descriptions are essential to correctly represent interlaminar stress components and anisotropic effects, which play a crucial role in fatigue life estimation. Within this context, the role of higher-order CUF theories has been explicitly assessed for T-shape composite specimen with $[90/-45/45/0]_s$. The comparison between linear (LE1) and higher-order (LE2) expansions has shown that increasing the expansion order leads to a progressive convergence toward fully three-dimensional finite element solutions, both in terms of stress power spectral densities and fatigue life estimates.

When moving from constant PSD excitations to physically meaningful gust- induced loading, the von Kármán turbulence model has provided a realistic representation

of atmospheric excitation and its interaction with structural dynamics. The results clearly indicate that turbulence intensity σ is the dominant parameter governing fatigue life, as it directly controls the energy content of the excitation and, consequently, the amplitude of stress cycles. Increasing σ leads to broader stress-amplitude PDFs with heavier tails, resulting in a drastic reduction of fatigue life over several orders of magnitude.

The turbulence scale length L plays a secondary but non-negligible role. For all investigated configurations, increasing L leads to a monotonic decrease in fatigue life, due to the shift of the gust spectral content toward lower frequencies that are more effective in exciting the dominant bending modes of the structure. This behavior confirms that fatigue damage under gust loading is strongly influenced by the interaction between the load spectrum and the structural dynamic characteristics, rather than by load intensity alone.

The influence of laminate architecture has been shown to be particularly relevant for composite structures. The comparison between fully aligned ($[0°/0°]$) and cross-ply ($[0°/90°]$) configurations in the box–beam model reveals a clear trade-off between absolute fatigue performance and sensitivity to gust parameters. While the aligned laminate exhibits higher fatigue life, it is more sensitive to variations in σ and L, as reflected by steeper gradients in the fatigue life maps. Conversely, the cross-ply laminate shows a consistently lower fatigue life but a reduced sensitivity to turbulence parameters, operating in a uniformly fatigue-critical regime over a wide range of loading conditions. This behavior is consistent with the broader stress-amplitude PDFs observed in the random response analysis, which can be attributed to the presence of transverse plies that are not aligned with the dominant bending stresses, leading to increased stress heterogeneity across the laminate thickness.

Chapter 8

Conclusions

8.1 Overview of the Thesis

This thesis investigated the numerical modelling of progressive damage of composite structures and fatigue response of metallic and composite structures, with particular emphasis on the role of accurate three-dimensional stress reconstruction under quasi-static and stochastic loading conditions. The work was developed within the framework of the Carrera Unified Formulation (CUF), which enables the formulation of refined beam and shell models capable of reproducing three-dimensional stress states at a significantly reduced computational cost compared to full three-dimensional solid-element approaches.

The first part of the thesis focused on the progressive damage analysis of composite laminates under quasi-static loading conditions (Part II). A continuum damage mechanics framework was adopted and extended through the implementation of three-dimensional failure criteria. In particular, the Hashin 3D criterion was employed to describe tensile-dominated damage mechanisms, while a combined Hashin–Puck formulation was adopted to improve the modelling of compressive failure, especially in matrix-dominated regimes. These failure criteria were embedded within CUF-based two-dimensional finite element models, allowing the investigation of intralaminar damage mechanisms while retaining ply-level kinematics.

Progressive damage analyses were conducted on a wide range of benchmark configurations, including single-element tests, center-notched specimens, compact tension and compression tests, and open-hole laminates. The numerical results showed that refined CUF models are able to accurately reproduce experimental responses and reference numerical solutions, capturing damage initiation, damage propagation and stiffness degradation with good accuracy. The use of layer-wise formulations highlighted the necessity of retaining ply-level kinematics to correctly describe damage localization and stress redistribution, particularly in configurations governed by strong through-the-thickness stress gradients.

Although the progressive damage analyses were performed under quasi-static loading, they provided a physically consistent description of the governing damage mechanisms and stress transfer paths. These results constitute a fundamental basis for the subsequent extension to fatigue analysis under variable-amplitude and stochastic loading conditions.

Building on this foundation, the second part of the thesis (Part III) addressed fatigue life estimation in the frequency domain for both metallic and composite structures. The theoretical framework of random vibration analysis was introduced, and the structural response to stochastic excitation was characterized through stress power spectral densities obtained from CUF-based simulations. The Dirlik method was adopted to derive stress-range probability density functions directly from spectral information, enabling fatigue damage estimation without explicit time-domain simulations.

For metallic structures, the frequency-domain framework was coupled with linear elastic fracture mechanics concepts, allowing crack-growth prediction through equivalent stress intensity factor ranges derived from spectral stress information. The results demonstrated that CUF-based models provide stress frequency response functions and stress power spectral densities in very good agreement with experimental data and three-dimensional finite element solutions, while requiring a significantly reduced number of degrees of freedom.

For composite structures, the frequency-domain approach was extended through the definition of an equivalent stress based on the Tsai–Hill criterion, enabling fatigue life estimation while accounting for material anisotropy and multi-axial stress states. The analyses highlighted the strong influence of laminate stacking sequence on fatigue hot-spot location, stress distribution and fatigue life, confirming that accurate three-dimensional stress reconstruction is essential for reliable fatigue assessment.

Finally, fatigue analyses were performed under both idealized constant power spectral density excitation and physically based stochastic loading conditions derived from the von Kármán turbulence model. These investigations demonstrated the capability of the proposed CUF-based framework to capture the interaction between aerodynamic excitation, structural dynamics and fatigue damage accumulation under realistic operational environments.

For composite laminates, the proposed fatigue framework is primarily intended as an efficient life-prediction tool under random loading, rather than as a fully coupled fatigue–damage evolution model. In this perspective, the adoption of a frequency-domain formulation was also motivated by the need to preserve computational efficiency, whereas a fully coupled strategy would require a blockwise incremental analysis, with repeated re-evaluations of the structural response over successive fatigue intervals as stiffness progressively degrades, resulting in a substantially higher computational cost.

8.2 Main contributions

The main scientific contributions of this thesis are summarized below. For clarity, they are grouped according to the two main research topics addressed: progressive damage analysis and fatigue life estimation in the frequency domain.

Progressive damage analysis of composite Structures

- A refined CUF-based modelling strategy was developed for the progressive damage analysis of composite laminates, enabling the reconstruction of a full three-dimensional stress state using two-dimensional finite elements with a reduced computational cost.
- Three-dimensional failure criteria were implemented within the CUF framework. The Hashin 3D criterion was adopted for tensile-dominated damage mechanisms, while a combined Hashin–Puck formulation was employed to improve the prediction of compressive and matrix-dominated failure.
- Progressive damage analyses were performed on a variety of benchmark specimens, including notched and open-hole configurations, demonstrating the capability of the proposed approach to capture damage initiation, damage propagation and stiffness degradation in agreement with experimental and numerical reference data.
- The study highlighted the critical role of kinematic refinement in progressive damage modelling. Layer-wise CUF formulations were shown to be essential for accurately predicting damage localization and peak strength, whereas equivalent single-layer models exhibited limitations in the presence of strong ply-level stress gradients.
- The progressive damage analyses provided a physically consistent description of stress redistribution mechanisms, which was identified as a fundamental prerequisite for subsequent fatigue analyses under stochastic loading.

Fatigue life estimation in the frequency Domain

- A frequency-domain fatigue framework was developed using stress power spectral densities obtained from CUF-based simulations, enabling fatigue life prediction without explicit time-domain integration.
- For metallic structures, the framework was coupled with linear elastic fracture mechanics concepts, allowing crack-growth prediction through equivalent stress intensity factor ranges derived from spectral stress information.

- For composite structures, the frequency-domain approach was extended by introducing an equivalent stress definition based on the Tsai–Hill criterion, allowing fatigue life estimation while accounting for material anisotropy and multi-axial stress states.
- The study demonstrated that accurate three-dimensional stress reconstruction is essential for fatigue assessment in composite laminates. The results highlight the importance of an accurate stress evaluation strategy for reliable fatigue assessment, even within two-dimensional modelling frameworks.
- A systematic comparison with commercial finite element models confirmed that refined CUF-based formulations provide near three-dimensional accuracy in stress frequency response functions, stress power spectral densities and fatigue life predictions, at a significantly reduced computational cost.
- The analyses confirmed that fatigue damage cannot be inferred from RMS stress levels alone, and that the full stress-range probability density function governs fatigue damage accumulation, in agreement with established spectral fatigue theory.
- The influence of laminate stacking sequence on fatigue performance and sensitivity to stochastic loading parameters was quantified, revealing a trade-off between absolute fatigue life and robustness to variations in turbulence intensity and scale length.

8.3 Future perspectives

The results obtained in this thesis open several promising directions for future research. The most relevant perspectives are summarized below:

- Coupled progressive damage–fatigue modelling: extend the present framework to directly couple progressive damage evolution with frequency-domain fatigue analysis, allowing stiffness degradation to dynamically modify stress spectra and fatigue life predictions.
- Nonlinear dynamic response under stochastic loading: incorporate geometrical and material nonlinearities into the random response analysis in order to assess fatigue behaviour in structures where damage-induced stiffness changes affect the dynamic characteristics.
- Crack propagation and delamination in composites: extend the frequency-domain approach to explicitly model crack growth and delamination in composite laminates under stochastic excitation, bridging continuum damage mechanics and fracture mechanics-based fatigue models.

- Global–local and multi-scale strategies: combine CUF-based global models with refined local analyses in damage- and fatigue-critical regions to further improve accuracy while maintaining computational efficiency.
- Environmental and operational effects: include temperature, moisture and ageing effects within the fatigue framework to assess durability under realistic service conditions.
- Integration with structural health monitoring: couple the proposed frequency-domain framework with vibration-based damage indices and experimental data to enable predictive–monitoring strategies for damage tracking and remaining life estimation.
- Hybrid physics-based and data-driven approaches: use CUF-based high-fidelity simulations as data generators for machine learning models, enabling rapid fatigue assessment, uncertainty quantification and real-time decision support.
- Sensitivity analysis and uncertainty quantification: extend the present stochastic fatigue framework to include a structured assessment of the influence of uncertain parameters, such as damping ratios, turbulence characteristics, and material properties, on the predicted stress spectra and fatigue life. Such an extension would further enhance the robustness and certification relevance of the proposed methodology.

In summary, the methodologies developed in this thesis demonstrate that the CUF-based hierarchical modeling framework provides a versatile foundation for the unified analysis of progressive damage under quasi-static tension and compression loads, as well as fatigue under random excitation. A key advantage of the proposed approach lies in its intrinsic flexibility, which enables the kinematic description to be customized for the particular problem under consideration. By selecting an appropriate expansion order, the framework enables an effective balance between accuracy and computational efficiency, ensuring that higher-order theories are employed only when required to capture relevant three-dimensional stress effects.

Bibliography

[1] P. D. Mangalgiri. "Composite materials for aerospace applications". In: *Bulletin of Materials Science* 22.3 (May 1999), pp. 657–664. ISSN: 0973-7669. DOI: 10.1007/bf02749982.

[2] A.C. Orifici, I. Herszberg, and R.S. Thomson. "Review of methodologies for composite material modelling incorporating failure". In: *Composite Structures* 86.1–3 (Nov. 2008), pp. 194–210. ISSN: 0263-8223. DOI: 10.1016/j.compstruct.2008.03.007.

[3] T. Reytier, C. Bes, P. Marechal, M. Bianciardi, and A. Santgerma. "Generation of correlated stress time histories from continuous turbulence Power Spectral Density for fatigue analysis of aircraft structures". In: *International Journal of Fatigue* 42 (Sept. 2012), pp. 147–152. ISSN: 0142-1123. DOI: 10.1016/j.ijfatigue.2011.08.013.

[4] C. Galiotis and A. Paipetis. "Interfacial damage modelling of composites". In: *Multi-Scale Modelling of Composite Material Systems*. Elsevier, 2005, pp. 33–64. ISBN: 9781855739369. DOI: 10.1533/9781845690847.33.

[5] N. A. Fleck and B. Budiansky. "Compressive Failure of Fibre Composites Due to Microbuckling". In: *Inelastic Deformation of Composite Materials*. Springer New York, 1991, pp. 235–273. ISBN: 9781461391098. DOI: 10.1007/978-1-4613-9109-8_12.

[6] K. Niu and R. Talreja. "Modeling of compressive failure in fiber reinforced composites". In: *International Journal of Solids and Structures* 37.17 (Apr. 2000), pp. 2405–2428. ISSN: 0020-7683. DOI: 10.1016/s0020-7683(99)00010-4.

[7] X. Chen, X. Sun, B. Wang, J. Gu, P. Zou, Y. Chai, and J. Yang. "An improved longitudinal failure criterion for UD composites based on kinking model". In: *Mechanics of Advanced Materials and Structures* 29.6 (Aug. 2020), pp. 905–915. ISSN: 1537-6532. DOI: 10.1080/15376494.2020.1799269.

[8] P. D. Williams. "Increased light, moderate, and severe clear-air turbulence in response to climate change". In: *Advances in Atmospheric Sciences* 34.5 (Apr. 2017), pp. 576–586. ISSN: 1861-9533. DOI: 10.1007/s00376-017-6268-2.

[9] L. Zhang, B. Jiang, P. Zhang, H. Yan, X. Xu, R. Liu, J. Tang, and C. Ren. "Methods for fatigue-life estimation: A review of the current status and future trends". In: *Nanotechnology and Precision Engineering* 6.2 (June 2023), p. 025001. ISSN: 2589-5540. DOI: 10.1063/10.0017255.

[10] M. Muñiz-Calvente, A. Álvarez-Vázquez, F. Pelayo, M. Aenlle, N. García-Fernández, and M.J. Lamela-Rey. "A comparative review of time- and frequency-domain methods for fatigue damage assessment". In: *International Journal of Fatigue* 163 (Oct. 2022), p. 107069. ISSN: 0142-1123. DOI: 10.1016/j.ijfatigue.2022.107069.

[11] R. Talreja and C. V. Singh. *Damage and Failure of Composite Materials*. Cambridge University Press, June 2012. ISBN: 9781139016063. DOI: 10.1017/cbo9781139016063.

[12] E. Rivas, M. Parchei-Esfahani, and R. Gracie. "A two-dimensional extended finite element method model of discrete fracture networks". In: *International Journal for Numerical Methods in Engineering* 117.13 (Dec. 2018), pp. 1263–1282. ISSN: 1097-0207. DOI: 10.1002/nme.5999.

[13] M. J. Swindeman, E. V. Iarve, R. A. Brockman, D. H. Mollenhauer, and S. R. Hallett. "Strength Prediction in Open Hole Composite Laminates by Using Discrete Damage Modeling". In: *AIAA Journal* 51.4 (Apr. 2013), pp. 936–945. ISSN: 1533-385X. DOI: 10.2514/1.j051773.

[14] S. R. Hallett, W. Jiang, B. Khan, and M. R. Wisnom. "Modelling the interaction between matrix cracks and delamination damage in scaled quasi-isotropic specimens". In: *Composites Science and Technology* 68.1 (Jan. 2008), pp. 80–89. ISSN: 0266-3538. DOI: 10.1016/j.compscitech.2007.05.038.

[15] C. Yao, Q.H. Jiang, J.F. Shao, and C.B. Zhou. "A discrete approach for modeling damage and failure in anisotropic cohesive brittle materials". In: *Engineering Fracture Mechanics* 155 (Apr. 2016), pp. 102–118. ISSN: 0013-7944. DOI: 10.1016/j.engfracmech.2016.01.012.

[16] K. V. Williams, R. Vaziri, and A. Poursartip. "A physically based continuum damage mechanics model for thin laminated composite structures". In: *International Journal of Solids and Structures* 40.9 (May 2003), pp. 2267–2300. ISSN: 0020-7683. DOI: 10.1016/s0020-7683(03)00016-7.

[17] Z. P. Bažant and B. H. Oh. "Crack band theory for fracture of concrete". In: *Matériaux et Constructions* 16.3 (May 1983), pp. 155–177. ISSN: 1871-6873. DOI: 10.1007/bf02486267.

[18] S. W. Tsai and E. M. Wu. "A General Theory of Strength for Anisotropic Materials". In: *Journal of Composite Materials* 5.1 (Jan. 1971), pp. 58–80. ISSN: 1530-793X. DOI: 10.1177/002199837100500106.

[19] X. Li, D. Ma, H. Liu, W. Tan, X. Gong, C. Zhang, and Y. Li. "Assessment of failure criteria and damage evolution methods for composite laminates under low-velocity impact". In: *Composite Structures* 207 (Jan. 2019), pp. 727–739. ISSN: 0263-8223. DOI: 10.1016/j.compstruct.2018.09.093.

[20] O. Hoffman. "The Brittle Strength of Orthotropic Materials". In: *Journal of Composite Materials* 1.2 (Apr. 1967), pp. 200–206. ISSN: 1530-793X. DOI: 10.1177/002199836700100210.

[21] A. Rotem and Z. Hashin. "Failure Modes of Angle Ply Laminates". In: *Journal of Composite Materials* 9.2 (Apr. 1975), pp. 191–206. ISSN: 1530-793X. DOI: 10.1177/002199837500900209.

[22] R. Narayanaswami and H. M. Adelman. "Evaluation of the Tensor Polynomial and Hoffman Strength Theories for Composite Materials". In: *Journal of Composite Materials* 11.4 (Oct. 1977), pp. 366–377. ISSN: 1530-793X. DOI: 10.1177/002199837701100401.

[23] Z. Hashin. "Fatigue Failure Criteria for Unidirectional Fiber Composites". In: *Journal of Applied Mechanics* 48.4 (Dec. 1981), pp. 846–852. ISSN: 1528-9036. DOI: 10.1115/1.3157744.

[24] M.R.T. Arruda, L. Almeida-Fernandes, L. Castro, and J.R. Correia. "Tsai–Wu based orthotropic damage model". In: *Composites Part C: Open Access* 4 (Mar. 2021), p. 100122. ISSN: 2666-6820. DOI: 10.1016/j.jcomc.2021.100122.

[25] K. C. Warren, R. A. Lopez-Anido, S. S. Vel, and H. H. Bayraktar. "Progressive failure analysis of three-dimensional woven carbon composites in single-bolt, double-shear bearing". In: *Composites Part B: Engineering* 84 (Jan. 2016), pp. 266–276. ISSN: 1359-8368. DOI: 10.1016/j.compositesb.2015.08.082.

[26] C. Hühne, A.-K. Zerbst, G. Kuhlmann, C. Steenbock, and R. Rolfes. "Progressive damage analysis of composite bolted joints with liquid shim layers using constant and continuous degradation models". In: *Composite Structures* 92.2 (Jan. 2010), pp. 189–200. ISSN: 0263-8223. DOI: 10.1016/j.compstruct.2009.05.011.

[27] B. Mandal and A. Chakrabarti. "Simulating Progressive Damage of Notched Composite Laminates with Various Lamination Schemes". In: *International Journal of Applied Mechanics and Engineering* 22.2 (May 2017), pp. 333–347. ISSN: 2353-9003. DOI: 10.1515/ijame-2017-0020.

[28] P.P. Camanho, P. Maimí, and C.G. Dávila. "Prediction of size effects in notched laminates using continuum damage mechanics". In: *Composites Science and Technology* 67.13 (Oct. 2007), pp. 2715–2727. ISSN: 0266-3538. DOI: 10.1016/j.compscitech.2007.02.005.

[29] J. Reiner, T. Feser, D. Schueler, M. Waimer, and R. Vaziri. "Comparison of two progressive damage models for studying the notched behavior of composite laminates under tension". In: *Composite Structures* 207 (Jan. 2019), pp. 385–396. ISSN: 0263-8223. DOI: 10.1016/j.compstruct.2018.09.033.

[30] A. Puck and H. Schürmann. "Failure analysis of FRP laminates by means of physically based phenomenological models". In: *Failure Criteria in Fibre-Reinforced-Polymer Composites*. Elsevier, 2004, pp. 832–876. ISBN: 9780080444758. DOI: 10.1016/b978-008044475-8/50028-7.

[31] C. Dogan, M. O. Kaman, S. Erdem, and M. Albayrak. "Comparison of Hashin and Puck criterions for failure behavior of pin loaded composite plates". In: *Materialwissenschaft und Werkstofftechnik* 55.3 (Mar. 2024), pp. 314–329. ISSN: 1521-4052. DOI: 10.1002/mawe.202300104.

[32] C. Davila, N. Jaunky, and S. Goswami. "Failure Criteria for FRP Laminates in Plane Stress". In: *44th AIAA/ASME/ASCE/AHS/ASC Structures, Structural Dynamics, and Materials Conference*. American Institute of Aeronautics and Astronautics, Apr. 2003. DOI: 10.2514/6.2003-1991.

[33] M.H. Nagaraj, J. Reiner, R. Vaziri, E. Carrera, and M. Petrolo. "Progressive damage analysis of composite structures using higher-order layer-wise elements". In: *Composites Part B: Engineering* 190 (June 2020), p. 107921. ISSN: 1359-8368. DOI: 10.1016/j.compositesb.2020.107921.

[34] M.H. Nagaraj, J. Reiner, R. Vaziri, E. Carrera, and M. Petrolo. "Compressive damage modeling of fiber-reinforced composite laminates using 2D higher-order layer-wise models". In: *Composites Part B: Engineering* 215 (June 2021), p. 108753. ISSN: 1359-8368. DOI: 10.1016/j.compositesb.2021.108753.

[35] M. Trombini, M. Enea, M.R.T. Arruda, A. Pagani, M. Petrolo, and E. Carrera. "1D higher-order theories for quasi-static progressive failure analysis of composites based on a full 3D Hashin orthotropic damage model". In: *Composites Part B: Engineering* 270 (Feb. 2024), p. 111120. ISSN: 1359-8368. DOI: 10.1016/j.compositesb.2023.111120.

[36] Y. Zhang, W. Van Paepegem, and W. De Corte. "An Enhanced Progressive Damage Model for Laminated Fiber-Reinforced Composites Using the 3D Hashin Failure Criterion: A Multi-Level Analysis and Validation". In: *Materials* 17.21 (Oct. 2024), p. 5176. ISSN: 1996-1944. DOI: 10.3390/ma17215176.

[37] L. Bek, R. Kottner, and V. Laš. "Material model for simulation of progressive damage of composite materials using 3D Puck failure criterion". In: *Composite Structures* 259 (Mar. 2021), p. 113435. ISSN: 0263-8223. DOI: 10.1016/j.compstruct.2020.113435.

[38] S. Suresh. *Fatigue of materials*. Cambridge university press, 1998.

[39] O. H. Basquin. "The exponential law of endurance tests". In: *American Society of Testing Materials* (1910).

[40] L. F. Coffin. "A Study of the Effects of Cyclic Thermal Stresses on a Ductile Metal". In: *Journal of Fluids Engineering* 76.6 (Aug. 1954), pp. 931–949. ISSN: 0097-6822. DOI: 10.1115/1.4015020.

[41] S. S. Manson. *Behavior of materials under conditions of thermal stress*. National Advisory Committee for Aeronautics, 1953.

[42] J. Goodman. *Mechanics applied to engineering*. Longmans, Green, 1899.

[43] H. Gerber. *Bestimmung der zulässigen spannungen in eisen-constructionen*. Wolf, 1874.

[44] K. N. Smith, T. Topper, and P. Watson. "A stress-strain function for the fatigue of materials (stress-strain function for metal fatigue including mean stress effect)". In: *J Materials* 5 (1970), pp. 767–778.

[45] M. A. Miner. "Cumulative Damage in Fatigue". In: *Journal of Applied Mechanics* 12.3 (Sept. 1945), A159–A164. ISSN: 1528-9036. DOI: 10.1115/1.4009458.

[46] A. Fatemi and L. Yang. "Cumulative fatigue damage and life prediction theories: a survey of the state of the art for homogeneous materials". In: *International Journal of Fatigue* 20.1 (Jan. 1998), pp. 9–34. ISSN: 0142-1123. DOI: 10.1016/s0142-1123(97)00081-9.

[47] P. Paris and F. Erdogan. "A Critical Analysis of Crack Propagation Laws". In: *Journal of Basic Engineering* 85.4 (Dec. 1963), pp. 528–533. ISSN: 0021-9223. DOI: 10.1115/1.3656900.

[48] W. Elber. "Fatigue crack closure under cyclic tension". In: *Engineering Fracture Mechanics* 2.1 (July 1970), pp. 37–45. ISSN: 0013-7944. DOI: 10.1016/0013-7944(70)90028-7.

[49] M. W. Brown and K. J. Miller. "A Theory for Fatigue Failure under Multiaxial Stress-Strain Conditions". In: *Proceedings of the Institution of Mechanical Engineers* 187.1 (June 1973), pp. 745–755. ISSN: 2058-1203. DOI: 10.1243/pime_proc_1973_187_161_02.

[50] W. N. Findley. "A Theory for the Effect of Mean Stress on Fatigue of Metals Under Combined Torsion and Axial Load or Bending". In: *Journal of Engineering for Industry* 81.4 (Nov. 1959), pp. 301–305. ISSN: 0022-0817. DOI: 10.1115/1.4008327.

[51] J. W. Miles. "On Structural Fatigue under Random Loading". In: *The Journal of the Acoustical Society of America* 29.1 (Jan. 1957), pp. 176–176. ISSN: 1520-8524. DOI: 10.1121/1.1918447.

[52] T. Dirlik. "Application of computers in fatigue analysis". PhD thesis. University of Warwick, 1985.

[53] T. Dirlik and D. Benasciutti. "Dirlik and Tovo-Benasciutti Spectral Methods in Vibration Fatigue: A Review with a Historical Perspective". In: *Metals* 11.9 (Aug. 2021), p. 1333. ISSN: 2075-4701. DOI: 10.3390/met11091333.

[54] L. D. Lutes and S. Sarkani. *Random vibrations: analysis of structural and mechanical systems*. Elsevier, 2004.

[55] G. Di Giorgio. "Safety and Accidents Involving Aircraft Manufactured from Polymer Composite Materials: A Review". In: *Aerotecnica Missili & Spazio* 102.4 (Aug. 2023), pp. 337–353. ISSN: 2524-6968. DOI: 10.1007/s42496-023-00170-9.

[56] N. Post, S. Case, and J. Lesko. "Modeling the variable amplitude fatigue of composite materials: A review and evaluation of the state of the art for spectrum loading". In: *International Journal of Fatigue* 30.12 (Dec. 2008), pp. 2064–2086. ISSN: 0142-1123. DOI: 10.1016/j.ijfatigue.2008.07.002.

[57] A. P. Vassilopoulos, B. D. Manshadi, and T. Keller. "Influence of the constant life diagram formulation on the fatigue life prediction of composite materials". In: *International Journal of Fatigue* 32.4 (Apr. 2010), pp. 659–669. ISSN: 0142-1123. DOI: 10.1016/j.ijfatigue.2009.09.008.

[58] T. Philippidis and A. Vassilopoulos. "Complex stress state effect on fatigue life of GRP laminates.part I, experimental". In: *International Journal of Fatigue* 24.8 (Aug. 2002), pp. 813–823. ISSN: 0142-1123. DOI: 10.1016/s0142-1123(02)00003-8.

[59] M. Quaresimin, L. Susmel, and R. Talreja. "Fatigue behaviour and life assessment of composite laminates under multiaxial loadings". In: *International Journal of Fatigue* 32.1 (Jan. 2010), pp. 2–16. ISSN: 0142-1123. DOI: 10.1016/j.ijfatigue.2009.02.012.

[60] C. Caprile and G. Sala. "Fatigue Behaviour of CFRP Jointed Specimens". In: *Aerotecnica Missili & Spazio* 65.4 (1986), pp. 176–185.

[61] S. Goswami. "Response of Composite Stiffened Shells Under Stochastic Excitation". In: *Journal of Reinforced Plastics and Composites* 16.16 (Nov. 1997), pp. 1492–1522. ISSN: 1530-7964. DOI: 10.1177/073168449701601604.

[62] T. P. Philippidis and A. P. Vassilopoulos. "Fatigue Strength Prediction under Multiaxial Stress". In: *Journal of Composite Materials* 33.17 (Sept. 1999), pp. 1578–1599. ISSN: 1530-793X. DOI: 10.1177/002199839903301701.

[63] M. Gude, W. Hufenbach, I. Koch, and R. Protz. "Fatigue failure criteria and degradation rules for composites under multiaxial loadings". In: *Mechanics of Composite Materials* 42.5 (Sept. 2006), pp. 443–450. ISSN: 1573-8922. DOI: 10.1007/s11029-006-0054-z.

[64] S.C. Tan. "Effective Stress Fracture Models for Unnotched and Notched Multidirectional Laminates". In: *Journal of Composite Materials* 22.4 (Apr. 1988), pp. 322–340. ISSN: 1530-793X. DOI: 10.1177/002199838802200402.

[65] M. Kawai and T. Teranuma. "A multiaxial fatigue failure criterion based on the principal constant life diagrams for unidirectional carbon/epoxy laminates". In: *Composites Part A: Applied Science and Manufacturing* 43.8 (Aug. 2012), pp. 1252–1266. ISSN: 1359-835X. DOI: 10.1016/j.compositesa.2012.03.003.

[66] S. Zhou, Y. Sun, and L. Guo. "Random fatigue life prediction of carbon fibre-reinforced composite laminate based on hybrid time-frequency domain method". In: *Advanced Composite Materials* 26.2 (Mar. 2016), pp. 181–195. ISSN: 1568-5519. DOI: 10.1080/09243046.2016.1158935.

[67] K. Dang-Van. "Macro-Micro Approach in High-Cycle Multiaxial Fatigue". In: *Advances in Multiaxial Fatigue*. ASTM, Jan. 1993, pp. 120–130. ISBN: 9780803152434. DOI: 10.1520/stp24799s.

[68] M. Shokrieh. "Multiaxial fatigue behaviour of unidirectional plies based on uniaxial fatigue experiments — I. Modelling". In: *International Journal of Fatigue* 19.3 (Mar. 1997), pp. 201–207. ISSN: 0142-1123. DOI: 10.1016/s0142-1123(96)00074-6.

[69] M. Shokrieh. "Multiaxial fatigue behaviour of unidirectional plies based on uniaxial fatigue experiments—II. Experimental evaluation". In: *International Journal of Fatigue* 19.3 (Mar. 1997), pp. 209–217. ISSN: 0142-1123. DOI: 10.1016/s0142-1123(96)00068-0.

[70] M. Quaresimin and L. Susmel. "Multiaxial Fatigue Behaviour of Composite Laminates". In: *Key Engineering Materials* 221–222 (Dec. 2001), pp. 71–80. ISSN: 1662-9795. DOI: 10.4028/www.scientific.net/kem.221-222.71.

[71] A. Fatemi and D. F. Socie. "Acritical plane approach to multiaxial fatigue damage including out-of-phase loading". In: *Fatigue & Fracture of Engineering Materials & Structures* 11.3 (Mar. 1988), pp. 149–165. ISSN: 1460-2695. DOI: 10.1111/j.1460-2695.1988.tb01169.x.

[72] N. H. Yang, H. Nayeb-Hashemi, and A. Vaziri. "Multi-axial failure models for fiber-reinforced composites". In: *Journal of ASTM International* (2007).

[73] Y. Liu and S. Mahadevan. "A unified multiaxial fatigue damage model for isotropic and anisotropic materials". In: *International Journal of Fatigue* 29.2 (Feb. 2007), pp. 347–359. ISSN: 0142-1123. DOI: 10.1016/j.ijfatigue.2006.03.011.

[74] A. M. El-Assal and U. A. Khashaba. "Fatigue analysis of unidirectional GFRP composites under combined bending and torsional loads". In: *Composite Structures* 79.4 (Aug. 2007), pp. 599–605. ISSN: 0263-8223. DOI: 10.1016/j.compstruct.2006.02.026.

[75] D. Qi and G. Cheng. "Failure analysis of fiber-reinforced composites under multiaxial cyclic stress". In: *Polymer Composites* 29.8 (May 2008), pp. 922–931. ISSN: 1548-0569. DOI: 10.1002/pc.20419.

[76] N. E. Bedewi and D. N. Kung. "Effect of fatigue loading on the modal properties of composite structures and its utilization for prediction of residual life". In: *Composite Structures* 37.3–4 (Mar. 1997), pp. 357–371. ISSN: 0263-8223. DOI: 10.1016/s0263-8223(97)00028-7.

[77] P. Reis, J. Ferreira, J. Costa, and M. Richardson. "Fatigue life evaluation for carbon/epoxy laminate composites under constant and variable block loading". In: *Composites Science and Technology* 69.2 (Feb. 2009), pp. 154–160. ISSN: 0266-3538. DOI: 10.1016/j.compscitech.2008.09.043.

[78] Z. Wu, J. Liang, M. Fu, G. Fang, and Z. Zhou. "Study of random fatigue behavior of C/SiC composite thin-wall plates". In: *International Journal of Fatigue* 116 (Nov. 2018), pp. 553–561. ISSN: 0142-1123. DOI: 10.1016/j.ijfatigue.2018.07.001.

[79] V. A. Passipoularidis, T. P. Philippidis, and P. Brondsted. "Fatigue life prediction in composites using progressive damage modelling under block and spectrum loading". In: *International Journal of Fatigue* 33.2 (Feb. 2011), pp. 132–144. ISSN: 0142-1123. DOI: 10.1016/j.ijfatigue.2010.07.011.

[80] Y. Zhou, X. Hang, S. Wu, Q. Fei, and N. Trisovic. "Frequency-dependent random fatigue of panel-type structures made of ceramic matrix composites". In: *Acta Mechanica Solida Sinica* 30.2 (Apr. 2017), pp. 165–173. ISSN: 0894-9166. DOI: 10.1016/j.camss.2017.03.010.

[81] Z. Wu, Y. Zhao, J. Liang, M. Fu, and G. Fang. "A frequency domain approach in residual stiffness estimation of composite thin-wall structures under random fatigue loadings". In: *International Journal of Fatigue* 124 (July 2019), pp. 571–580. ISSN: 0142-1123. DOI: 10.1016/j.ijfatigue.2019.03.013.

[82] J. R. Schaff and B. D. Davidson. "Life Prediction Methodology for Composite Structures. Part I—Constant Amplitude and Two-Stress Level Fatigue". In: *Journal of Composite Materials* 31.2 (Jan. 1997), pp. 128–157. ISSN: 1530-793X. DOI: 10.1177/002199839703100202.

[83] J. R. Schaff and B. D. Davidson. "Life Prediction Methodology for Composite Structures. Part II—Spectrum Fatigue". In: *Journal of Composite Materials* 31.2 (Jan. 1997), pp. 158–181. ISSN: 1530-793X. DOI: 10.1177/002199839703100203.

[84] X. Chen, Y. Sun, Z. Wu, L. Yao, Y. Zhang, S. Zhou, and Y. Liu. "An investigation on residual strength and failure probability prediction for plain weave composite under random fatigue loading". In: *International Journal of Fatigue* 120 (Mar. 2019), pp. 267–282. ISSN: 0142-1123. DOI: 10.1016/j.ijfatigue.2018.10.013.

[85] Z. Fan, Y. Jiang, S. Zhang, and X. Chen. "Experimental Research on Vibration Fatigue of CFRP and Its Influence Factors Based on Vibration Testing". In: *Shock and Vibration* 2017 (2017), pp. 1–18. ISSN: 1875-9203. DOI: 10.1155/2017/1241623.

[86] L. Euler. *Methodus inveniendi lineas curvas maximi minimive proprietate gaudentes*. Springer Science & Business Media, 1952.

[87] S. P. Timoshenko. "LXVI. On the correction for shear of the differential equation for transverse vibrations of prismatic bars". In: *The London, Edinburgh, and Dublin Philosophical Magazine and Journal of Science* 41.245 (May 1921), pp. 744–746. ISSN: 1941-5990. DOI: 10.1080/14786442108636264.

[88] G. Kirchhoff. "Über das Gleichgewicht und die Bewegung einer elastischen Scheibe". In: *Journal für die reine und angewandte Mathematik (Crelles Journal)* 1850.40 (July 1850), pp. 51–88. ISSN: 1435-5345. DOI: 10.1515/crll.1850.40.51.

[89] E. Reissner. "The Effect of Transverse Shear Deformation on the Bending of Elastic Plates". In: *Journal of Applied Mechanics* 12.2 (June 1945), A69–A77. ISSN: 1528-9036. DOI: 10.1115/1.4009435.

[90] F. Gruttmann and W. Wagner. "Shear correction factors in Timoshenko's beam theory for arbitrary shaped cross-sections". In: *Computational Mechanics* 27.3 (Mar. 2001), pp. 199–207. ISSN: 1432-0924. DOI: 10.1007/s004660100239.

[91] N. Silvestre and D. Camotim. "First-order generalised beam theory for arbitrary orthotropic materials". In: *Thin-Walled Structures* 40.9 (Sept. 2002), pp. 755–789. ISSN: 0263-8231. DOI: 10.1016/s0263-8231(02)00025-3.

[92] N. Silvestre and D. Camotim. "Second-order generalised beam theory for arbitrary orthotropic materials". In: *Thin-Walled Structures* 40.9 (Sept. 2002), pp. 791–820. ISSN: 0263-8231. DOI: 10.1016/s0263-8231(02)00026-5.

[93] R. Gonçalves and D. Camotim. "Generalised beam theory-based finite elements for elastoplastic thin-walled metal members". In: *Thin-Walled Structures* 49.10 (Oct. 2011), pp. 1237–1245. ISSN: 0263-8231. DOI: 10.1016/j.tws.2011.05.011.

[94] R. Gonçalves and D. Camotim. "Geometrically non-linear generalised beam theory for elastoplastic thin-walled metal members". In: *Thin-Walled Structures* 51 (Feb. 2012), pp. 121–129. ISSN: 0263-8231. DOI: 10.1016/j.tws.2011.10.006.

[95] C. E. S. Cesnik and D. H. Hodges. "VABS: A New Concept for Composite Rotor Blade Cross-Sectional Modeling". In: *Journal of the American Helicopter Society* 42.1 (Jan. 1997), pp. 27–38. ISSN: 2161-6027. DOI: 10.4050/jahs.42.27.

[96] W. Yu, V. V. Volovoi, D. H. Hodges, and X. Hong. "Validation of the Variational Asymptotic Beam Sectional Analysis". In: *AIAA Journal* 40.10 (Oct. 2002), pp. 2105–2112. ISSN: 1533-385X. DOI: 10.2514/2.1545.

[97] R. D. Mindlin. "Influence of Rotatory Inertia and Shear on Flexural Motions of Isotropic, Elastic Plates". In: *Journal of Applied Mechanics* 18.1 (Mar. 1951), pp. 31–38. ISSN: 1528-9036. DOI: 10.1115/1.4010217.

[98] J. N. Reddy. "A Simple Higher-Order Theory for Laminated Composite Plates". In: *Journal of Applied Mechanics* 51.4 (Dec. 1984), pp. 745–752. ISSN: 1528-9036. DOI: 10.1115/1.3167719.

[99] J. N. Reddy. "A generalization of two-dimensional theories of laminated composite plates". In: *Communications in Applied Numerical Methods* 3.3 (May 1987), pp. 173–180. ISSN: 1555-2047. DOI: 10.1002/cnm.1630030303.

[100] J. N. Reddy and C. F. Liu. "A higher-order shear deformation theory of laminated elastic shells". In: *International Journal of Engineering Science* 23.3 (Jan. 1985), pp. 319–330. ISSN: 0020-7225. DOI: 10.1016/0020-7225(85)90051-5.

[101] A. N. Palazotto and S. T. Dennis. *Nonlinear Analysis of Shell Structures*. American Institute of Aeronautics and Astronautics, Jan. 1992. ISBN: 9781600862199. DOI: 10.2514/4.862199.

[102] P. R. Heyliger and J. N. Reddy. "A higher order beam finite element for bending and vibration problems". In: *Journal of Sound and Vibration* 126.2 (Oct. 1988), pp. 309–326. ISSN: 0022-460X. DOI: 10.1016/0022-460x(88)90244-1.

[103] E. Carrera. "A class of two-dimensional theories for anisotropic multilayered plates analysis". In: *Atti della accademia delle scienze di Torino. Classe di scienze fisiche matematiche e naturali* (1995).

[104] E. Carrera. "Theories and Finite Elements for Multilayered Plates and Shells:A Unified compact formulation with numerical assessment and benchmarking". In: *Archives of Computational Methods in Engineering* 10.3 (Sept. 2003), pp. 215–296. ISSN: 1886-1784. DOI: 10.1007/bf02736224.

[105] E. Carrera, M. Cinefra, M. Petrolo, and E. Zappino. *Finite element analysis of structures through unified formulation*. John Wiley & Sons, 2014.

[106] A. G. de Miguel, I. Kaleel, M. H. Nagaraj, A. Pagani, M. Petrolo, and E. Carrera. "Accurate evaluation of failure indices of composite layered structures via various FE models". In: *Composites Science and Technology* 167 (Oct. 2018), pp. 174–189. ISSN: 0266-3538. DOI: 10.1016/j.compscitech.2018.07.031.

[107] Y. Yan, A. Pagani, and E. Carrera. "Exact solutions for free vibration analysis of laminated, box and sandwich beams by refined layer-wise theory". In: *Composite Structures* 175 (Sept. 2017), pp. 28–45. ISSN: 0263-8223. DOI: 10.1016/j.compstruct.2017.05.003.

[108] E. Zappino, T. Cavallo, and E. Carrera. "Free vibration analysis of reinforced thin-walled plates and shells through various finite element models". In: *Mechanics of Advanced Materials and Structures* 23.9 (Mar. 2016), pp. 1005–1018. ISSN: 1537-6532. DOI: 10.1080/15376494.2015.1121562.

[109] R. B. Bharati, M. Filippi, P. K. Mahato, and E. Carrera. "Flutter analysis of laminated composite structures using Carrera Unified Formulation". In: *Composite Structures* 253 (Dec. 2020), p. 112759. ISSN: 0263-8223. DOI: 10.1016/j.compstruct.2020.112759.

[110] M. Filippi and E. Carrera. "Aerodynamic and mechanical hierarchical aeroelastic analysis of composite wings". In: *Mechanics of Advanced Materials and Structures* 23.9 (Mar. 2016), pp. 997–1004. ISSN: 1537-6532. DOI: 10.1080/15376494.2015.1121561.

[111] M. Filippi and E. Carrera. "Dynamic Analyses of Axisymmetric Rotors Through Three-Dimensional Approaches and High-Fidelity Beam Theories". In: *Journal of Vibration and Acoustics* 139.6 (Aug. 2017), p. 061008. ISSN: 1048-9002. DOI: 10.1115/1.4036927.

[112] M. Cinefra, M. Petrolo, G. Li, and E. Carrera. "Variable kinematic shell elements for composite laminates accounting for hygrothermal effects". In: *Journal of Thermal Stresses* 40.12 (Aug. 2017), pp. 1523–1544. ISSN: 1521-074X. DOI: 10.1080/01495739.2017.1360165.

[113] G. Li, M. Cinefra, and E. Carrera. "Coupled thermo-mechanical finite element models with node-dependent kinematics for multi-layered shell structures". In: *International Journal of Mechanical Sciences* 171 (Apr. 2020), p. 105379. ISSN: 0020-7403. DOI: 10.1016/j.ijmecsci.2019.105379.

[114] E. Carrera and M. Filippi. "Variable Kinematic One-Dimensional Finite Elements for the Analysis of Rotors Made of Composite Materials". In: *Journal of Engineering for Gas Turbines and Power* 136.9 (Apr. 2014). ISSN: 1528-8919. DOI: 10.1115/1.4027192.

[115] E. Carrera and C. Fagiano. "Mixed piezoelectric plate elements with continuous transverse electric displacements". In: *Journal of Mechanics of Materials and Structures* 2.3 (May 2007), pp. 421–438. ISSN: 1559-3959. DOI: 10.2140/jomms.2007.2.421.

[116] M. D. Demirbas, U. Caliskan, X. Xu, and M. Filippi. "Evaluation of the bending response of compact and thin-walled FG beams with CUF". In: *Mechanics of Advanced Materials and Structures* 28.17 (Jan. 2020), pp. 1755–1764. ISSN: 1537-6532. DOI: 10.1080/15376494.2019.1704951.

[117] A. Pagani and E. Carrera. "Large-deflection and post-buckling analyses of laminated composite beams by Carrera Unified Formulation". In: *Composite Structures* 170 (June 2017), pp. 40–52. ISSN: 0263-8223. DOI: 10.1016/j.compstruct.2017.03.008.

[118] A. Pagani and E. Carrera. "Unified formulation of geometrically nonlinear refined beam theories". In: *Mechanics of Advanced Materials and Structures* 25.1 (Sept. 2016), pp. 15–31. ISSN: 1537-6532. DOI: 10.1080/15376494.2016.1232458.

[119] P. Chiaia, A. Pagani, M. Cinefra, and E. Carrera. "Analysis of transversely isotropic compressible and nearly-incompressible soft material structures by high order unified finite elements". In: *Mechanics of Advanced Materials and Structures* 31.27 (Nov. 2023), pp. 9451–9467. ISSN: 1537-6532. DOI: 10.1080/15376494.2023.2273962.

[120] R. Augello, E. Carrera, M. Filippi, A. Pagani, and E. Tortorelli. "Unified plate finite elements for the large strain analysis of hyperelastic material structures". In: *International Journal of Non-Linear Mechanics* 155 (Oct. 2023), p. 104465. ISSN: 0020-7462. DOI: 10.1016/j.ijnonlinmec.2023.104465.

[121] E. Carrera, I. Kaleel, and M. Petrolo. "Elastoplastic analysis of compact and thin-walled structures using classical and refined beam finite element models". In: *Mechanics of Advanced Materials and Structures* 26.3 (Oct. 2017), pp. 274–286. ISSN: 1537-6532. DOI: 10.1080/15376494.2017.1378780.

[122] M. Petrolo, M. H. Nagaraj, I. Kaleel, and E. Carrera. "A global-local approach for the elastoplastic analysis of compact and thin-walled structures via refined models". In: *Computers & Structures* 206 (Aug. 2018), pp. 54–65. ISSN: 0045-7949. DOI: 10.1016/j.compstruc.2018.06.004.

[123] I. Kaleel, M. Petrolo, A. M. Waas, and E. Carrera. "Computationally efficient, high-fidelity micromechanics framework using refined 1D models". In: *Composite Structures* 181 (Dec. 2017), pp. 358–367. ISSN: 0263-8223. DOI: 10.1016/j.compstruct.2017.08.040.

[124] I. Kaleel, M. Petrolo, A. M. Waas, and E. Carrera. "Micromechanical Progressive Failure Analysis of Fiber-Reinforced Composite Using Refined Beam Models". In: *Journal of Applied Mechanics* 85.2 (Dec. 2017). ISSN: 1528-9036. DOI: 10.1115/1.4038610.

[125] I. Kaleel, M. Petrolo, E. Carrera, and A. M. Waas. "Computationally Efficient Concurrent Multiscale Framework for the Nonlinear Analysis of Composite Structures". In: *AIAA Journal* 57.9 (Sept. 2019), pp. 4029–4041. ISSN: 1533-385X. DOI: 10.2514/1.j057881.

[126] M. Filippi, M. Petrolo, and E. Carrera. "Refined structural theories for the random response of fiber-reinforced and sandwich composite structures". In: *AIAA SCITECH 2022 Forum*. American Institute of Aeronautics and Astronautics, Jan. 2022. DOI: 10.2514/6.2022-0530.

[127] J. N. Reddy. *Mechanics of laminated composite plates and shells: theory and analysis*. CRC press, 2003.

[128] E. Carrera, A. Pagani, and M. Petrolo. "Classical, Refined, and Component-Wise Analysis of Reinforced-Shell Wing Structures". In: *AIAA Journal* 51.5 (May 2013), pp. 1255–1268. ISSN: 1533-385X. DOI: 10.2514/1.j052331.

[129] K. J. Bathe. *Finite element procedures*. Klaus-Jurgen Bathe, 2006.

[130] R. De Borst, M. A. Crisfield, J. J. C. Remmers, and C. V. Verhoosel. *Nonlinear finite element analysis of solids and structures*. John Wiley & Sons, 2012.

[131] I. Lapczyk and J. A. Hurtado. "Progressive damage modeling in fiber-reinforced materials". In: *Composites Part A: Applied Science and Manufacturing* 38.11 (Nov. 2007), pp. 2333–2341. ISSN: 1359-835X. DOI: 10.1016/j.compositesa.2007.01.017.

[132] M. V. Donadon, L. Iannucci, B. G. Falzon, J. M. Hodgkinson, and S. F. M. de Almeida. "A progressive failure model for composite laminates subjected to low velocity impact damage". In: *Computers & Structures* 86.11–12 (June 2008), pp. 1232–1252. ISSN: 0045-7949. DOI: 10.1016/j.compstruc.2007.11.004.

[133] M. Rezasefat, D. Badel Torres, A. Gonzalez-Jimenez, M. Giglio, and A. Manes. "A fast fracture plane orientation search algorithm for Puck's 3D IFF criterion for UD composites". In: *Materials Today Communications* 28 (Sept. 2021), p. 102700. ISSN: 2352-4928. DOI: 10.1016/j.mtcomm.2021.102700.

[134] N. Zobeiry. "Extracting the strain-softening response of composites using full-field displacement measurement". en. In: (2010). DOI: 10.14288/1.0062622.

[135] J. Reiner, N. Zobeiry, and R. Vaziri. "A stacked sublaminate-based damage-plasticity model for simulating progressive damage in composite laminates under impact loading". In: *Thin-Walled Structures* 156 (Nov. 2020), p. 107009. ISSN: 0263-8231. DOI: 10.1016/j.tws.2020.107009.

[136] M. Petrolo, E. Tortorelli, S. Saputo, and E. Carrera. "Tensile damage analysis of composite structures based on 3D Hashin failure criteria and 2D higher-order structural theories". In: *Composites Communications* 56 (June 2025), p. 102395. ISSN: 2452-2139. DOI: 10.1016/j.coco.2025.102395.

[137] M. Petrolo, E. Tortorelli, and S. Saputo. "Compressive damage of composite structures using 3D failure criteria and 2D higher-order structural theories". In: *Mechanics of Advanced Materials and Structures* (Apr. 2025), pp. 1–11. ISSN: 1537-6532. DOI: 10.1080/15376494.2025.2489138.

[138] X. Xu, M. R. Wisnom, X. Li, and S. R. Hallett. "A numerical investigation into size effects in centre-notched quasi-isotropic carbon/epoxy laminates". In: *Composites Science and Technology* 111 (May 2015), pp. 32–39. ISSN: 0266-3538. DOI: 10.1016/j.compscitech.2015.03.001.

[139] I. Kaleel, E. Carrera, and M. Petrolo. "Progressive delamination of laminated composites via 1D models". In: *Composite Structures* 235 (Mar. 2020), p. 111799. ISSN: 0263-8223. DOI: 10.1016/j.compstruct.2019.111799.

[140] N. Zobeiry, R. Vaziri, and A. Poursartip. "Characterization of strain-softening behavior and failure mechanisms of composites under tension and compression". In: *Composites Part A: Applied Science and Manufacturing* 68 (Jan. 2015), pp. 29–41. ISSN: 1359-835X. DOI: 10.1016/j.compositesa.2014.09.009.

[141] J. Reiner, T. Feser, M. Waimer, A. Poursartip, H. Voggenreiter, and R. Vaziri. "Axial crush simulation of composites using continuum damage mechanics: FE software and material model independent considerations". In: *Composites Part B: Engineering* 225 (Nov. 2021), p. 109284. ISSN: 1359-8368. DOI: 10.1016/j.compositesb.2021.109284.

[142] P. Ladeveze and E. Ledantec. "Damage modelling of the elementary ply for laminated composites". In: *Composites Science and Technology* 43.3 (1992), pp. 257–267. ISSN: 0266-3538. DOI: 10.1016/0266-3538(92)90097-m.

[143] J. Lee and C. Soutis. "Measuring the notched compressive strength of composite laminates: Specimen size effects". In: *Composites Science and Technology* 68.12 (Sept. 2008), pp. 2359–2366. ISSN: 0266-3538. DOI: 10.1016/j.compscitech.2007.09.003.

[144] M.H. Nagaraj, E. Carrera, and M. Petrolo. "Progressive damage analysis of composite laminates subjected to low-velocity impact using 2D layer-wise structural models". In: *International Journal of Non-Linear Mechanics* 127 (Dec. 2020), p. 103591. ISSN: 0020-7462. DOI: 10.1016/j.ijnonlinmec.2020.103591.

[145] F. M. Hoblit. *Gust loads on aircraft: concepts and applications*. AIAA, 1988.

[146] S. S. Dey. "Finite element method for random response of structures due to stochastic excitation". In: *Computer Methods in Applied Mechanics and Engineering* 20.2 (Nov. 1979), pp. 173–194. ISSN: 0045-7825. DOI: 10.1016/0045-7825(79)90016-1.

[147] H. Karadeniz, M. P. Saka, and V. Togan. "Introduction to Random Vibration and Stochastic Analysis". In: *Stochastic Analysis of Offshore Steel Structures*. Springer London, Aug. 2012, pp. 121–176. ISBN: 9781849961905. DOI: 10.1007/978-1-84996-190-5_2.

[148] D. E. T. Marques, D. Vandepitte, and V. Tita. "Damage detection and fatigue life estimation under random loads: A new structural health monitoring methodology in the frequency domain". In: *Fatigue & Fracture of Engineering Materials & Structures* 44.6 (Feb. 2021), pp. 1622–1636. ISSN: 1460-2695. DOI: 10.1111/ffe.13439.

[149] H. Tada, P. C. Paris, and G. R. Irwin. "The stress analysis of cracks". In: *Handbook, Del Research Corporation* (1973).

[150] T. L. Anderson. *Fracture mechanics: fundamentals and applications*. CRC press, 2005.

[151] Y. Murakami. "Stress intensity factors handbook". In: *Soc. Mater. Sci., Japan* (1986).

[152] I. S. Raju and J. C. Newman. "Stress-intensity factors for a wide range of semi-elliptical surface cracks in finite-thickness plates". In: *Engineering Fracture Mechanics* 11.4 (Jan. 1979), pp. 817–829. ISSN: 0013-7944. DOI: 10.1016/0013-7944(79)90139-5.

[153] X. J. Zheng, A. Kiciak, and G. Glinka. "Weight functions and stress intensity factors for internal surface semi-elliptical crack in thick-walled cylinder". In: *Engineering Fracture Mechanics* 58.3 (Oct. 1997), pp. 207–221. ISSN: 0013-7944. DOI: 10.1016/s0013-7944(97)00083-0.

[154] S. W. Doebling, C. R. Farrar, and M. B. Prime. "A summary review of vibration-based damage identification methods". In: *Shock and vibration digest* 30 (1998), pp. 91–105.

[155] C. R. Farrar and K. Worden. "An introduction to structural health monitoring". In: *Philosophical Transactions of the Royal Society A: Mathematical, Physical and Engineering Sciences* 365.1851 (Dec. 2006), pp. 303–315. ISSN: 1471-2962. DOI: 10.1098/rsta.2006.1928.

[156] E. Monaco, F. Franco, and L. Lecce. "Experimental and Numerical Activities on Damage Detection Using Magnetostrictive Actuators and Statistical Analysis". In: *Journal of Intelligent Material Systems and Structures* 11.7 (July 2000), pp. 567–578. ISSN: 1530-8138. DOI: 10.1106/2urv-d0hy-0qla-hawh.

[157] T. Mickens, M. Schulz, M. Sundaresan, A. Ghoshal, A. S. Naser, and R. Reichmeider. "Structural Health Monitoring of an aircraft joint". In: *Mechanical Systems and Signal Processing* 17.2 (Mar. 2003), pp. 285–303. ISSN: 0888-3270. DOI: 10.1006/mssp.2001.1425.

[158] D. Y. Gao, W. X. Yao, W. D. Wen, and J. Huang. "Equivalent Spectral Method to Estimate the Fatigue Life of Composite Laminates Under Random Vibration Loadings". In: *Mechanics of Composite Materials* 57.1 (Mar. 2021), pp. 101–114. ISSN: 1573-8922. DOI: 10.1007/s11029-021-09937-2.

[159] E. Tortorelli, M. Valente, G. Palaia, and E. Carrera. "Preliminary Fatigue Life Prediction of Composite Wing under Gust Spectrum LoadsUsing a CUF-Based Approach". In: *AIDAA/CEAS*. AIDAA/CEAS. 2025.

[160] G. Sedky, A. Gementzopoulos, I. Andreu-Angulo, F. D. Lagor, and A. R. Jones. "Physics of gust response mitigation in open-loop pitching manoeuvres". In: *Journal of Fluid Mechanics* 944 (July 2022). ISSN: 1469-7645. DOI: 10.1017/jfm.2022.509.

[161] D. Marques, D. Vandepitte, and V. Tita. "Sensitivity and uncertainty analysis for structural health monitoring with crack propagation under random loads: A numerical framework in the frequency domain". In: *Fatigue & Fracture of Engineering Materials & Structures* 46.1 (Oct. 2022), pp. 137–152. ISSN: 1460-2695. DOI: 10.1111/ffe.13853.

[162] N. W. M. Bishop and F. Sherratt. "Fatigue life prediction from power spectral density data". In: *Environmental Engineering* (1989).

[163] European Union Aviation Safety Agency (EASA). *Type Certificate Data Sheet No. EASA.A.089 - Pilatus PC-12*. Tech. rep. EASA, 2023.

Appendix A

List of publications

A.1 Journal articles

- R. Augello, E. Carrera, M. Filippi, A. Pagani and **E. Tortorelli**. Unified plate finite elements for the large strain analysis of hyperelastic material structures, *International Journal of Non-Linear Mechanics*, 155, 2023.

- M. Petrolo, **E. Tortorelli**, S. Saputo and E. Carrera. Tensile damage analysis of composite structures based on 3D Hashin failure criteria and 2D higher-order structural theories, *Composites Communications*, 56, 2025.

- M. Petrolo, **E. Tortorelli** and S. Saputo. Compressive damage of composite structures using 3D failure criteria and 2D higher-order structural theories, *Composites Communications*, 2025.

A.2 Conference proceedings

- **E. Tortorelli**, M. Filippi,A. Pagani, M. Petrolo, and E. Carrera. Refined structural theories for dynamic analysis of composite structures subjected to random excitation, *ICFC9-The 9th International Conference on the Fatigue of Composite*, Vicenza, Italy, 21-23 June 2023.

- M. Filippi, **E. Tortorelli**, M. Petrolo, and E. Carrera. Refined structural theories for dynamic and fatigue analyses of structure subjected to random excitations, *XXVII AIDAA Congress*, Padova, Italy, 4-7 September 2023.

- **E. Tortorelli**, S. Saputo and E. Carrera. 2D higher-order theories for progressive damage model of composite structures based on Hashin and Puck failure criteria, *AIDAA 4th Aerospace PhD-Days*, Scopello, Italy, 6-9 May 2024.

- **E. Tortorelli**, M. Valente, G. Palaia and E. Carrera. CUF-based fatigue prediction of composite structures under climate-modified gust spectra, *ICFC10-The 10th International Conference on the Fatigue of Composite*, Sapporo, Japan, 1-4 July 2025.

- **E. Tortorelli**, G. Palaia and E. Carrera. CUF-based fatigue life estimation of metal and composite structures: a preliminary assessment in the frequency domain, *MECHCOMP10-The 10th International Conference on Mechanics of Composite*, Porto, Portugal, 23-25 July 2025.

- **E. Tortorelli**, G. Palaia and E. Carrera. Fatigue life estimation in frequency-domain of composite and metallic structures via CUF and Dirlik's method, *The 10th CEAS Aerospace Europe Conference, The 28th AIDAA International Congress*, Torino, Italy, 1-4 December 2025.

- **E. Tortorelli**, M. Valente, G. Palaia and E. Carrera. Preliminary fatigue life prediction of composite wing under gust spectrum loads using a CUF-based approach, *The 10th CEAS Aerospace Europe Conference, The 28th AIDAA International Congress*, Torino, Italy, 1-4 December 2025

- M. Petrolo, M. Filippi, E. Carrera, C. Franceschini and **E. Tortorelli**. Low-Velocity impact Analysis of composites plates using the Hashin 3D Criterion and Layer-Wise Models, *The 10th CEAS Aerospace Europe Conference, The 28th AIDAA International Congress*, Torino, Italy, 1-4 December 2025

This Ph.D. thesis has been typeset by means of the TEX-system facilities. The typesetting engine was pdfLATEX. The document class was `toptesi`, by Claudio Beccari, with option `tipotesi=scudo`. This class is available in every up-to-date and complete TEX-system installation.